POLITECNICO
MILANO 1863

School of Industrial and Information Engineering

Master of Science in Engineering Physics

Photonics and Nano Optics

Master Thesis

Femtosecond Laser Writing in Material Platforms for Quantum Technologies

Advisor:

Prof. Roberta Ramponi

Co-Advisor:

Dr. Shane Eaton

Author:

Ciavolino Vincenzo
942833

Academic Year 2022-2023

Acknowledgments

I would like to express my great appreciation to Professor Roberta Ramponi and Doctor Shane Eaton for the opportunity they gave me to work on such an interesting topic, and to all the people of the Felice Laboratory, especially Giulio who constantly helped me during my work, Argiro and Vibhav, whose work was fundamental for the development of the laboratory and my studies on the project.

I would also like to thank all the people that have contributed to my academic studies in Politecnico di Milano, all the professors that have challenged my learning, all the colleagues met in the last years. A special mention to Alina, who made possible for me to take this amazing path. A kind regard goes to my family, friends and loved ones, for their fundamental and consistent support that made my journey a wonderful journey.

Vincenzo

Contents

List Of Images

Abstract

Color centers in wide bandgap semiconductors have a disruptive potential for quantum technology, as they act as single photon sources, and can be used as spin qubits. Recently, femtosecond laser writing of integrated photonic circuits emerged as a valuable technique due to its capability of 3D patterning with low residual lattice damage.

In this thesis work, in-depth details of the aforementioned writing method, a study of the optimal parameters, and its application towards the creation of photonic components, such as waveguides and Y-Splitters, is presented. Moreover, the possibility to create vacancy-related defects within the bulk of relevant platforms such as diamond, silicon carbide and hexagonal boron nitride, is explored and findings are reported.

This study emphasizes the convenience and adaptability of femtosecond laser fabrication of integrated quantum photonic devices in relevant platforms for quantum applications and looks forward to the development of this technique as a possible game changer for fully exploiting and uncovering the powerful nature of the 21-th century “particle zoo” represented by color centers.

Chapter 1

Introduction

Current years have been crucial for the development of the field of quantum technology and each individual area of application such as quantum computers, simulators, communications [1], sensors and metrology is still in its early years and hence is characterized by a large room for improvement.

For instance, major research is being performed to develop applications in the fields of quantum computing and communication, where the conventional classical bits encoding information in classical computers are being replaced by quantum bits (q-bits), which should result in devices with the computational power to solve complex problems. Among others, quantum computers will be applicable to highly multivariable macro-scale problems such as predicting stock market trends or forecasting the global climate [2]. Other studies are performed on topics like quantum simulations and quantum walks to understand the behavior of nanoscale complex systems in a quantum mechanical view [3], on quantum metrology to explain physical systems using quantum mechanical parameters like quantum entanglement and squeezed states [4] and more radical ideas like quantum teleportation [5].

The key component for the development of any quantum device is given by a system in which a quantum mechanical parameter can be initialized, manipulated and read out. The most conventional way to pursue this goal has been the use of trapped ions [6] or cold atoms [7], techniques requiring temperatures close to 0 K to be functional and ultra-high vacuum environments, making them unsuitable for daily use in scalable technological products. Recently, color center defects in wide bandgap semiconductors have emerged as a suitable candidate for quantum computing and room temperature quantum sensing [8], with the ability of optical excitation, manipulation and readout.

Moreover, their spin coherence times have been found to be similar to those of trapped ions [9]. Intense research is being undertaken to utilize these particular properties for quantum information and magnetometry [10, 11, 12, 13]. However, a photonic device capable of improving the optical emission and collection from the emitters within the bulk of the crystal is still lacking. In addition, deterministic placement of defects in the bulk is crucial for integrated quantum photonics.

To tackle the first limitation and improve the coupling efficiency, waveguides and optical cavities have been fabricated using focussed ion beam and reactive ion etching resulting in the creation of micro-cylinders [14], nano-wires [15, 16], nano-pillars [17], nano-beams [18] and nano-waveguides [19], whose performance is very sensitive to surface roughness leading to non-ideal shapes.

In this thesis, femtosecond laser micromachining is applied to solve the challenges impeding the full application of the properties of color centers in wide bandgap semiconductors devices. From the first results showing the ability to laser write optical waveguides in glass in 1996 [20], femtosecond laser writing has been extensively used to fabricate integrated 3D photonic networks in transparent dielectrics and crystals [21-23]. One of the main objectives of this thesis has been the use of femtosecond laser writing to fabricate 3D photonic networks in diamond and deterministically place spin defects for quantum information and magnetometry.

Laser writing of waveguides in diamond is a very challenging task due to the high refractive index of diamond leading to spherical aberration. Moreover, previous studies of diamond laser writing have shown the creation of graphitic lines [24, 25], which are detrimental for optical guiding since graphite is a strong absorber in the visible spectrum. The optimal parameters for laser writing of photonics structures in diamond were systematically investigated in this thesis, in particular to achieve stress induced single mode waveguiding while avoiding significant graphitization, either in optical grade diamond and in NV doped diamond. The success of laser writing of a simple waveguide can be extended to create engineered 3D components such as Y-Splitters.

Regarding the creation of color centers, their spatial positioning within the lattice of crystals is of paramount importance for practical device fabrication. The conventional ion implantation technique for the color centers' creation is detrimental to the spectral properties of the emitters due to the lattice damage and stress created in its vicinity [26, 27]. The technique is also only successful for placements close to the surface, where the centers' spectral coherence times are reduced due to dangling bonds and surface interactions. As an alternative, focused femtosecond laser pulses have been shown to create vacancies in the bulk of glass [28, 29] and crystals [30]. From this starting point, the idea of laser written color centers has been progressively extended to promising wide bandgap semiconductors for the creation of optically active defects within the bulk of a crystal. With the ability of laser writing a waveguide and deterministically placing color centers, an integrated device consisting of laser written spin defects coupled to laser written waveguides can be developed.

This thesis explores the wide range of capabilities of femtosecond laser writing in wide bandgap semiconductors. A chapter-wise summary is provided below.

In chapter 2, a background about femtosecond laser micromachining is introduced, emphasizing the physics behind the femtosecond laser-matter interaction during laser fabrication. In the subsequent section, an overview of the science behind the use of color centers for quantum technologies is presented.

In chapter 3, the experimental details of the two main femtosecond laser micromachining stations are treated, along with the various materials and optical characterization techniques used in this thesis and necessary to understand the performances of the laser written photonic networks.

In chapter 4 the systematic study of the optimal parameters to laser write optical

waveguides within the bulk of diamond is presented and their optical characterization is explained. The photoluminescence and ODMR measurements performed on the fabricated waveguides are reported. A subsection contains the fabrication and characterization of the vertical Y-Splitters in the bulk of diamond. Lastly, the fabrication and characterization of waveguides in DNV diamond resulting in a straightforward proof-of-concept quantum sensor is presented.

In chapter 5, laser writing of static exposures in diamond, SiC and hBN is explored. The methodical procedure of fabrication and characterization to obtain the optimal pulse energy and pulse number to create high quality NV centers within the bulk of diamond is explained. Subsequently, the attempts to create vacancy defects in SiC are reported and finally, hBN is studied as a suitable platform for quantum technologies and the relative results of the fabrications are presented.

Chapter 2

Background

This chapter will deal with the theoretical framework that constitutes the building blocks necessary to the pursuit of the goal of the thesis, namely the fabrication through femtosecond laser micromachining of integrated quantum photonic devices.

In particular, the first paragraph tackles the details about the fabrication method, addressing the physical mechanisms involved during the irradiation of transparent materials with femtosecond laser pulses. Furthermore, it is explained how the laser interaction with the crystal leads to modifications of the crystalline structure which can be exploited to create optical waveguides. The advantages of the laser fabrication technique with respect to alternative methods are also presented.

The second paragraph contains an in-depth analysis of the relevant properties of defects centers for quantum technology. It is divided into four subsections, each of which describes one of the fundamental properties defining the behavior of color centers, specifically spin, optical, charge and host material properties.

2.1 Femtosecond Laser Micromachining

Since its initial demonstration by Hirao's group in 1996 [31], femtosecond laser micromachining has become a very powerful technique for writing photonic networks in transparent dielectrics and crystals. The processing mechanism is based on nonlinear absorption and avalanche ionization [1, 2, 26] within the focal volume of tightly focused ultrashort laser pulses inside transparent dielectrics and crystals, leading to highly localized modifications within the bulk.

2.1.1 Nonlinear Photoionization Process

When femtosecond laser pulses at visible and near-infrared wavelengths are focused within a transparent dielectric, linear absorption cannot occur because the photons' energy ($h\nu$) is usually lower than the material's band gap energy (E_g), $h\nu < E_g$. Higher-order nonlinear absorption, on the other hand, has the potential to happen mainly through multiphoton absorption, tunneling ionization, or a combination of the two. As shown in Figure 2.1(a), multiphoton absorption can happen when a number m of photons satisfies the condition $mh\nu > E_g$, bridging the material's band gap energy and resulting in the absorption of the photons from an electron in the valence band, which gets promoted to the conduction band. Multiphoton absorption typically predominates at high frequencies and low laser intensities, while for high intensities and low frequencies the electric field deforms the band structure, lowering the potential barrier between the valence and conduction bands and enabling direct band-to-band tunneling of the electron from the valence to conduction band, as shown in Figure 2.1(b).

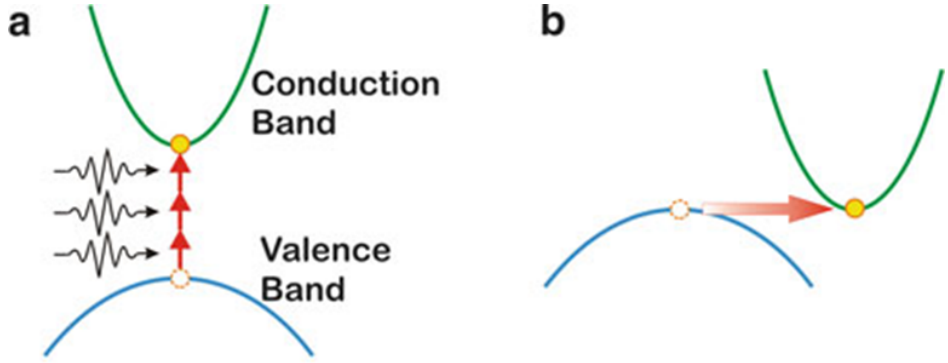

Figure 2.1. Schematic showing the various nonlinear photoionization processes occurring during femtosecond laser micromachining: (a) Multiphoton absorption, (b) Tunneling ionization.

Which of two competing processes will prevail is determined by the Keldysh parameter

[5]:

$$\gamma = \frac{\omega}{e}\sqrt{\frac{m_e c n \epsilon_0 E_g}{I}}$$

where, ω is the laser frequency, I is the intensity of the laser beam at the focus, m_e is the effective mass of the electron and n is the refractive index of the material. If γ is much lower than 1.5, tunneling ionization dominates. If it is much greater than 1.5, multiphoton absorption dominates and if the value is close to 1.5, nonlinear absorption occurs due to a combination of both processes.

Alternatively, avalanche ionization can also happen as a result of multiple photons being absorbed in succession by the electrons in the conduction band. When the energy of the electron in the conduction band rises above the band gap energy, an impact ionization can lead to an electron in the valence band being excited to the conduction band resulting in two excited electrons. Additional free carrier absorption involving the two electrons could result in more impact ionization of other electrons. As long as the electric field is present, this process can lead to an exponential increase in the number of electrons in the conduction band. The initial presence of electrons in the conduction band is necessary for avalanche ionization, and this can be accomplished through multiphoton, tunneling absorption, or thermally excited impurities of defect states.

2.1.2 Relaxation and Modification

After the femtosecond laser pulse has been nonlinearly absorbed by the transparent material, a relaxation process occurs, transferring the energy to the lattice at the focal volume, altering the material.

Although the actual physics behind the relaxation process is not fully understood for the materials discussed in this work, it is helpful to study the simplest scenario of femtosecond laser interaction with fused silica, which leads to three distinctive material modifications depending on the laser energy: smooth refractive index change,

birefringent gratings and void creation, as schematically shown in Figure 2.2 [4].

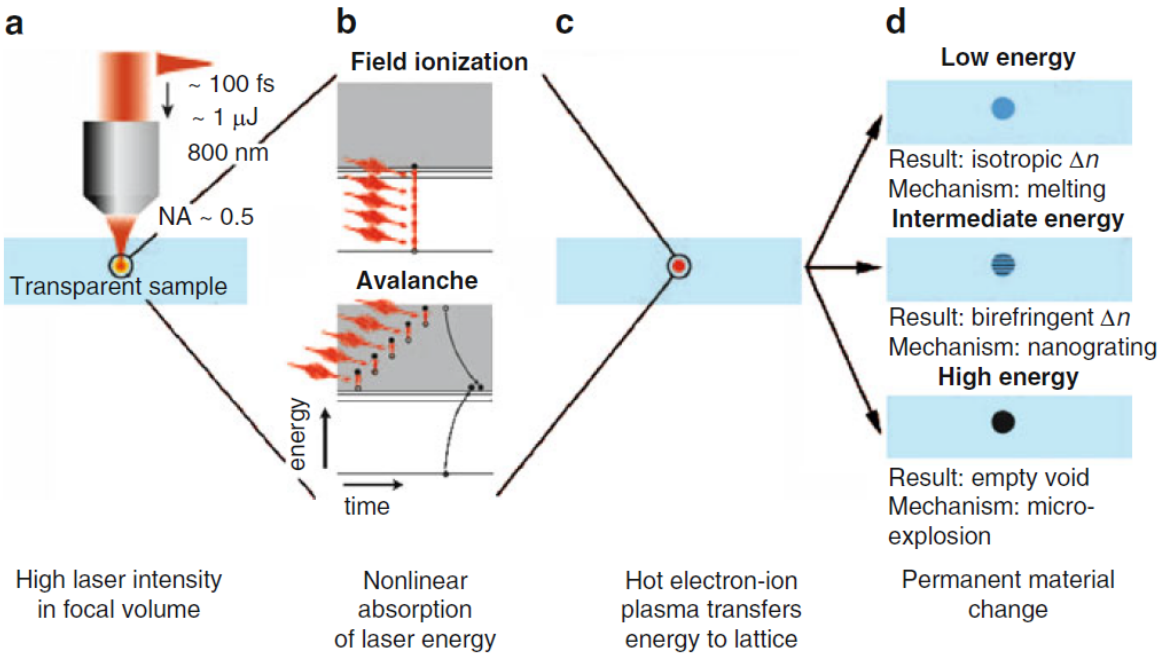

Figure 2.2. Schematic showing relaxation process after femtosecond laser pulse interaction with the material. (a) Femtosecond laser pulses focused within the bulk of transparent material. (b) Nonlinear absorption of energy by multiphoton/tunneling or avalanche ionization in the material. (c) Energy transferred to the lattice. (d) Three distinctive material modifications after relaxation depending on the laser energy: isotropic refractive index change, birefringent nanogratings creation and empty void creation.

The following section discusses the interaction of femtosecond laser pulses with crystals. The isotropic refractive index change at low energies (~ 100 nJ pulse energy using an objective of 0.6 NA at a wavelength of 800 nm with 100 fs pulse duration) is caused by a number of mechanisms, including the formation of color centers [5], thermal heating followed by cooling that causes resolidification [2, 6, 7], modification of chemical bonds in the material matrix that results in an increase in density [8], or a combination of the above. Ion migration is a key factor in the refractive index distribution that results in multicomponent glasses [9, 10, 11]. The resulting change in refractive index enables optical mode confinement, which can be exploited to create advanced optical photonic circuits with three-dimensional layouts by translating the sample, and consequently the laser focal point, within the glass substrate [4, 12, 13].

A birefringent refractive index change has been observed for moderate pulse energies

(~ 150 – 500 nJ laser pulse energy using an objective of 0.6 NA at a wavelength of 800 nm with 100 fs pulse duration), which has been attributed to the formation of nanogratings, caused by the interference of the laser field and the induced electron plasma wave [14, 15]. The creation of buried microfluidic channels has greatly benefited from such laser-written gratings in the bulk of glasses. By polarizing the laser beam perpendicularly to the writing direction, which produces parallel nanogratings, the tracks produced serve as channels for preferential etching with acids like HF, resulting in the creation of buried channels. The channels have been the primary base for lab-on-chip applications involving microfluidic applications [16, 17, 18].

The laser pulses induce a shock wave in the material creating a void for high energies (> 500 nJ using an objective of 0.6 NA at a wavelength of 800 nm with 100 fs pulse duration). Despite having a higher refractive index, the area around the void is unsuitable for optical waveguiding, while applications for memory storage have made use of these voids [5].

2.1.3 Laser Writing of Waveguides in Crystals

Based on the laser energy, femtosecond laser inscription of optical waveguides in crystals can be divided into two main morphological modifications, which are covered below.

The irradiation with a single line of low laser energy, which is also known as type I modality of femtosecond laser writing, can gently modify some crystals, as shown in Figure 2.3(a). Weak lattice disorders and small changes in the molar volume cause the process to produce a higher refractive index in the area surrounding the focal volume [19, 20]. Only ZnSe [21], Li:NbO_3 [22], Nd:YCOB [23] and periodically-poled lithium niobate [19] have shown this mild increase in refractive index.

Despite the fact that the type I modality of writing is preferred to create arbitrary-shaped 3D photonic networks in crystals, weak refractive index increases usually fail to produce low loss waveguides, which have also been found to be

thermally unstable [24].

More commonly laser irradiation in crystals causes a decrease in refractive index at the focal volume due to the formation of lattice disorder or amorphization, which causes a lower density at the focal spot. However, optical waveguiding may take place on the sides of the modified region, where the stress fields cause a refractive index increase, despite the negative refractive index change at the focal spot [25, 27]. This can lead to the creation of low loss optical waveguides by laser writing two closely spaced modification lines, which results in a stressed central region between them, as shown in Figure 2.3(b). The type II modality of femtosecond laser writing is the name given to this geometry of laser writing. Moreover, the modifications that result are thermally stable [24], which is important when annealing processes of the devices are required, as it will be shown in the next chapters.

Similar photonic structures have been realized in a variety of crystals, including lithium niobate [22], silicon [28], KGW [29], YAG [30], ZnSe [21], and KTP [32], by carefully adjusting the geometry of the modification.

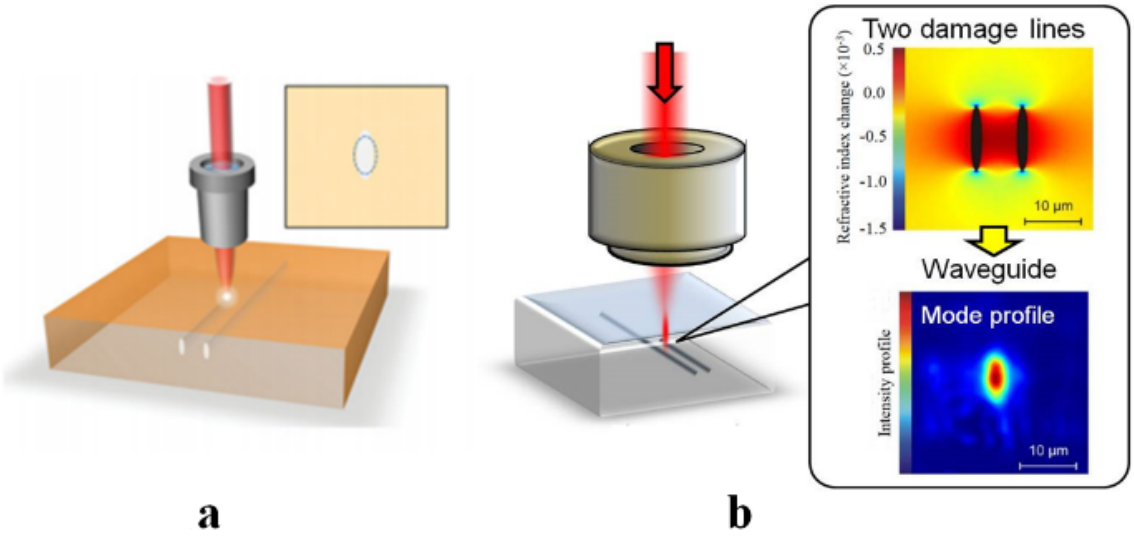

Figure 2.3. Schematic showing the two modalities of femtosecond laser writing of waveguides. (a) The type I modality, where a single line of increased refractive index modification acting as the core for the optical waveguiding is created. This is generally employed for laser writing in glasses. (b) The type II modality, where two lines of decreased refractive index are laser written close to each other creating a stressed central in the region between them and hence confining the optical mode between the two lines. This is generally employed for laser writing of optical waveguides in crystals.

2.1.4 Fundamental Physical Quantities of Femtosecond Lasers

In femtosecond laser micromachining, the interaction of the femtosecond laser pulses with the material, resulting in nonlinear absorption at the focus is the main physical process taking place. However, as already shown in the previous chapters, nonlinear absorption strongly depends on the laser intensities at the focal volume and to overcome the breakdown threshold, the femtosecond laser pulses need to be focused using high numerical aperture microscope objectives, reaching up to 10^{13} W/cm^2 peak intensities at the focus. The use of the focusing objective also results in micrometer spot sizes at the focal volume, corresponding in principle to micrometer-size spatial resolution for the modifications. However, the ultimate resolution of the laser processing is greatly influenced by the spot size at the focal volume and the material properties. Assuming the laser beam to be Gaussian, when a femtosecond laser beam of wavelength λ is focused into a material of refractive index n, using a focusing objective of numerical aperture NA, the diffraction limited minimum beam waist radius ω_0 , which is half the spot size diameter, is given by the following equation:

$$\omega_0 = \frac{M^2 \lambda}{\pi NA}$$

where, M^2 is the Gaussian beam propagation factor, assumed to be 1 for a pure Gaussian beam. The Rayleigh range of the focus z_0 within the material, defined as the distance along the propagation direction of a beam from the waist to the place where the area of the cross section is doubled, is given by the following equation:

$$z_0 = \frac{M^2 n \lambda}{\pi NA}$$

ω_0 and z_0 dictate the focal spot size and hence the peak intensities at the focal point.

A visual depiction of a focused Gaussian beam with the relevant parameters is displayed in figure 2.4.

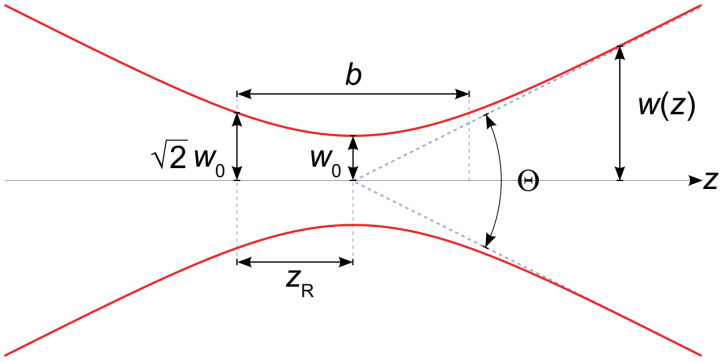

Figure 2.4. Gaussian beam width w(z) as a function of the axial distance z. w0: beam waist; b: confocal parameter; zR: Rayleigh range; Θ: total angular spread.

The peak intensity I_p at the focus is given by:

$$I_p = \frac{P_{peak}}{\pi \omega_0^2}$$

where,

$$P_{peak} = \frac{E_p}{\tau_p}$$

where, E_p is the energy per pulse and τ_p is the pulse duration.

In addition to the Gaussian beam parameters ω_0 and z_0, the spot size at the focal volume is significantly influenced by optical aberrations, particularly chromatic and spherical aberrations. The chromatic aberration can be easily addressed by using focusing objectives that are chromatic aberration corrected for the desired wavelengths. While the spherical aberration is primarily caused by the mismatch in refractive indices between the material and the air, which results in an elongated focal volume within the bulk of the material. Additionally, spherical aberration is proportional to the cube of the NA of the objective. Collar-corrected dry focusing objectives can be used to correct for spherical aberration, but they are typically made for laser writing in glasses (n = 1.5). Spherical aberration significantly impairs laser writing with high NA objectives in high refractive index materials, such as diamond (n = 2.4), by axially distorting the intensity distribution at the focal volume. Furthermore, writing depth independent symmetric

structures in three dimensions is challenging due to the fact that spherical aberration increases with depth. However, adaptive optics components such as a spatial light modulator (SLM) or a deformable mirror can be used to apply a suitable negative phase distortion to the beam, resulting in a circular spot at the focus, symmetrical when viewed from the transverse direction [33, 34]. Due to the spatially varying refractive index produced in the material's focal volume during laser writing, self-focusing can also happen at high intensities. Since the second order nonlinear refractive index, n_2, is typically positive, the center of the beam experiences a greater refractive index change, which functions as a positive lens to focus the beam inside the material. Self-focusing only depends on the peak power, being a nonlinear phenomenon. The critical power P_c for self-focusing is given by:

$$P_c = \frac{3.88\lambda^2}{8\pi n_0 n_2}$$

where, n_0 is the linear refractive index of the material. In order for the laser writing not to be hampered by self-focusing, the peak powers used for laser writing must be below the critical power P_c.

2.1.5 Advantages of Femtosecond Laser Micromachining over other Fabrication Techniques

As previously stated, conventional fabrication technologies are based on photolithographic processes, which enable strong miniaturization and mass production, but have drawbacks such as high residual lattice damage and low depth of inscription. In quantum optics applications a relevant role has been played also by the direct inscription of the circuits by femtosecond lasers, here's the advantages this technique brings with respect to the others:

- Simple and low-cost setup. There is no need for extensive sample preparation, masks, or clean-room equipment when using femtosecond laser

micromachining.

- Ability of 3D structuring. By translating the sample with respect to the laser focus using computer-controlled motion stages, microstructures may be formed along 3D paths because the material modification occurs only at the focal volume due to nonlinear absorption. As an alternative, one can create 3D structures by keeping the sample still while translating the laser focus with galvo scanners.
- Rapid prototyping. Femtosecond laser fabrication is a direct writing method requiring no mask. Arbitrary 3D optical circuits can be realized by simply changing the algorithm of the computer-controlled translation stages.
- Versatility. Numerous transparent materials, including active and passive glasses, nonlinear glasses, ceramics, crystals, and polymers, have been successfully written on using femtosecond lasers.
- Various modalities of microfabrication. Femtosecond lasers can write in a variety of ways, such as: (1) bulk optical waveguide writing [1]; (2) bulk modification followed by chemical etching to create hollow and buried microchannels [16]; (3) surface laser ablation by scanning the focus along the sample surface to create microfluidic channels, microholes, and diffractive optics [35]; and (4) two-photon polymerization to create 3D microstructures in photoresists [36].

Given the versatility and convenience of the femtosecond laser writing, major scientific initiatives have been undertaken by different research groups around the globe exploiting such a technique. Twenty years since the original paper by Davis et al. [31], there are demonstrations of devices like directional couplers, Y-splitters, polarization controllers, Bragg reflectors, optical microcavities, interferometers, lasers, buried microfluidic channels for novel applications in technologies such as astrophotonics [37, 38], quantum information [39], telecommunications [40, 41], sensing [42], lab on a

chip [43] and lab on a fiber [44].

To meet the demands of current and emerging technologies, industry is also actively pursuing femtosecond laser microfabrication. High-repetition rate/energy femtosecond lasers specifically designed for femtosecond laser microfabrication are now being produced by laser companies like Spectra Physics, Coherent, Light conversion, IMRA America, and Menlo Systems. Additionally, for 3D direct laser writing in photoresists, user-friendly and fully integrated femtosecond laser fabrication systems are offered by Nanoscribe (Eggenstein-Leopoldshafen, Germany). Most importantly, new businesses have started using femtosecond laser writing to create functional products for end users. For instance, OZ Optics (Ottawa, Canada) creates specialized optical power taps, while Optoscribe (Livingston, Scotland) uses lasers to create 3D waveguides and photonic lanterns for optical communications and astrophotonics. In order to measure temperature, strain, pressure, and vibration, FemtoFiberTec (Berlin, Germany) creates fiber Bragg gratings, FEMTOprint (Muzzano, Switzerland) realizes microphotonics in glass and polymers for micromechanics/optomechanics and 5D high density memories. For integrated lab-on-a-fiber devices, Incise Photonics (Toronto, Canada) writes waveguide and microchannel devices directly in fibers.

2.2 Solid-state Spin Defects

Solid-state defects are at the heart of numerous condensed matter physics challenges and opportunities. They are either highly detrimental to crystalline growth, or beneficial due to their ability to modulate and control material properties. Impurities, when isolated, act as analogues of atomic systems in an effective “semiconductor vacuum” [45], with properties defined by the host substrate, allowing them to be studied for semi-classical and later quantum applications.

Electron spin resonance experiments with phosphorus dopants in both natural and isotopically purified silicon were carried out in 1958, with the first spin- echo experiments [46] demonstrating spin coherence times as high as 0.5 ms. In the 1960s, the first solid-state laser was built using chromium dopants in ruby [47] and numerous electron spin resonance experiments were carried out using rare-earth ions in oxides [48]. However, it wasn't until the turn of the century that there was a strong push for the use of spin defects for quantum applications. This began with the proposal of quantum computers based on silicon donors with electrical gates [49] or on rare-earth ions in Y_2SiO_5 with optical cavities [50], as well as the first measurement of single nitrogen-vacancy (NV) defects in diamond [51]. Following these achievements, defects with solid-state spins have been rapidly applied to all three major fields of quantum science: sensing, computing, and communication.

In quantum sensing, the spin state is used to acquire a phase shift from interactions with the environment [52], and an optical interface (that is, spin-to-photon conversion) allows optical readout of a spin qubit, potentially enhanced by spin-to-charge conversion [53]. Quantum computing is most closely realized with large clusters of nuclear spin registers coupled to an electron spin [54], alongside optical or charge-based control for efficient initialization and readout [56]. Finally, quantum communications demand an efficient, spin-dependent optical interface [57] and a spin quantum memory [58].

In addition to the properties of their host material, defects are defined by their spin, optical, and charge states.

2.2.1 Spin Properties

For defects in solid state materials, quantum information is generally encoded in the electron spin of the orbital ground state of the defect. Controllable qubits with long relaxation and coherence times can be obtained by electron spins. They can be coupled to nuclear spins for long-lived quantum memories and advanced applications. Spin initialization, control and readout fidelities are critical parameters to optimize for all quantum applications.

Spin Relaxation

The spin relaxation time, T_1 , is the characteristic time for the spin to reach an equilibrium state after random spin flips along the spin quantization axis.

T_1 fundamentally limits the possible coherence time, T_2 , such that $T_2 \leq 2T_1$, though, in practice, $T_2 \leq 0.5T_1$ or $1T_1$ [59]. The thermal relaxation resulting from the absorption, emission, or scattering of phonons in the crystal via the spin-orbit interaction primarily determines the electron spin T_1 in the solid state. This sets the operating temperature regime of the qubit, which is shown in Fig. 2.5(a) for common materials.

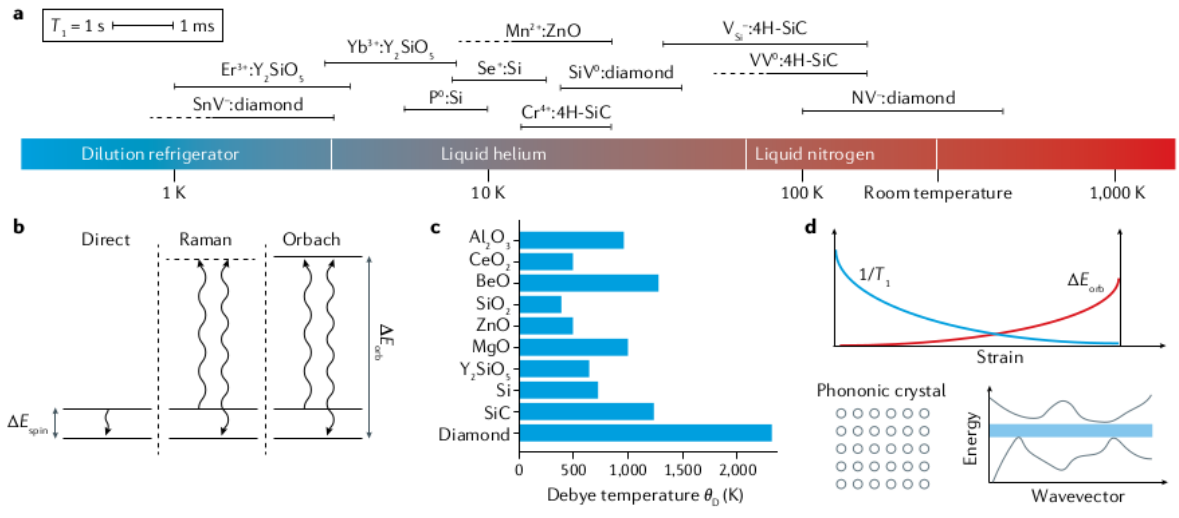

Figure 2.5. (a) Temperature ranges corresponding to spin relaxation times, T_1 , from 1 ms to 1 s in common defects for quantum information. Dotted lines indicate parameters missing from the literature. (b) Phonon processes for spin–lattice relaxation of electron spins in the solid state. ΔE_{spin} is the energy splitting between the ground spin states and ΔE_{orb} the energy splitting between the ground and a nearby excited state. (c) Summary of Debye temperatures in relevant qubit host materials. (d) Engineering T_1 relaxation. Top: strain tuning of the ground-state orbital splitting can reduce the contribution of the Orbach process. Bottom: phononic structures can gap (in blue) relevant energies, such as ΔE_{orb} or ΔE_{spin}.

T_1 models are generally divided into three relaxation mechanisms (Fig. 2.5(b)) : direct absorption or emission of one phonon resonant between two electron spin states, Raman processes by virtual absorption and emission of two phonons and Orbach [60] relaxation by phonon excitation to a higher excited state, followed by decay and emission of a phonon.

For non-integer (Kramers) spins, T_1 follows :

$$\frac{1}{T_1} \approx K_D K_\theta \Delta E_{spin}^4 T + K_\theta^2 (K_{R1} T^5 + K_{R2} \Delta E_{spin}^2 T^7 + K_{R3} T^9) + K_O K_\theta \frac{\Delta E_{orb}^3}{e^{\left(\frac{\Delta E_{orb}}{k_b T}\right)} - 1}$$

whereas for integer (non-Kramers) spins, T_1 follows:

$$\frac{1}{T_1} \approx K_D K_\theta \Delta E_{spin}^2 T + K_\theta^2 (K_{R1} T^5 + K_{R2} T^7) + K_O K_\theta \frac{\Delta E_{orb}^3}{e^{\left(\frac{\Delta E_{orb}}{k_b T}\right)} - 1}$$

where $K_\theta \propto \rho^{2/3}/\theta_D^5$ is a host-dependent parameter with ρ the atomic density and θ_D the Debye temperature, and K_D , $K_{R1\text{-}3}$ and K_O are the coefficients for the direct, Raman and Orbach mechanisms, respectively. ΔE_{spin} is the energy splitting between the ground spin states, ΔE_{orb} is the energy splitting (lower than the Debye frequency) between the ground and a nearby orbital excited state and k_b is the Boltzmann constant. Equations just presented are valid for $\Delta E_{spin} / k_b < T < \theta_D$.

For material design (Fig. 2.5(c)) , the choice of the Debye temperature θ_D (via K_θ) has a large impact on the spin relaxation, especially for Raman processes ($\propto K_\theta^2$). For Raman processes, one power law generally dominates, such as T^9 in rare-earth ions. The Orbach mechanism often dominates in the presence of a low-lying orbital state [61] .

At extremely low temperatures ($\ll$1 K), a phonon bottleneck effect can occur, in which there are not enough phonons to transfer energy from the spin to the lattice and the relaxation time is reduced. The dependence on ΔE_{spin} for some of the mechanisms allows for tunability, usually using an external magnetic field [62] . However, electron spin relaxation is not limited to phonon processes. Resonant magnetic or electric noise from the environment can effectively drive random flips of the defect electron spin; in turn, monitoring T_1 can be used directly as a sensing mechanism [63] .Charge instability, in which the defect transitions between charge states in a non-spin-conserving manner, is another decay mechanism. Lastly, unwanted photoexcitation to an excited state followed by relaxation may cause spin flips similar to phonon-induced processes.

An isolated nuclear spin-1/2 in the solid state has very few direct phonon-mediated T_1 mechanisms. In most cases, coupling with other nuclear spin bath components or with the electron spins in a sample limits the spin relaxation time. For the latter case, the nuclear spin T_1 is limited by cross-relaxation involving simultaneous electron and nuclear spin flips driven by phonon modulation of the hyperfine coupling. In this case, the nuclear spin coherence may have an upper limit $T_{2,nuclear} \leq 2T_{1,electron}$ [58].

One of the most difficult properties to improve for a given temperature, defect, and host material is the phonon-limited T_1. However, the Orbach contribution can be reduced by increasing ΔE_{orb} through strain tuning, and engineering a phononic bandgap around ΔE_{spin} or ΔE_{orb} could eliminate either the direct or Orbach processes (Fig. 2.5(d)). Nanostructures smaller than the wavelength of relevant acoustic phonons could theoretically improve T_1 for spins, though they may suffer from surface proximity effects, and the required scales commonly exceed fabrication capabilities.

Spin Coherence

In a quantum system, decoherence constitutes loss of phase information. Long coherence times, higher control reliabilities, and longer phase acquisition times are needed for quantum applications. Thankfully, decoherence can be well predicted and suppressed with sufficient knowledge of the quantum system and its environment. Typically, spin qubits lose their phase coherence, owing to surrounding fluctuating magnetic sources, that is, other nuclear and electron spins. Coherence is characterized by two key figures: the inhomogeneous dephasing time T_2^* (measured by Ramsey interferometry) and the homogeneous dephasing time T_2 (measured by Hahn echo). In spin ensembles, T_2^* originates mainly from the random and (quasi-)static distribution of spin states and their interaction with the environment (bath). For single spins, T_2^* results mainly from experiment-to-experiment fluctuations in the spin bath state during averaging. In singles and ensembles, T_2 is obtained using a refocusing π pulse to suppress the static and slow fluctuations, and is, therefore, set by fast noise processes. In most relevant materials used for quantum applications, the electron spin T_2^* and T_2 are around a microsecond and a millisecond respectively, and can be extended to exceed seconds [64].

There are three material factors that can reduce this decoherence contribution: a low abundance of non-zero nuclear spin isotopes, low nuclear gyromagnetic ratios and host lattices that prevent nearest-neighbor coupling of nuclear spins of the same species.

Surrounding electron spins start to significantly contribute to T_2^* when their concentration reaches 10^{12} – 10^{14} cm^{-3}, corresponding to coherence times below seconds [64].

Magnetic fluctuations can also arise from the life-time of electron spins in the bath, $T_{1,B}$. At higher spin concentrations, spin state exchange, or flip-flop, between resonant spins becomes important, though it can be suppressed by local detuning, like magnetic field gradients. Through the modulation of specific spin parameters, electric field noise can also be a significant source of decoherence (see the section on spin control). T_2^* is

also susceptible to static variations from strain in the crystal. Finally, decoherence can also occur through rapid thermal excitation/relaxation into an excited state with spin parameters different from those of the ground state.

An increase of coherence time can be engineered by reducing the nuclear spin bath density through isotopic purification and by reducing the concentration of electron spins during crystal growth, defect creation and doping. Tuning the dimensionality (2D versus bulk) of the material can also improve decoherence, owing to the different spatial distribution of spins [65] .

Spin Control

A large variety of protocols are available to coherently control the electron (or nuclear) spin state [66] . Depending on the specific electron spin and orbital level structures of the defect, as well as the application at hand, each of these schemes — which include optical, magnetic, electric, and strain fields — has advantages and disadvantages. An electron spin (**S**) coupled to a nuclear spin (**I**) can be described by the following spin Hamiltonian:

$$H = \underbrace{\mu_B \mathbf{B}\cdot\mathbf{g_e}\cdot\mathbf{S}}_{\text{electron Zeeman}} + \underbrace{\mathbf{S}\cdot\mathbf{D}\cdot\mathbf{S}}_{\text{zero-field}} - \underbrace{\mu_N \mathbf{B}\cdot\mathbf{g_n}\cdot\mathbf{I}}_{\text{nuclear Zeeman}} + \underbrace{\mathbf{S}\cdot\mathbf{A}\cdot\mathbf{I}}_{\text{hyperfine}} + \underbrace{\mathbf{I}\cdot\mathbf{Q}\cdot\mathbf{I}}_{\text{quadrupole}}$$

where each bracket denotes a different spin interaction parameterized by the external magnetic field (**B**), the electron and nuclear spin g-tensor ($\boldsymbol{g_e}$, $\boldsymbol{g_n}$), the zero-field splitting tensor for **S** > 1/2 (**D**), the hyperfine coupling tensor (**A**, including both contact and dipolar terms) and the quadrupole tensor for **I** > 1/2 (**Q**) . μ_B and μ_N are the Bohr and nuclear magneton, respectively. Each parameter has a known microscopic origin, and ab initio calculations can predict their tensorial form.

Together with the magnetic field **B** in Eq. 4 , all the interaction tensors and transition frequencies can be controlled by local electric fields (**E**) and strain (**ε**) that perturb the electronic wavefunction, as illustrated in Fig. 2.6(a) . However, the interaction tensors

are affected by E and ε in different ways, depending on the symmetry and spin of the defect [67].

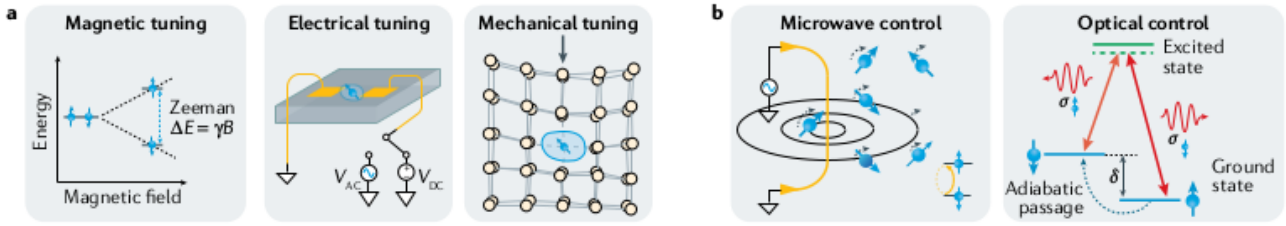

Figure 2.6. (a) Electron spin frequency tuning via external magnetic, electrical and mechanical fields. (b) Electron spin driving using magnetic (or other) fields at microwave frequencies (left). Optical control via an orbital excited state (right). σ indicates the circular polarization of light and δ is the ground-state spin transition frequency.

Microwave (GHz) frequencies are the ones typical of the electron spin resonance, and these frequencies are largely determined by the electron Zeeman interaction and zero-field splitting. Magnetic fields provide the simplest coherent spin control of $\Delta m_s = \pm 1$ transitions using microwave striplines and resonators (Fig. 2.6(b)) , though it is challenging to independently manipulate nearby spins. This may be solved using magnetic field gradients [49] or local detuning through electric fields [68] or strain [69] , for example.

Electric field modulation of the zero-field tensor results in $\Delta m_s = \pm 2$ transitions, whereas electric field modulation of the hyperfine interaction results in $\Delta m_s + \Delta m_I = 0$ (flip-flop) transitions.

Mechanical (phonon) control of the spin state works by creating local crystallographic strains (Fig. 2.6(a)) in a cantilever or acoustic resonator, for example, which allows for full ground state control of both the $\Delta m_s = \pm 1$ and $\Delta m_s = \pm 2$ transitions [67] . Typically, the spin–strain coupling is small. However, despite the potential trade-off of a reduced T_1, a strong coupling is preferred for quantum transduction between spins and phonons.

Ground state electron spin manipulation is also available by optical excitation, which utilizes the orbital excited-state levels as an intermediary. This enables the use of

optical techniques developed in the context of trapped ions and cold atoms [70], including coherent population trapping (CPT) and electromagnetically induced transparency (EIT).

For optical control, excited-state effects such as the optical lifetime, coherence and spectral hopping are all major sources of errors that limit control fidelities. Many methods have been developed to mitigate these issues, such as stimulated Raman adiabatic passage (STIRAP) and superadiabatic approaches. Optical control offers localized spin driving limited by the optical spot size of the excitation laser, and sub-diffraction control when combined with spectral resolution [71].

Nuclear Spin Registers

Besides being a source of decoherence for the defect's electronic spin, nuclear spins can act as key components for quantum communications [72], computation [73] and sensing [74]. Owing to the low magnetic moment of nuclear spins and their weak interactions with the lattice, these states can have extremely long spin coherences and lifetimes [54]. Nuclear spins can be divided into two categories: intrinsic nuclear spins, which are found inside defects containing impurity atoms, and extrinsic nuclear spins, which are found in the atoms around the electronic defect, primarily the host crystal's non-zero nuclear spin isotopes.

With the right choice of isotope during defect formation, every defect for intrinsic systems can deterministically host one or more corresponding nuclear spin registers. The hyperfine interaction for intrinsic nuclear spins can be large from the contact term. This usually results in a strongly coupled electron–nuclear spin system with nuclear spin-resolved transitions, depending on the electron spin linewidth, $\Gamma = 1/\pi T_2^*$.

However, to extend beyond one nuclear spin for each defect, extrinsic nuclei are necessary. They are also the only nuclear spins available for vacancy-related defects, which do not contain an impurity atom. Depending on Γ, extrinsic defects may result in a few strongly coupled nuclear spins for the first few adjacent sites in the lattice.

There are two broad choices for nuclear spin control: direct resonant driving or conditional phase accumulation, depending on the frequency shift Δω imparted by the hyperfine interaction with the electron spin (Fig. 2.7(a)). With the presence of this control, nuclear spin initialization by single-shot measurement or by swapping polarization with the electron are possible [75]. In strongly coupled electron–nuclear spin systems, Δω is large compared with Γ and the nuclear spin states are sufficiently resolved for direct magnetic driving of fully entangling two-qubit gates [73], consisting of electron–nuclear conditional rotations, as shown in Fig. 2.7(b). Spin selectivity here requires significant nuclear Zeeman interaction (high magnetic field), a quadrupole interaction or hyperfine differences between spin sublevels.

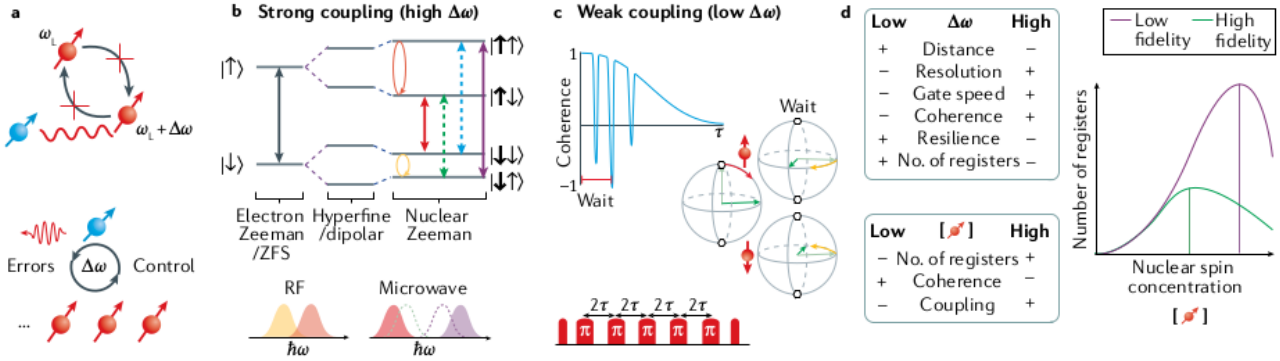

Figure 2.7. (a) Electron spin coupling to nearby nuclear spin registers in the environment. The detuning Δω of the coupled nuclear spin from the rest of the nuclear spin bath is a key parameter that reduces interactions with the bath, and also sets control mechanisms and accumulated errors on the nuclear register. ωL is the nuclear Larmor precession frequency. (b) Nuclear spin driving schemes using resolved conditional rotations for strongly coupled spins (high Δω). The dotted lines indicate forbidden transitions. RF, radio frequency; ZFS, zero-field splitting. (c) Ramsey and dynamical decoupling schemes for driving weakly coupled nuclear spins (low Δω), where nuclear spin-dependent phases are accumulated and projected. τ, lifetime. (d) Trade-offs involved in the choice of hyperfine strength (Δω) and nuclear spin concentration (left) in terms of the positives and negatives (+ and −) and high and low values. The nuclear spin bath concentration must be chosen carefully for high-fidelity control and the number of nuclear spin registers (right) .

The second way to mediate two-qubit gates is by creating an electron spin superposition and accumulating a nuclear spin-dependent phase (Fig. 2.7(c)). The spin state selectivity is similarly limited by the spin's T_2^* and requires a hyperfine interaction that is faster than the dephasing time. Extending the number of registers to include weakly coupled nuclear spins with small frequency shifts Δω can be achieved with dynamical decoupling-based control. This extends the T_2^* limit to T_2 by canceling

all interactions with the environment but those at a frequency set by the inter-pulse spacing of the decoupling scheme (Fig. 2.7(c)) .

Gate speeds from a few microseconds to a few milliseconds are produced by both strategies. They have allowed for the control and entanglement of more than ten nuclear spin registers [54], as well as proof-of-principle error correction [73,75] for quantum computing and communications, along the ability to resolve single nuclei at a few nanometres distance [76] for quantum sensing.

The interplay between the hyperfine interaction strength and the isotopic abundance is critical (Fig. 2.7(d)). This channel of decoherence at strong magnetic fields can also be avoided by manipulating a nuclear spin species that has a different gyromagnetic ratio than the bath spins. Isotopic purification increases both the electron and the nuclear spin coherence times, yet, reduces the availability of nuclear spins that can be used. Conversely, at high nuclear spin concentrations, the ability to resolve nuclear spin transitions is limited by spectral crowding [73] , which reduces the two-qubit gate fidelities.

2.2.2 Optical Properties

Materials research for defects with the best optical properties is driven by the optical addressability of numerous spin defects, which offers a photonic interface for quantum applications. Though electrical (see the section on the spin–charge interface) and other methods exist to initialize and read out the spin state, an optical interface is generally desired for its practical ease of use and for the possibility of isolating single defects. An efficient interface requires understanding the major optical parameters of a spin defect, including the emission spectrum, quantum efficiency and spin-dependent optical contrast.

Optical Emission and Excitation

The emission wavelength is a basic property that influences factors such as the attenuation through various media and the required detector technology. In order to minimize optical fiber losses for quantum communication, infrared photons are preferred (Fig. 2.8(a)). This has sparked interest in defects that emit in the telecom band.

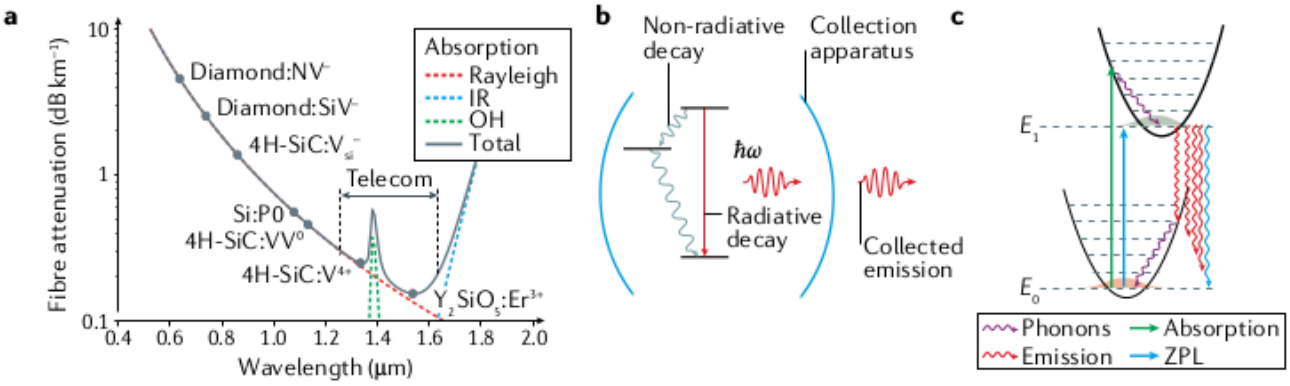

Figure 2.8. (a) Attenuation loss as a function of wavelength in an optical fiber . Typical defect emission wavelengths are shown to compare their viability for quantum communication (without frequency conversion). IR, infrared; OH, hydroxyl ions. (b) Radiative and non-radiative emission of a defect in a collection system, such as free-space optics or photonic cavities. (c) Phonon-assisted and zero-phonon line (ZPL) absorption and emission from defect orbitals, showing the harmonic vibration potentials in a Franck–Condon diagram. E_0 , lowest ground-state energy; E_1 , lowest excited-state energy.

Likewise, applications in biosensing are optimized around 1000 nm in the 'second biological optical window' dictated by low photon absorption in saltwater.

For integrated, low-cost applications, silicon detectors operate optimally at 400–1000 nm, whereas high quantum efficiency can be achieved with superconducting nanowires in the infrared, at a higher cost.

A desirable emission wavelength can be engineered by sum and difference frequency conversion using nonlinear optical phenomena such as spontaneous parametric down-conversion (SPDC) and spontaneous four-wave mixing (SPWM), often in a periodically-poled material. When mixing single photons, however, Raman scattering

and other sources of scattering can produce noise in the output band of interest, depending on the chosen input pump wavelengths. Importantly, these techniques can preserve the phase coherence of the input photons, which is required for entanglement protocols.

Since it determines the experimental signal intensity, the photon count rate of single-photon sources, the sensitivity of the defect as a quantum sensor, and the entangling rate for quantum communication, the photon emission rate is a crucial component of optically active defects.

The photon count rate is dictated by the radiative rate from the excited state, but is reduced by non-radiative rates and experimental collection efficiencies (Fig. 2.8(b)). Efficient collection can be addressed via solid immersion lenses and surface metalenses that reduce the effect of total internal reflections. Alternatively, photonic waveguides can enable direct fiber coupling of the light [48]. The photon generation rates can be enhanced by using small-mode-volume, low-loss cavity structures with a high Purcell factor to reduce the excited state lifetime.

The emitted photons are spectrally divided into a narrow zero-phonon line (ZPL) and a broad phonon sideband (PSB) (Fig. 2.8(c)). The Debye–Waller factor (DWF) is the key quantity that describes the ratio between the ZPL emission intensity and the overall emission intensity. A low DWF is often due to a strong phonon coupling, resulting in decay between the excited state and the higher phonon modes of the ground state. Applications that require photon coherence or interference benefit from a dominant narrow ZPL spectral contribution (high DWF) that contains indistinguishable photons. Nanophotonic cavities provide an engineering pathway for increasing the ZPL emission and the DWF.

Quantum efficiency (QE) is another key parameter for assessing the performance of an optical emitter. QE is the fraction of excitation events that result in the emission of a photon, and is lowered by non-radiative and ionization rates. The QE can be obtained indirectly by comparing the measured optical lifetime to the radiative rates calculated

with density functional theory (DFT) or by combining master equation modeling and experimental spin-dependent transient decays. Direct experimental measurement of the QE can be achieved by controllably varying the photonic density of states [77]. Similarly, Purcell enhancement can improve the QE by changing the balance between the radiative and non-radiative rates.

Spin-Photon Interface

For spin-based quantum information, the spin-dependent optical processes of defects are crucial characteristics. Without them, light could not be used to polarize, control or read out spins. There are two main ways that the spin of a defect can influence the coupling to light: optical transitions with spectrally or polarization-resolved spin states or via an intersystem crossing (ISC) with spin-dependent non-radiative processes. Both of these processes unlock optically detected magnetic resonance (ODMR) of the spin state of the defect.

In the first case, optical polarization (linear or circular) can lead to different optical selection rules depending on the spin state and, hence, to spin-dependent excitation and emission of photons. Alternatively, spin selectivity is obtained when two or more spin states in the ground state have different optical transition frequencies to one or more spin states in the excited state (Fig. 2.9) .

This frequency resolution requires that the optical linewidth is narrower than the spin-dependent optical shift.

Spin-dependent frequency differences between orbital ground and excited states can arise from different electronic wavefunctions and corresponding spin interactions. This includes differences in the g-factor (such as in Si vacancies in diamond [78]), hyperfine or zero-field tensors (for $S > 1/2$, such as the NV center in diamond [79] or vacancy centers in SiC [80]).

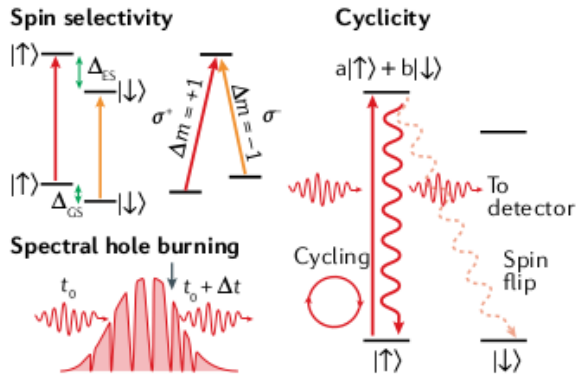

Figure 2.9. Spin-selective optical transitions can occur as spin-resolved optical transitions from frequency detuning (left) or as a non-conserving spin transition using polarization selection rules (right). Spectral hole burning in ensembles is used for controlled single-photon storage. Cyclicity is defined by the spin mixing in the excited state, which causes spin-flip transitions. The red wavy arrows represent the absorption and emission of photons. Δ_{ES} , excited-state spin transition frequency; Δ_{GS} , ground-state spin transition frequency; $\sigma^{+/-}$, circular polarization of light; m, spin projection.

For many applications, the spin eigenstates must remain identical between ground and excited states, otherwise the defect would suffer from non-spin-conserving radiative decay from the excited state (Fig. 2.9). A low spin-flip probability is desired to create so-called 'cycling' transitions, in which, upon excitation and emission of a photon, the defect is returned to its initial spin state. With this, photons can be continuously extracted from the defect with high correlation to the spin state, which is critical to the fidelity and verification of spin–photon entanglement for quantum communication protocols.

Unfortunately, many of the mechanisms that provide spin-selective optical transitions can also contribute to mixing of the spin eigenstates. For example, in some diamond and SiC defects, the axial spin–orbit term λ_z creates the frequency splitting needed for spin–photon entanglement, whereas the transverse spin–orbit mixing $\lambda_\perp$ degrades the spin selectivity of the transitions and reduces the cyclicity. Additionally, mixing of the spin eigenstates can be reduced/increased by controlled/uncontrolled magnetic fields, electric fields and strain, while Purcell enhancement can increase the cyclicity by changing the balance between different radiative rates [81] .

To optically polarize and control the spin ground state, on the other hand, non-spin

conserving transitions are necessary.

Without spin-selective optical excitations, the alternative pathway for optical spin readout and polarization is via spin-dependent non-radiative processes such as ISCs. ISCs are non-radiative transitions between orbital levels with different spin multiplicity but the same symmetry, and they are mediated through phonons and the spin–orbit interaction (λ).

The addition of spin-dependent non-radiative rates, as well as intermediate orbital 'shelving' states in the ISC, results in spin-dependent emission probability of a photon during the optical cycle (Fig. 2.8(c)) . This core feature allows for ODMR, in which the spin–photon interface may be unresolved, such as in room-temperature and quantum sensing applications.

The spin dependence of non-radiative processes depends on the temperature of the system. For the ISC, the potential energy surface (PES) of the states for each spin multiplicity can be calculated as a function of the nuclear coordinates of the defect. If an energy barrier (W) exists between PESs with different multiplicity, then direct transitions between these PESs at their crossing point are unlikely [82]. However, thermal crossing through the barrier can eliminate the spin dependence of the non-radiative ISC rates while also lowering QE [82]. Thermal activation through this process modifies the radiative lifetime τ as a function of temperature T as follows [82]:

$$\tau(T) = \frac{\tau_0}{1 + s \cdot e^{-\frac{W}{k_b T}}}$$

where *s* is the ratio of non-radiative to radiative rates at the PES crossing point and τ_0 is the optical lifetime at absolute zero temperature. Therefore, by knowing the relative rates and lifetimes of the system, the optical illumination and readout durations can be optimized for the highest ground-state spin polarization, contrast and number of extracted spin-correlated photons,relating to the signal-to-noise ratio. Finally, it is important to note that the properties yielding a desired ISC often conflict with an ideal radiative and spin-conserving spin–photon interface. Additionally, the mixing from the

presence of an ISC, by definition, reduces the state purity of the defect's spin.

Optical Coherence

Aside from ground-state spin coherence, the coherence of the orbital transitions has important consequences for quantum technologies. Resonant read-out protocols, spin initialization, optical spin control, and signal-to-noise ratio for quantum sensing can all suffer from reduced optical coherence. Critically, the coherence of an emitted photon directly influences the fidelity and entanglement rate of quantum communication protocols. These factors lead to some applications favoring the best optical performance over the best spin properties [83].

For optical transitions, the relevant coherence for single emitters is usually the optical T_2^* or, inversely, the optical linewidth Γ. An optical emitter with a lifetime τ has a best-case 'lifetime-limited' or transform-limited homogeneous linewidth (full width at half maximum, Fig. 2.10(a)) of:

$$\Gamma_0 = \frac{1}{2\pi\tau}$$

This optical linewidth reflects the coherence of the emitted light from the defect, which can also be measured directly through the decay of optical Rabi oscillations, (Fig. 2.10(b)). Additional non-radiative processes can shorten optical lifetimes and, therefore,

increase Γ (Fig. 2.10(c)). With two perfectly indistinguishable emitters, coherent interference between two emitted photons on a beam splitter erases the path information of the photons and causes a Hong–Ou–Mandel interference dip (Fig. 2.10(d)), enabling heralded entanglement [84]. This photon-mediated interaction is the key mechanism by which spin defects can produce and distribute entanglement at long distances. With imperfect emitters, the reduced phase coherence of the photons drastically decreases the entanglement rates and fidelities achievable with defect spins.

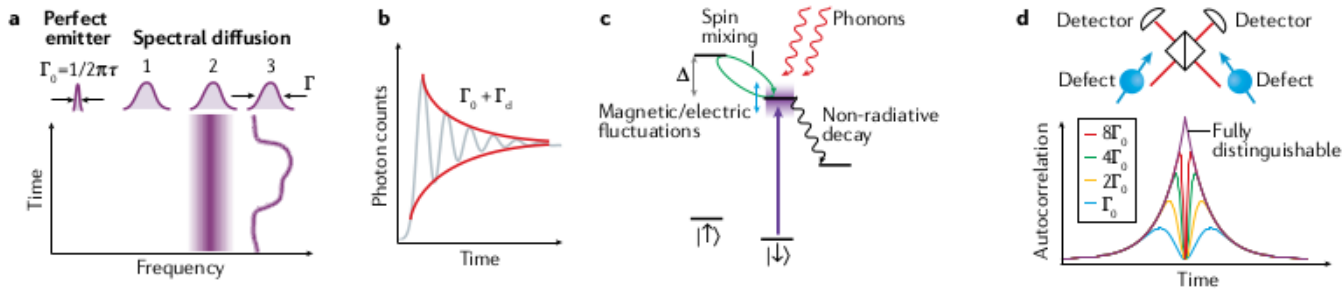

Figure 2.10. (a) Various types of spectral diffusion depending on the noise correlation time: (1) discrete spectral jumps, (2) Gaussian broadened line ($\tau_c < \tau$) and (3) spectral wandering. Γ_0 is the full width at half maximum optical linewidth and τ the lifetime. (b) Decay of optical Rabi oscillations through time-resolved fluorescence. Γ_d is an additional decoherence contribution. (c) Possible mechanisms for orbital decoherence and decay. (d) Hong–Ou–Mandel interference between emitted photons from two defects at a beam splitter. A correlation dip is formed for indistinguishable emitters and is degraded with increased linewidth Γ.

A defect's orbital structure can undergo multiple types of broadening, depending on the correlation time of the noise (τ_c) and the noise source.

Spectral diffusion refers to broadening from environmental noise that is slow compared with the optical lifetime, whereas pure dephasing occurs from noise that is fast compared with the emitter's lifetime.

Similar to the spin T_1 , a small spin–orbit coupling and large Debye temperature are desired to maintain a lifetime-limited optical line at the desired temperature.

2.2.3 Charge Properties

The charge properties of spin defects in the solid state are fundamental to their reliable use, as well as for electrical readout of the spin state. Studying these properties was instrumental to the development of classical condensed matter and semiconductor physics. However, the focus in quantum science is on specific defects and how they can be used, and not on the overall transport properties, as is often the case for classical electronics.

Charge State

The negatively charged NV center in a diamond is one example of a well-known spin defect that corresponds to a specific charge state. In contrast, a different charge state results in radically different spin and optical interfaces. It is, therefore, critical that the charge state is initialized on demand and is stable during qubit operation. The first condition ensures that a large fraction of a defect ensemble contributes to the signal and a lower fraction contributes as a dephasing spin environment, both being important aspects for sensing applications. For single spins, a known initial charge state is essential for more complex applications such as single-shot readout and deterministic entanglement [84]. The second condition prevents an additional T_1 relaxation channel from random charge state switching, while the stability of surrounding defects in the host reduces the intensity of electrical and magnetic noises that deteriorate the spin and optical coherences.

Charge stabilization can be achieved through laser control. The defect might be stabilized if the laser wavelength that excites the optical transition can simultaneously repump to the right charge state [85]. In addition to optical manipulation, electrical techniques such as depletion engineering or high electric fields can be used to control the amount of local charges and the various ionization and capture rates. Finally, charge control can enable applications such as electrometry [86], super-resolution imaging [87] and control of defect formation kinetics [88].

Spin-Charge Interface

Readout for defect spins is not limited to ensemble spin resonance (inductive read-out) or purely spin-dependent optical measurements. Spin-to-charge conversion (SCC) allows the spin state of a defect to be mapped to the presence or absence of charges. SCC can proceed by means of spin-dependent optical processes when an optical interface is present. SCC can happen in the case of defects lacking an optical interface

by recombination with nearby traps, tunneling to a quantum dot or reservoir of charges [56], or using polarized conduction electrons. Fig. 2.11(a) provides an illustration of these procedures.

Independent of the SCC mechanism, electrical read-out can occur through a variety of techniques (Fig. 2.11(b)). A photocurrent or changes in a device's capacitance caused by variations in the trapped charge in a semiconductor [45] can be used to perform a spin-dependent readout directly. Charge sensors such as single-electron transistors can measure single charges [56], so host crystals with this device capability are desired.

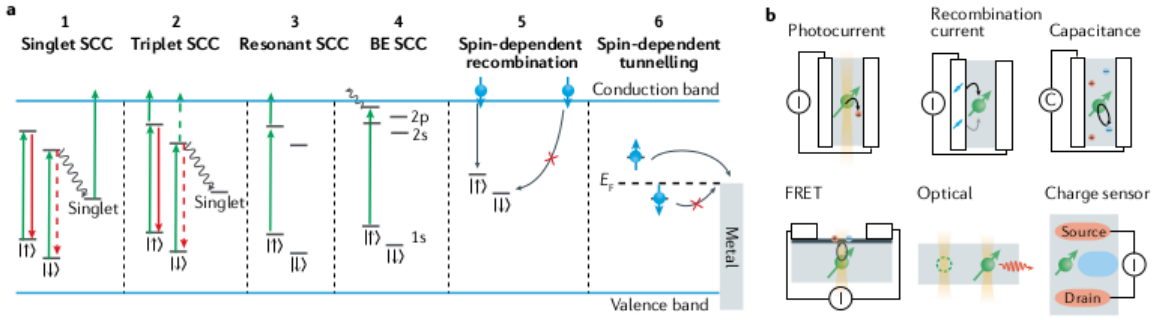

Figure 2.11. (a) Multiple examples of spin-to-charge conversion (SCC): (1) spin-dependent two-photon ionization through spin-dependent shelving; (2) two-photon ionization with a spin-dependent lifetime modification; (3) two-photon ionization with spin-dependent optical transitions; (4) bound exciton (BE) SCC with either a two-photon, thermal or Auger ionization process; (5) spin-dependent capture of a free carrier to a trap; and (6) spin-dependent tunneling. (b) Electrical readout devices: from top left to bottom right, photocurrent readout after spin-dependent defect ionization, spin-dependent recombination, spin-dependent charge/capacitive sensing after ionization, Förster resonance energy transfer (FRET) between the defect and a secondary system, fluorescence readout of the presence or absence of a particular defect charge state and single-charge sensor/single-electron transistors with spin-dependent tunneling.

2.2.4 Material Properties and Outlook

Spin defect qubit properties are interwoven with the intrinsic host material properties, including variations in crystallographic, dopant and nuclear-spin imperfections in their local environment.

The identification, creation and localization of defects remains a key challenge for the integration of these defects with optical devices, nanostructures and other spatially dependent applications. The ability to create localized defects must be achieved without introducing significant damage that would negatively affect the defect's spin, optical

and charge properties. In summary, the selection of host materials should consider not only the properties of the spin defect but also the scalability (for example, wafer availability), ease of fabrication and unique properties (such as low acoustic loss) of the host.

There are many trade-offs to take into account about spin, optical, charge, and material properties. The fundamental balance for any parameter is between control and coherence of the defect system.

The main challenge for the field is, therefore, finding a material host and defect for the specific application at hand. The major limitations for quantum communications are in creating indistinguishable photons at ideal wavelengths and in nanophotonic integration, whereas for quantum sensing, the signal-to-noise ratio and the effect of nearby surfaces determine the performance. Quantum computation faces the largest hurdles in terms of engineering interactions between nearby spins to create two-qubit gates.

Solid-state spin defects are already being deployed in commercial applications such as quantum sensing, and the continued progress and understanding of their interconnected properties is vital to fulfilling the full promise of defect-based quantum systems and their future in quantum technologies.

Chapter 3

Experimental Details

In this chapter the experimental details of laser fabrication and characterization of waveguides are discussed in detail. In the first paragraph, a description of the experimental setup used to perform the fabrication is illustrated, including the technical specifications of the femtosecond laser source, the optical path and a step-by-step breakdown of the actions needed to operate the system. The second paragraph deals with the theory and techniques behind the characterization of the fabricated devices, i.e. the measurement of parameters that define the performance of the device like the Mode Field Diameter and the Insertion Losses. The last section contains a brief overview of the setup used to take microRaman spectra by the joint research group at CNR-IFN, Trento.

3.1 Micromachining System

In this work, the development of quantum devices relies mostly on the fabrication of photonics structures and color centers in bulk materials through femtosecond laser irradiation. With this purpose, a laser writing system's simplest configuration should include a suitable high power femtosecond laser source that is focused into a sample mounted on a 3-axis stage using a microscope objective. However, additional optics for beam shaping, polarization control and power tunability of the source and an imaging system for alignment and supervision of the fabrication can be used to achieve a better

control of the several parameters playing a role in the process. The Felis laboratory in Lecco served as the primary laser micromachining station for this thesis' experiments.
In particular, a Yb:KGW BlueCut fiber laser is used as the main source (Menlo Systems, Germany), being an all-fiber integrated laser system that is designed for industrial use and is inherently reliable and stable. It delivers pulses at 1030 nm with 300 fs pulse duration with a peak pulse energy of 10 μJ and a tunable repetition rate from single pulse to 10 MHz. Figures 3.1 and 3.2 depict the beam path along the setup.

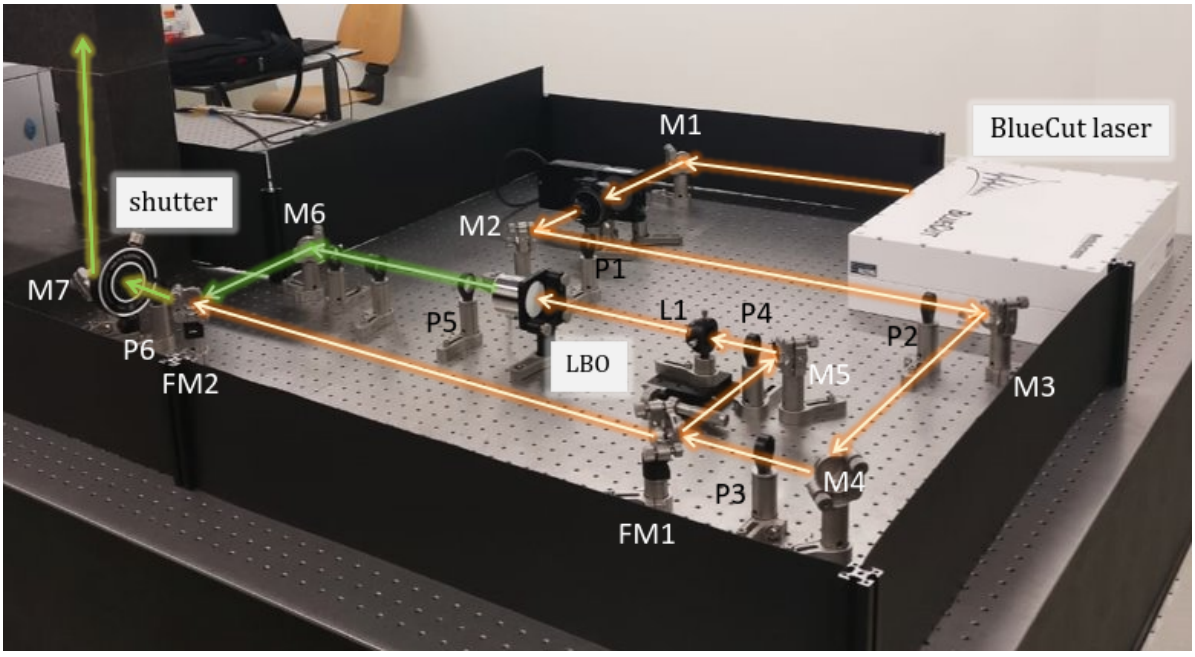

Figure 3.1. Optical beam path at Felis lab, showing the femtosecond laser source, the intensity modulation stage and the second harmonic generation stage

Silver-coated mirrors mounted on extremely stable and precise Polaris mounts (Thorlabs) are used to steer the beam. Both polarization and power control of the laser beam are possible through a half-wave plate and polarizer. The beam is directed onto the optics on the top breadboard by a 45° mirror M5. The last dichroic mirror, M7, steers the light towards a microscope objective that is mounted on an Aerotech ANT130-L-ZS air bearing stage, allowing for vertical z-axis displacement of the objective.

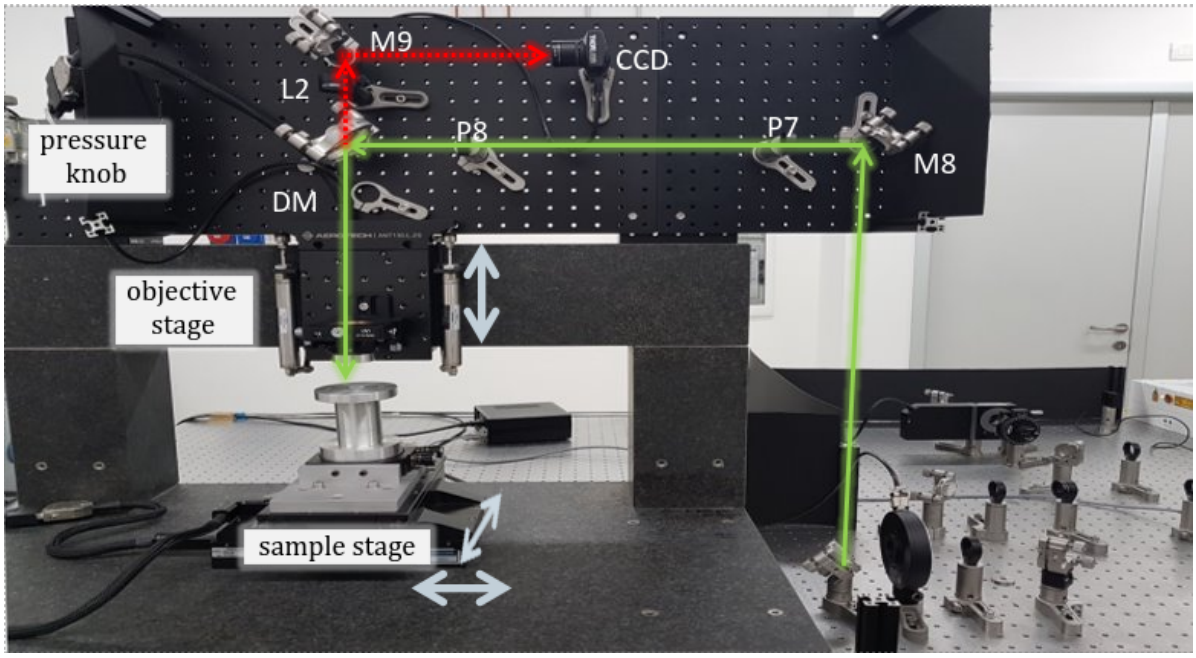

Figure 3.2. Optical beam path at Felis lab, showing the CCD camera, the objective stage and the sample stage.

The sample is positioned on an Aerotech ANT130-110-XY stage that enables translations along the x and y axes, i.e. along the plane of the optical table. To compensate for any tilt that might occur during sample placement, a second gimbal stage is used to hold the sample. The final dichroic mirror DM (065-5103, EKSMA optics) has a reflectivity of 99.5% for 1030 nm and 515 nm. In order to visualize the back-reflected laser beam and locate the focal plane on the sample's surface, a CCD is positioned behind the dichroic mirror DM. The CCD also enables real-time imaging of the sample features and the plasma produced by the laser during fabrication. Menlo Systems' laser interface software gives users control over the internal shutter, internal attenuator and repetition rate. The Aerotech stages are programmed in the Aerobasic compiler provided by the manufacturer using the Aerocode language. The Scope in the software enables real-time parameter monitoring of the stage motion thanks to additional feedback from the stages. In order to have a user-friendly single software control over the various available parameters, additional integration and bridging work is being done.

Moreover, it is possible to use the second harmonic wavelength of the fundamental

(515nm) by flipping a mirror and sending the beam through a lens and an LBO crystal, before reaching a second collimating lens and be realigned with the fundamental path. This enables fabrications with higher energy photons with respect to the fundamental, necessary for certain experiments.

A detailed procedure for the fabrication process is reported below:

It is needed to turn on the BlueCut laser by following the instructions in the laser manual and using the desktop's laser control software. Note that in the laser interface software, the oscillator must be turned on first, then the repetition rate of interest must be chosen, and finally the amplifier must be turned on.

The compressor for the z-stage must first be opened in order to enable the stages. Just enough pressure to balance the weight of the stage should be applied to the air bearing z-stage using the pressure control knob, as shown in Figure 3.1. This can be achieved by manually positioning the z-stage so that it remains in the middle of its travel range and does not move when pressure is applied.

The Aerotech stages then need to be enabled using the Aerotech software.

The output power of the laser can be measured for reference, after it has warmed up sufficiently, by positioning the power meter immediately after the output aperture.

A suitable power can be selected for secure beam alignment by adjusting the amplitude percentage in the laser software and consequently the internal attenuator of the laser. It has been determined that a 2% amplitude percentage setting at a 500 kHz repetition rate is safe. The polarization and power of the laser can be adjusted by rotating the assembly of the half wave-plate and polarizer.

Because the polarizer is a prism, it should be noted that rotating it alters the alignment of the beam at the output. To keep the alignment unaffected, it is preferable to rotate the half wave-plate for power control.

The LBO crystal used for second harmonic generation is based upon a temperature tuning phase matching, for this reason it is contained within a special oven that has to be turned on and reach the equilibrium temperature required for operation.

The mirrors M1 and M2 can then be used to align the beam along the pinholes P2 and P3.

Mirrors M3 and M4 can also be used to align the beam through pinholes P3 and P6, in order to direct it toward the 45-degree mirror M7.

To operate with 515 nm wavelength, the two flip-mirrors FM1 and FM2 have to be raised, then the beam must be aligned through pinholes P4 and P5 using mirrors FM1 and M5, and through pinhole P6 using mirrors FM2 and M6.

To direct the beam onto the dichroic mirror M7, the beam must be aligned through the pinholes P7 and P8 using mirrors M7 and M8.

By manipulating the X and Y controls of the objective holder stage, it is possible to align the beam so that it passes through a pinhole inserted at the center of the objective holder on the z-stage.

A mirror can be mounted on the objective stage, so that the back reflection can be seen through a pinhole in P7 to control the tilt of the objective stage. The back-reflected beam can be aligned to pass through the pinhole's center by adjusting the tilt, ensuring that the objective stage is perpendicular to the incident beam.

By mounting a mirror on the sample stage and adjusting the gimbal movement along the horizontal and vertical tilts, it is also possible to change the tilt in the sample stage.

The chosen objective can then be mounted onto the objective holder following the alignment of the optical path, and the sample can then be set down on the sample stage.

A low power laser beam can be used to align the objective's focal plane with the sample's surface, and mirror M9 will reflect the objective's back-reflected beam onto the CCD so that the image at the focus can be seen. The beam can be focused on the top surface of the sample by adjusting the z-stage using the aerotech control software, producing a sharp and intense dot on the CCD image. By estimating the focal distance using the working distance specified for the relevant objective, a preliminary coarse adjustment can be made.

By measuring the laser beam power just before the objective and adjusting the half

wave-plate, the appropriate power needed for fabrication can be obtained. Using the Aerotech compiler, the stage can be programmed for a specific motion.

The z-stage can be raised once fabrication is complete in order to provide a secure distance from which to remove the sample holder. Before turning the compressor off, care should be taken to manually lower the z-stage to its lowest setting after disabling the stages.

The amplifier must be turned off first, then the oscillator, in order to turn off the laser.

3.2 Waveguide Characterization

Once the fabrications have been performed, it is necessary to characterize qualitatively and quantitatively the performances of the resulting devices. Depending on the type of fabrication and the application considered, different properties of the system might need to be studied. In this subsection, the characterization techniques required to study laser-written photonic devices in diamond is briefly discussed.

3.2.1 Optical Mode Characterization

Background

The mode field diameter (MFD) is one of the primary characteristic parameters of any waveguided Gaussian beam. It is mathematically defined as the diameter at which the power density is reduced to $1/e^2$ of its maximum value. The output mode is typically imaged onto a beam profiler using a microscope objective to magnify the optical mode and fill a larger portion of the detector screen in order to measure the MFD of a guided mode. The intensity image profile of the mode is provided by the beam profiler, and further analysis of the mode can be done to determine its MFD. The analysis of the beam profiles propagated through the fabricated waveguides give a first qualitative estimation of the guiding properties of the waveguides. However, for a quantitative study the optical loss in transmitted power has to be considered. The term insertion loss (IL) refers to the total loss caused by the insertion of the optical device. The waveguide insertion loss can be determined using the fiber coupled characterization technique by measuring the power transmitted, P_t (in dB), through the laser-written waveguide by butt-coupling a single mode fiber at both the input and the output facets of the waveguide and normalizing to the reference power, P_{ref} (in dB), measured by direct butt-coupling of the input fiber to the output fiber. Mathematically the equation yielding the insertion loss, where the reference power and the transmitted power are both expressed in dB, is:

$$IL(dB) = P_{ref} - P_t$$

The coupling loss (CL) resulting from the mismatch in the mode field diameter of the optical fiber and the laser written waveguide are included in the insertion loss along with the propagation loss along the length of the waveguide. The overlap integral of the two modes, as in the following equation, provides the coupling efficiency.

$$\eta = \frac{|\int_{-\infty}^{\infty} \Psi_1(x,y)\Psi_2(x,y)dxdy|^2}{\int_{-\infty}^{\infty} |\Psi_1(x,y)|^2 dxdy \int_{-\infty}^{\infty} |\Psi_2(x,y)|^2 dxdy}$$

where, $\Psi_1(x,y) = Ae^{-\frac{x^2+y^2}{a^2}})$ is the electric field distribution of the Gaussian beam from the single mode fiber with an MFD of 2*a* and $\Psi_2(x,y) = Be^{-(\frac{x^2}{d_x^2}+\frac{y^2}{d_y^2})}$ is the electric field distribution of the laser written waveguide mode assumed to be elliptical with a MFD of $2d_x$ and $2d_y$ along x and y axes respectively. Substituting the generalized form of $\Psi_1(x,y)$ and $\Psi_2(x,y)$ in the equation of the coupling efficiency, a logarithmic equation for the coupling loss can be obtained as in equation 3.3 .

$$CL(dB) = 10\log_{10}\frac{4a^2 d_x d_y}{(d_x^2+a^2)(d_y^2+a^2)}$$

Substituting the MFD $2d_x$ and $2d_y$ measured using the beam profiler in the equation above, the CL can be calculated.

The power loss resulting from scattering and absorption along the length of the waveguide is known as the waveguide propagation loss, which is expressed in dB/cm. The fringe contrast in the Fabry-Perot cavity, which is caused by the refractive index mismatch between the fiber and the sample surface, is typically used to determine the propagation loss. As an alternative, the propagation loss can be calculated indirectly by taking into account the insertion loss and the coupling loss with the formula:

$$\alpha(dB/cm) = \frac{IL - 2CL}{L}$$

where, IL and CL are in dB and L is the length of the waveguide in cm.

Experimental details characterization of the optical mode

The heart of all photonic devices is the simple optical waveguide. After the waveguide is created using a femtosecond laser, basic optical microscope characterization is carried out to understand more about the physical changes made to the material.

One can determine the size of the laser-induced modification and the sign of the refractive index change using optical microscopy. Optical microscopy can be used to find promising optical waveguides, and after that, light can be launched into the structures to examine their transmission characteristics. In order to quantitatively analyze the guiding behavior, the near field mode profile is typically captured as the first step in waveguide optical characterization. The simplest method for achieving this goal is to fiber-couple the input facet of the waveguide using a regular fiber connected to a laser emitting at the desired wavelength. The waveguide and fiber are positioned using high-resolution three-axis manual positioners. A vision system for better alignment can be used with an overhead microscope with CCD.

An alternative is to use a microscope objective at the waveguide's input facet to free space end-fire couple the laser light.

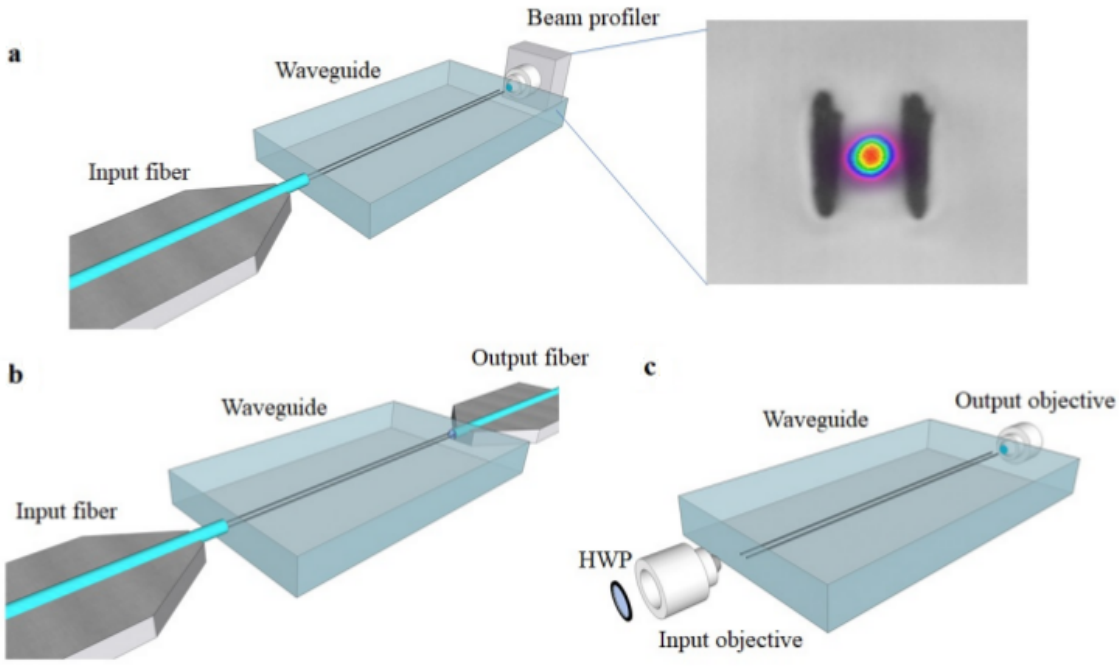

Figure 3.3. Chapter-36. Schematic showing various characterization configurations. (a) Fiber end coupled to the input facet of the waveguide and the output mode imaged onto a beam profiler, showing a typical side view microscope image with the optical mode in the inset for a type II waveguide in diamond. (b) Insertion loss measurement with fibers butt-coupled at the input and the output facets of the waveguide (c) Polarization-sensitive insertion loss measurement using free space optics consisting of microscope objectives at input and output and a half wave plate at the input to control the polarization of the input beam.

As shown in Figure 3.2(a), the guided mode can be imaged onto a beam profiler at the output to determine the near-field mode profile. By coupling the output to an optical power meter, either through fibers as shown in Figure 3.2(b) or free space optics for a polarization-sensitive transmission measurement, as shown in Figure 3.2(c), the transmitted optical power through the waveguide can be measured to determine the insertion loss. Due to the complexity of the refractive index profile, depending on the laser-writing conditions, one can produce a waveguide with a single mode, higher order modes, or even a waveguide with multiple guiding locations. Finding the mode field diameter (MFD) of the guided mode in single mode waveguides is helpful because it allows one to calculate the coupling loss. Based on the measured insertion loss, one can calculate the propagation losses of the waveguides by measuring the output power in relation to the input power.

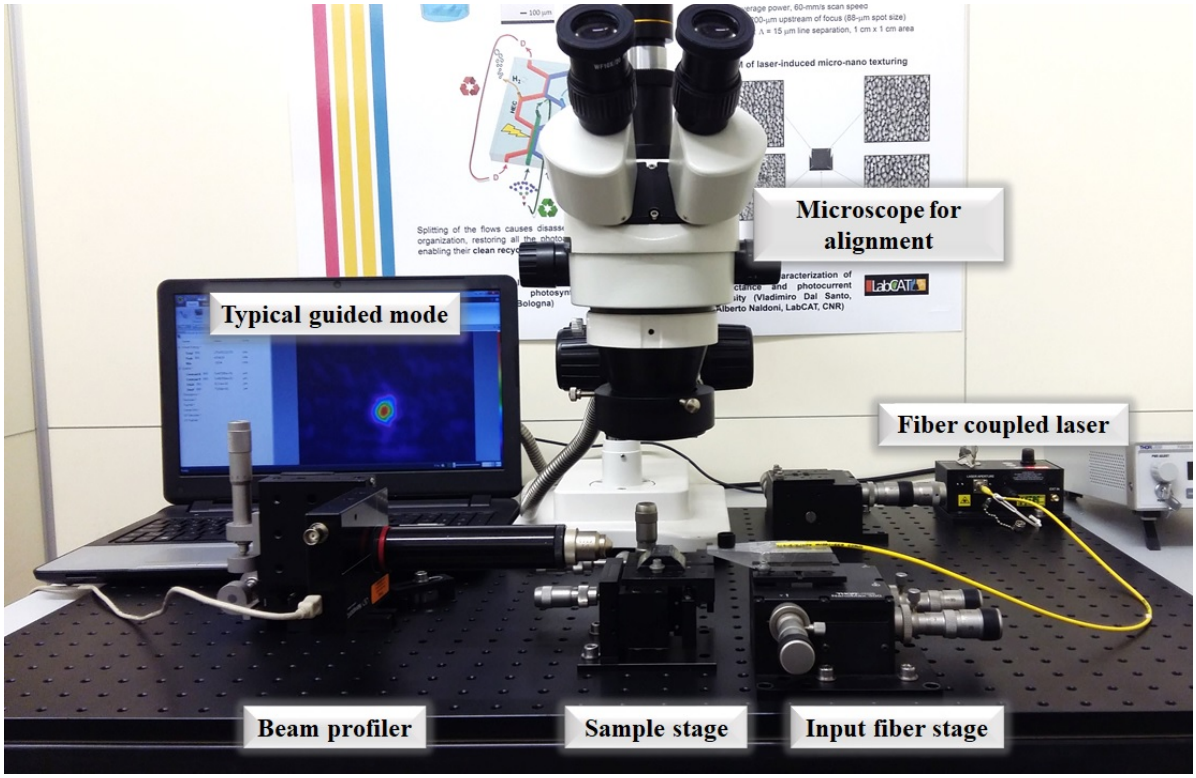

Figure 3.4. Characterization setup at Felice lab

The optical characterization was performed in the Felice lab at Dipartimento di fisica, Politecnico di Milano. Waveguides for various applications were characterized using fiber coupled laser sources at wavelengths of 635 nm (TLS001-635, Thorlabs), 808 nm (S1FC808, Thorlabs), and 1550 nm (TLS001-1550, Thorlabs). For the specific wavelengths of the aforementioned laser sources, suitable fibers for single mode operation were available (Thorlabs SMF-28 for 1550 nm, Thor-labs SM600 for 635 nm and Thorlabs 780HP for 808 nm). For input and output fiber coupling, high resolution 3-axis manual positioners (Nanomax MAX313D, Thorlabs) were employed. Using a 4-axis manipulator, the sample stage was moved transversely to switch between various waveguides (MicroBlock MBT401D, Thorlabs). High magnification aspheric lenses were used to image the mode onto the beam profiler (5721-H-B,Newport). The beam was profiled using Spiricon SP620U and SP620U-1550 (Ophir) at the visible and telecom wavelengths, respectively. Using the 4-sigma technique, which is a

measurement of four times the standard deviation of the energy distribution evaluated along the transverse plane, i.e. the x and y axes separately, the Spiricon software provided the option of determining the MFD of the mode. Fiber-coupled power meters 818-SL and 818-IG-L from Newport were used to measure the power transmitted along the waveguide at the visible and telecom wavelengths, respectively. In Figure 3.3, a typical lab characterization setup is depicted. The alignment of the optical fibers with the waveguides in the sample can be done precisely using an overhead microscope. We can analyze the guided beam's modes using the Beamgage software created by Ophir Photonics.

3.2.2 Micro Raman Characterization

The micro-Raman characterization was performed in the laboratory of Prof. Maurizio Ferrari and Dr. Andrea Chiappini at CNR-IFN, Trento, Italy. A Labram Aramis Jobin Yvon Horiba microRaman system with a 532 nm DPSS laser source was used to record the various micro-Raman spectra. A confocal microscope and an air-cooled CCD are also included in the system to collect photoluminescence signals. The beam was focused into the sample and the Raman signal was collected using focusing objectives of 50 and 100, respectively, providing a spatial resolution of about 1 m. The grating used in the spectrometer determines the system's resolution. A 1800 line/mm grating found in the spectrometer can be used to obtain a wavenumber accuracy of roughly 1 cm^{-1}.

Chapter 4

Diamond Quantum Photonics

4.1 Motivation

As discussed in Chapter 2, diamond is a very powerful platform for quantum computing, sensing and communication, where the improvement of the optical collection efficiency from the color centers has been one of the main challenges for the development of diamond-based quantum devices. The main limitation is given by the high refractive index (2.4), which causes a small angle of total internal reflection (TIR) at the diamond-air interface, reducing the collection efficiency of color center emission from the bulk when using a microscope objective (as represented in Figure 4.1(a)). The use of an index-matching oil to reduce the refractive index mismatch is a common practice during the femtosecond laser fabrication process, but is undesirable for the measurements because the oil is incompatible with low temperatures. This issue has been partially solved by a number of strategies. One of the approaches is based on the etching of diamond micro-cylinders [89], nanowires [90], nano-pillars [91], nano-beams [92], and nano-waveguides [93] onto the diamond surface. In order to increase the outcoupling efficiency, solid immersion lenses have been created using a focused ion beam (FIB) [94]. However, their performance is highly sensitive to surface roughness and non-ideal shapes. In general, due to its hardness, high refractive index, and low electrical conductivity, the fabrication of optical waveguides in single crystal diamond has proven to be challenging. Nevertheless, waveguiding structures have been

created using high refractive index materials engineered onto diamond substrates [95], resulting in a weak coupling to nitrogen vacancies (NVs) close to the surface.

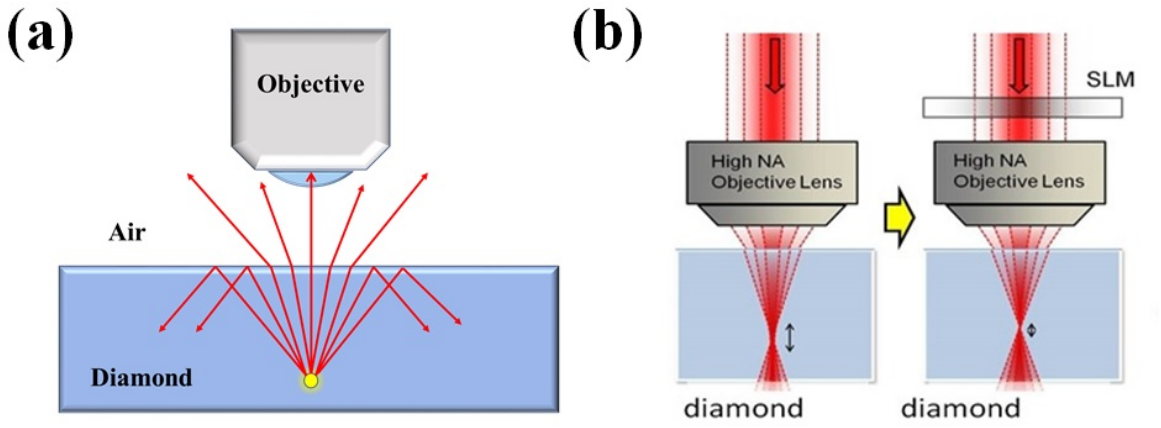

Figure 4.1. Chapter-38. Schematic showing (a) Small angle of total internal reflection, leading to reduced collection efficiency of the NV emission from the bulk of diamond. (b) The spherical aberration correction using a spatial light modulator (SLM) as the adaptive optics element

To overcome these limitations, Olivero et al. created the first optical waveguide within a single crystal diamond in 2005 [96] using the FIB technique. But the fabrication process caused unwelcome stress in the diamond films, which resulted in poor NV spectral properties [97]. Due to the scaling restrictions imposed by the FIB fabrication process, the waveguide length was also restricted to a few hundred micrometers. Recent waveguide fabrication in diamond has mainly relied on selective diamond etching to create an air-diamond interface. Typically, these etching processes are cumbersome and consist of many steps, involving ion implantation, high-temperature annealing, etching of the waveguides into the diamond using RIE, and FIB to make 45° cuts into the waveguides to act as total internal reflection mirrors. Shallow multimode waveguides have also been made using other methods, such as direct ion microbeam writing, but these only work with 2D waveguide geometries [98].

Although the methods described above have produced many diamond-based applications, they are still unable to create deep waveguides inside the bulk of diamond, where the coherence times of the color centers are significantly increased.

The aforementioned approaches are mostly applicable to two-dimensional waveguiding structures and multi-step procedures requiring extensive material processing, clean room facilities, and expensive laboratories. More importantly, a better interface for optical control of the color centers requires the waveguiding structures to be easily compatible with the optical technologies that are already in use. Unquestionably, the development of diamond-based quantum technologies requires a different fabrication strategy.

In this framework, the femtosecond laser micromachining method positions itself as a viable method for creating 3D waveguide structures in the bulk of diamond. Despite the fact that ultrafast laser processing has been used to form graphitic lines in diamond, laser writing optical waveguides is a more difficult task. Spherical aberration is an essential limitation when focusing a laser beam through a high NA objective into the bulk of diamond because of the high refractive index of diamond. Adaptive optics can be used to correct for this, as shown in Figure 4.1(b). The fabrication of optical waveguides in diamond requires the type II geometry, due to the reduced refractive index at the laser focus. Moreover, since graphite is so highly absorbent at the wavelengths of interest, its formation is detrimental for the performance of visible wavelength waveguides in diamond. Hence, it becomes crucial the choice of laser writing parameters used to fabricate ideal low loss stress-induced waveguides, avoiding the extensive creation of the graphitic phase.

4.2 Optical Waveguides in Diamond

A continuous and uniform laser-induced modification in the bulk of diamond is a crucial element for the realization of an optical waveguide in the material. This is the reason why, an initial effort was focused on determining the ideal settings for laser writing a single continuous line in diamond, carried out by Dr. Bharadwaj [100]. The main parameters to be tuned were the laser wavelength, laser repetition rate, sample scan speed, NA of the focusing objective, laser power, and input beam polarization. High NA (greater than 0.7) objective lenses were preferred because they provided greater resolution through a smaller spot size at the focus. Higher NA objectives also result in lower pulse energies for writing, which reduces self-focus as previously discussed in section 2.1.

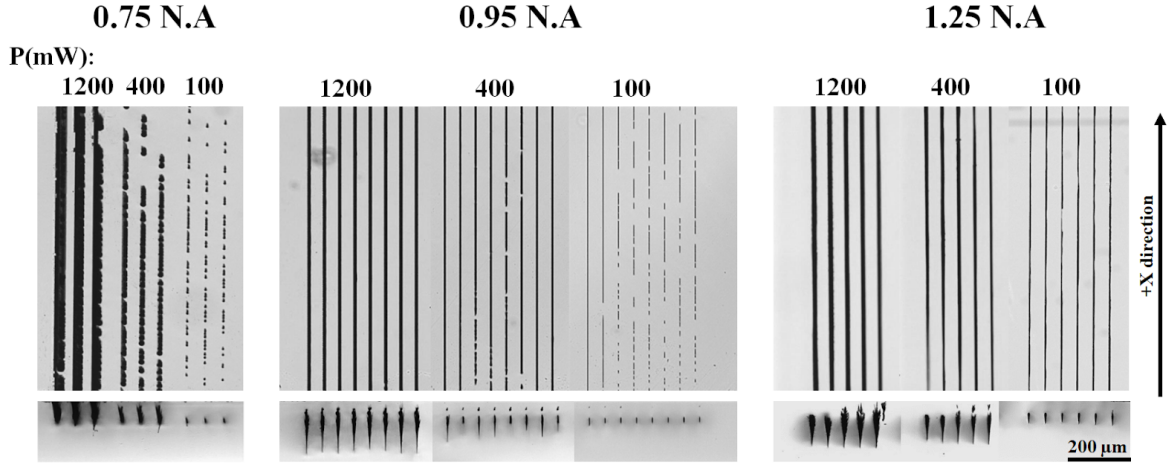

Figure 4.2. Chapter-39. Overhead and transverse optical microscope images of laser induced modifications in diamond using 0.75 NA (63×), 0.95 NA (100×) and 1.25 NA (100×) focusing objectives. The scan speeds of laser writing (from right to left) in each power sets of 0.75 NA are 0.05, 0.2 and 1 mm/s, for 0.95 NA, the scan speeds are 0.2, 0.5, 1 and 5 mm/s (written along +x and -x directions), for 1.25 NA, the scan speeds are 0.5, 2, 5, 20 and 40 mm/s

Using high NA objectives, attempts were made to laser write continuous lines, in particular 0.75 NA, 0.95 NA and 1.25 NA were used. As regards the material used, single crystal polished optical grade (OG) diamond samples were fabricated. Due to diamond's UV absorption edge being at about 220 nm, two photons of 515 nm are more

likely to get nonlinearly absorbed than two photons of 1030 nm, making modifications easier to form with 515 nm writing wavelength. As shown in Figure 4.2, higher powers (average power greater than 500 mW at 500 kHz) led to strongly elongated modifications as well as sample cracking at some scan speeds.

By identifying the variables that resulted in continuous smooth lines through straightforward optical microscope characterization it was possible to identify the most promising parameters. As illustrated in Figure 4.2, the structures written with 0.75 NA were discontinuous and non-uniform for low powers, while ablations and cracking were caused by higher powers. Although continuous modifications were produced for higher powers using the 0.95 NA objective, the resulting structures were elongated and asymmetric. As can be seen in Figure 4.2, even at low powers and for a wide range of scan speeds, a high NA of 1.25 produced continuous and smooth modifications, where it was confirmed that the continuity of the modification lines was unaffected by the laser beam's polarization with respect to the writing direction. The following parameters were found to be the most effective for causing uniform and repeatable modifications in the majority of samples: 500 kHz repetition rate, 50 mW average power, 1.25 NA objective (RMS100X-O,100, Olympus), and 0.5 mm/s scan speed.

Micro-Raman spectroscopy was used to examine the structural characteristics of the laser-induced modification in diamond. The modified Raman spectra were compared to the characteristic Raman peak of pristine diamond, which is at 1333 cm^{-1} and has an FWHM of approximately 2.3 cm^{-1} [100].

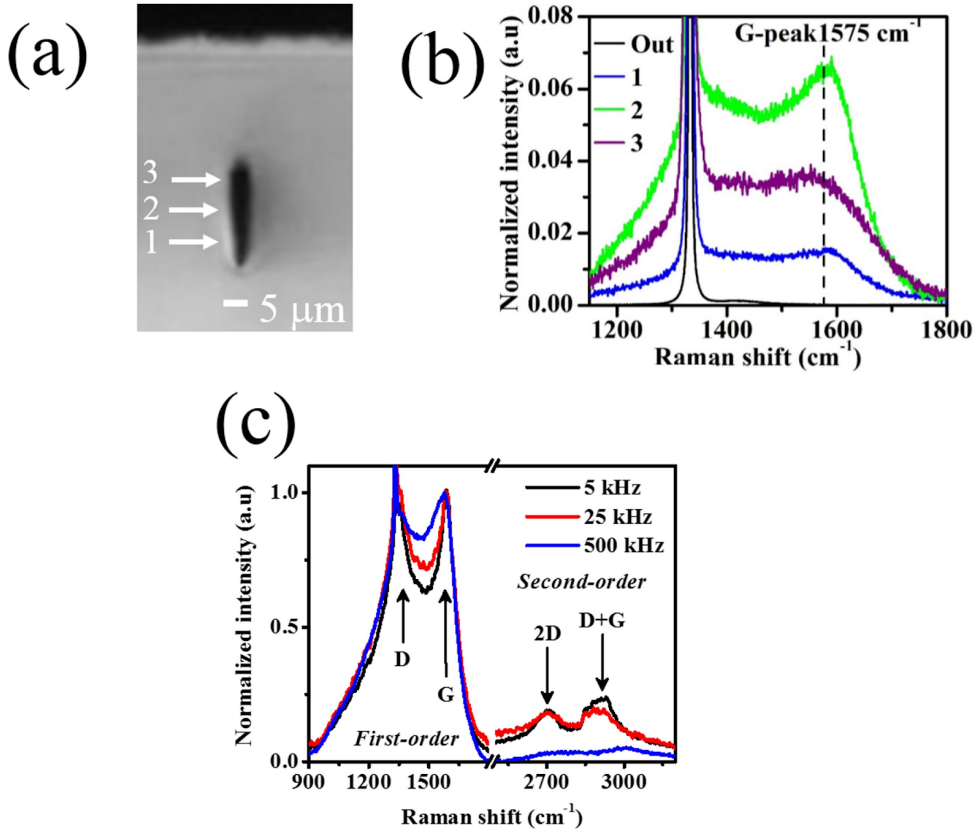

Figure 4.3. (a) Transverse optical microscope image of a single laser-induced track written with 515 nm wavelength, 500 kHz repetition rate, 50 mW average power and 0.5 mm/s scan speed. (b) Micro-Raman spectra at four different vertical positions inside the modification. 'out' refers to a spectrum taken outside the track. The spectrum has been normalized to the diamond peak to show the change in the relative intensity of the G-peak inside the structure. (c) Micro-Raman spectra (normalized to the G-peak) in the center of the modification tracks at repetition rates of 5, 25 and 500 kHz, with pulse energy being constant (800 nJ) to produce similar modification at each repetition rate.

Micro-Raman was applied to lines written with lower repetition rates of 25 kHz and 5 kHz, while maintaining constant pulse energies, in order to understand the impact of the laser's repetition rate on the material modification. Plotted in Figure 4.3(c), it is clear that as the repetition rate was lowered, the G-peak became sharper and second order peaks appeared at 2700 cm^{-1} (the 2D-peak) and 2900 cm-1 (the D+G peak), indicating increased graphitization.

Motivated by the micro-Raman results on single line modifications, two closely spaced single line modifications were engraved into a waveguide using the type II modality of waveguide writing. Using the following parameters, waveguides were written at a

depth of 50 μm from the surface: 515 nm wavelength, 500 kHz repetition rate, 50 mW average power, 1.25 NA focusing objective, and 0.5 mm/s scanning speed. The waveguides were characterized at 635 nm wavelength using the fiber coupled configuration as explained in Section 3.2. The buried waveguide in diamond was inscribed for the first time in literature with a 13 μm gap between the lines [102]. Using a 60× objective lens, the mode was imaged on the beam profiler (Spiricon) (Figure.4.4).

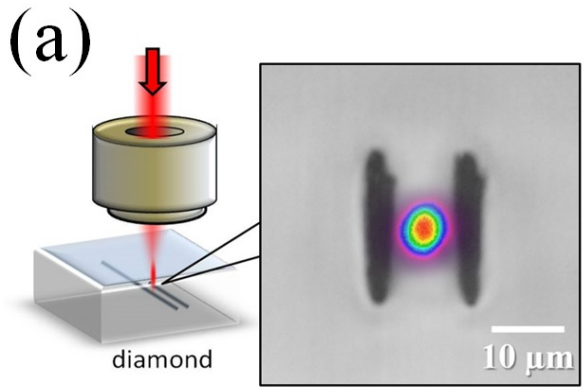

Figure 4.4. Schematic showing the type II modality of laser writing in diamond with the transverse view of the actual type II waveguide in diamond and the inset showing the mode at 635 nm.

Scanning the input fiber vertically revealed three distinct regions of guiding, with the central region exhibiting the lowest loss mode. The waveguide only showed single mode guiding in the horizontal direction. The Spiricon beam profiler's Beamgage software was used to measure the mode field diameter (MFD). When the central mode was characterized at 635 nm, the MFD was found to be 10 μm × 11 μm. The insertion loss was determined to be 11 dB for the best waveguide with a waveguide length of 5 mm, including 1.4 dB/facet coupling loss and 0.3 dB/facet Fresnel reflection loss. Similar losses were observed in the waveguides at 808 nm and 1550 nm, but with slightly larger mode field diameters.

The buried waveguides in diamond are fundamental for quantum computing and magnetometry because they enable the interaction with the diamond's color center properties. The laser written waveguides must be able to maintain the defects' internal properties in order for them to operate properly. As shown in Figure 4.5(a), the free space coupling strategy was used for investigation. 532 nm wavelength green laser (Verdi, Coherent) with a half-wave plate to control the input polarization was focused into the input facet of the waveguide (5 mm long waveguides in optical grade sample) using a 10× objective (Newport 5721-H-B) and the output mode was collected using a 60× objective (Newport 5721-H-B) and initially imaged onto the beam profiler (Spiricon) for investigating the guided mode. After using a notch filter to filter the pump wavelength, the optical mode was collected onto a spectrometer (Ocean Optics model HR2000) in order to record the photoluminescence signal from the waveguide. As seen in Figure 4.5(b), the waveguides displayed polarization-dependent behavior by only supporting the TM mode. Other crystals like Lithium Niobate [22], KDP [103], and Ti:Sapphire [104] have type II waveguides that exhibit a similar behavior and have beenalready reported and studied.

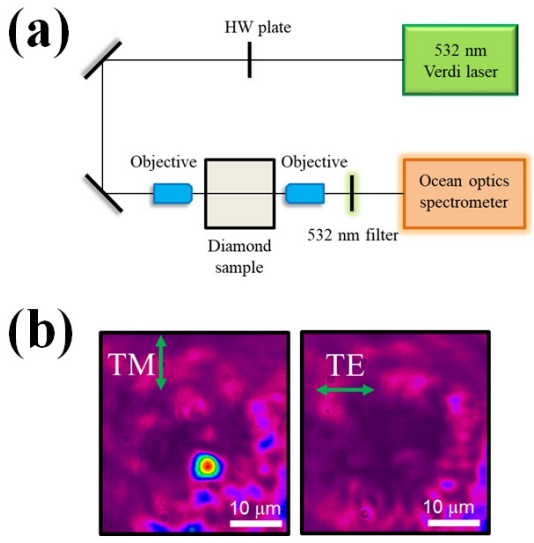

Figure 4.5. Schematic showing the free space coupling and photoluminescence measurement setup (b) The beam profile of the modes for TE and TM polarization of the input beam.

Such a polarization-dependent propagation has been attributed to the modification's elliptical shape, which caused the induced stress to cause a different refractive index for TE and TM polarizations [22]. To investigate the induced stress in femtosecond laser-written waveguides in diamond, polarized micro-Raman studies were carried out [105]. A refractive index profile map was created by relating the polarized Raman signal to the stress vectors surrounding the type II waveguide structure, as shown in Figure 4.6(a). Figure 4.6(b) and (c) depict how the mode position with respect to the two modification lines matched with the refractive index profile. At the waveguide center, it was observed that the refractive index change was about 3×10^{-3}.

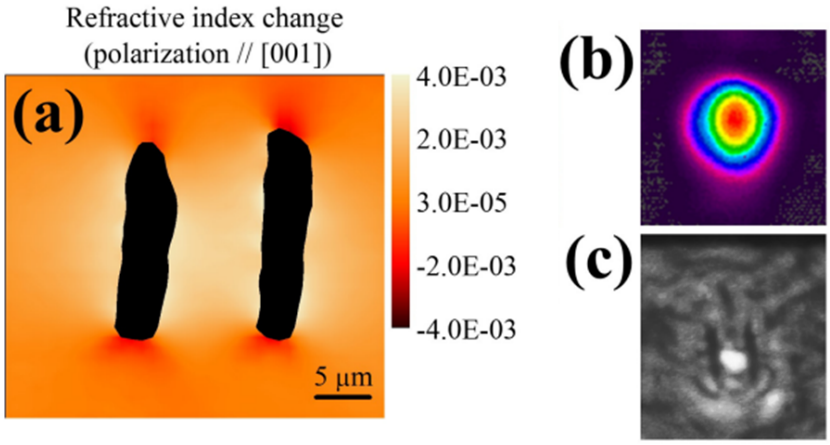

Figure 4.6. (a) Map of the refractive index profile for the type II waveguide structure. (b) Optical mode at 635 nm for the waveguide. (c) Image showing the position of the mode with respect to the two damaged lines.

Additionally, the vertical confinement of the mode is caused by the stress-induced refractive index variation, as opposed to the horizontal confinement of the mode, which is caused by the two lower refractive index modification lines.

For applications in magnetometry, shallower waveguides are advantageous for better interaction between the external magnetic field and the color centers. In this regard, a low-purity HPHT diamond sample had shallow waveguides laser-written onto it (See Section 3.3 for more details).

Single mode guiding at a wavelength of 635 nm was supported by type II waveguides

at depths shallower than 30 μm. This is explained by the less elongated modification structures in diamond caused by the decreased spherical aberration at shallow depths. About 12 μm below the surface was the lowest depth that could be reached, while increased insertion losses result from surface ablation caused by shallower focusing.

The side view microscope image of the shallow waveguides written at depths of 20, 15, and 12 μm is shown in Figure 4.7 (a) (from left to right). The waveguides were written using a laser with a writing wavelength of 515 nm, a repetition rate of 500 kHz, a pulse energy of 60 nJ, a scanning speed of 0.5 mm/s, and an objective with numerical aperture of 1.25 NA. The shallowest waveguide's characterization of the mode profile at 635 nm wavelength is displayed.

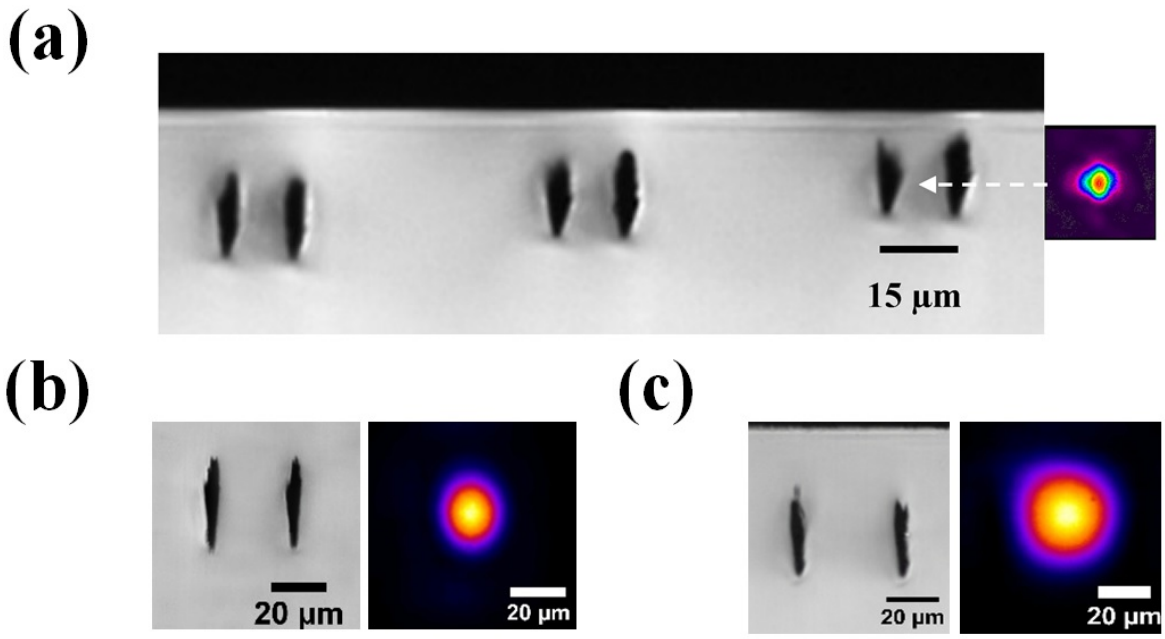

Figure 4.7. (a) Side view microscope image of shallow waveguides in diamond showing the mode at 635 nm for the shallowest waveguide. Side view microscope image showing a type II waveguide and optical mode at (b) 2.3 μm (c) 8.7 μm wavelength guiding.

Thanks to the ability to create optical waveguides using the laser writing technique, waveguides can be fabricated for mid-IR guiding and can even be extended to terahertz guiding. In order to confine longer wavelengths, type II waveguides were designed with greater separation.

The average power was varied from 75 to 100 mW. The depth was varied from 35 to 50 μm. The separation between the lines was also varied from 18 to 45 μm.

Single mode guidance for 2.3 μm wavelength was seen for waveguides with separation from 30 to 45 μm. The lowest propagation loss measured was 6 dB/cm for a waveguide with separation of 30 μm (Figure 4.7 (b)). For 8.7 μm guiding, the best waveguide was with a separation of 40 μm leading to a propagation loss of 5.9 dB/cm (Figure 4.7(c)).

4.3 Y-Splitters in Diamond

Motivation

Recently, a collaboration between our group and Kubanek's group from Ulm University [106] lead to the evidence for a single-photon non-linearity in a laser-written SiV^--waveguide system, demonstrating super-Poissonian light statistics originating from single photon subtraction between a quasi-coherent excitation field and the resonant fluorescence of the defect center.

A 300 fs pulse duration at 515 nm central wavelength and a 1.25 NA oil immersion objective were used for laser writing type-II waveguides in an electronic grade diamond slab of dimensions $2 \times 2 \times 0.3$ mm^3 and were optimized for a transmission wavelength of 738 nm, corresponding to the zero phonon line (ZPL) wavelength of the SiV^- center.

Through shallow ion implantation into the waveguides' front facet, the defect centers were produced after annealing at 1000 °C, resulting in spectrally stable emitters.

The experimental setup, illustrated in Figure 4.8(a,b), can be divided into two parts, the reflection and transmission paths. The SiV^- emission coupled into the waveguide is captured using a 0.25 NA objective in the transmission path that is aligned with one of the waveguides. Confocal access is obtained through the reflection channel (0.9 NA), allowing to scan the sample's facet using either an off-resonant 532 nm laser or an on-resonant tunable laser excitation source. All measurements were made in a flow cryostat at 5 K.

Sufficiently low laser powers are used, so that the driving field is in a quasi-coherent state with a non-negligible single- and two-photon contribution, in order to study the effect on the photon statistics. The mean photon number $\langle n \rangle_\tau$ within the given excited-state lifetime of the emitter, $\tau_{ex} = (2.5 \pm 0.6)$ ns, considering the photon

statistics of a quasi-coherent light field, can be calculated using the formula $\langle n \rangle_\tau = \frac{P_0 \eta_{tot} \tau_{ex}}{h\nu}$, where η_{tot} is the total attenuation, h is the Planck constant, and ν is the laser frequency.

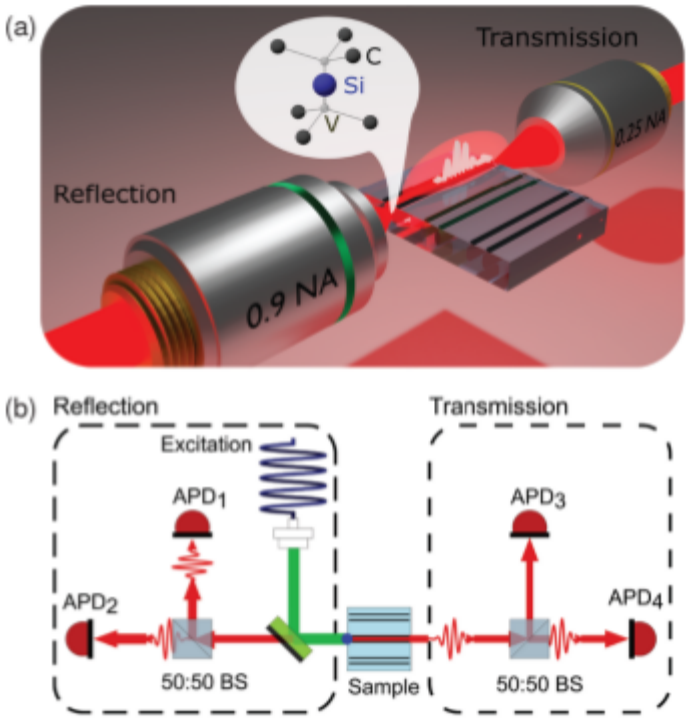

Figure 4.8. (a) Schematic depiction of single photon coupling in the diamond waveguide. Here, the guidance of the excitation laser and the photon emission of a single shallow implanted SiV − center is depicted. (b) Setup sketch, where a single SiV, indicated by the blue dot, is excited in the reflection path. Each detection path, in reflection and transmission, is equipped with two single photon detectors in HBT configuration.

This yields a mean photon number of $\langle n \rangle_\tau = 0.0022 \pm 0.0007$ for the quasi-coherent field and an eigenvalue of $a = \sqrt{\langle n \rangle_\tau} = 0.047 \pm 0.007$. Hence, the quasi-coherent state, normalized to the lifetime of the emitter, is described by:

$$|\alpha\rangle = e^{-\frac{|\alpha|^2}{2}} [\sum_{n=0}^{\infty} \frac{\alpha^n}{\sqrt{n!}} |n\rangle = 0.9989|0\rangle + 0.0472|1\rangle + 0.0016|2\rangle + ...]$$

Low photon flux of the excitation field can saturate the transition of the defect center in the case of large photon–atom interaction, and a single SiV^- center can alter the output field. A super-Poissonian light statistic of the transmitted light results from the removal

of individual photons from the quasi-coherent state. The autocorrelation measurement presented in Figure 4.9 confirms a bunching behavior at zero time delay, as expected from the HBT measurement.

Nonclassical light field engineering could build on the ability to laser-write advanced photonic components like Y-beam and X-beam splitters, allowing for on-chip Hong-Ou-Mandel interference [107] and the creation of path-entangled light fields for quantum metrology applications including super-resolution phase estimation beyond the standard quantum limit [108].

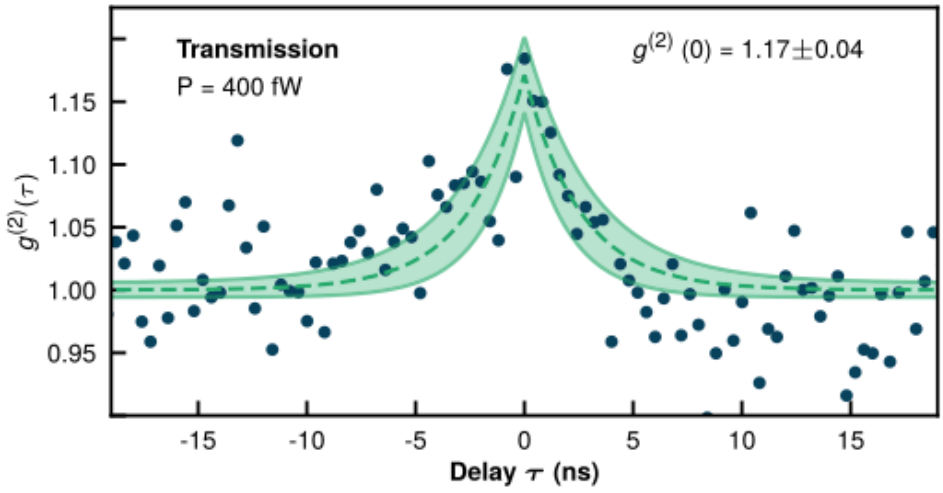

Figure 4.9. Correlation measurement at resonance with the same transition, detected in transmission (740/13 nm BP). Here, the quasi-coherent laser light is correlated with the emitters' fluorescence, which is guided through the waveguide (compared to Figure 15b). At zero time delay, bunching is clearly visible. The determined error margins, including the 2σ confidence interval, are indicated by the highlighted red and green areas, respectively.

Fabrication

For the mentioned reasons, i.e. increase the collection efficiency from defect ensembles and allow for path-entanglement or on-chip Hong-Ou-Mandel interference, we decided to engineer Y-splitters in bulk diamond exploiting the techniques used for straight waveguides.

A Y-splitter, also called bifurcation, is a special combiner used for passing from one to

two straight channels. This device cannot be simply realized as a splitting of one channel into two, since the presence of sharp angles will couple the guided modes to the radiation modes of the structure, generating losses. Therefore, we need to have a smoother division between the two structures, thus identifying three sections:

- A first section, indicated with I, is a single-mode guided section in which the field has a gaussian profile;
- The second section, indicated with II, is an adiabatic taper, in which the fundamental mode of the previous section is coupled to the two main modes (a symmetric and an antisymmetric one) of this larger section without any loss ;
- A third section, where we have the real bifurcation, where the two modes (symmetric and antisymmetric) are coupled in different waveguides, thus resulting in two waveguides with split power.

The study was aimed at finding the optimum parameters for having a balanced splitting. For the lines fabrication we used similar parameters to the ones already introduced in the previous sections: 515 nm central wavelength, 500 kHz repetition rate, 1 ps pulse duration, 1.25 NA (100× objective), 60 μm depth of the input waveguide.

The parameters that were varied were the radius of curvature of the bent regions R, from 100 to 225 mm with steps of 25 mm, the separation between output waveguides δ, from 20 to 60 μm with steps of 10 μm and the writing pulse average power P, from 30 to 50 mW with steps of 10 mW.

A total of 88 y-splitters were fabricated on a sample of optical grade diamond of dimension 2 × 2 × 0.5 mm^3. The overhead and cross-sectional optical microscope images of the sample are displayed in figures 4.10, 4.11 and 4.12, where it can also be seen how the parameters are grouped.

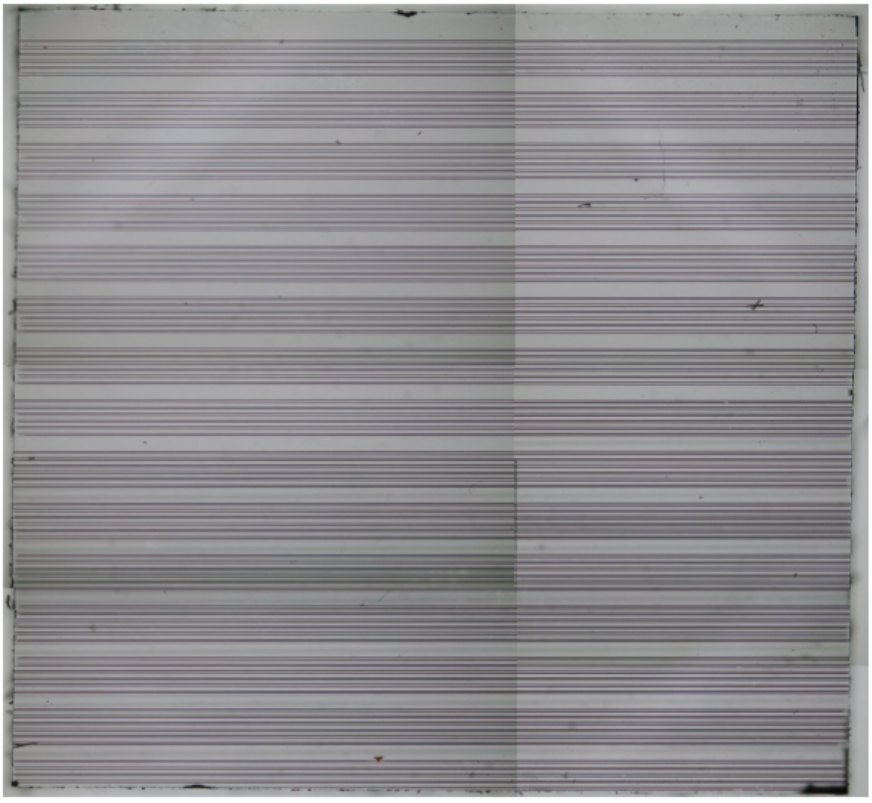

Figure 4.10. Overhead and optical microscopy images of Y-splitters in OG diamond. The sample dimensions are 2 mm × 2 mm × 0.5 mm.

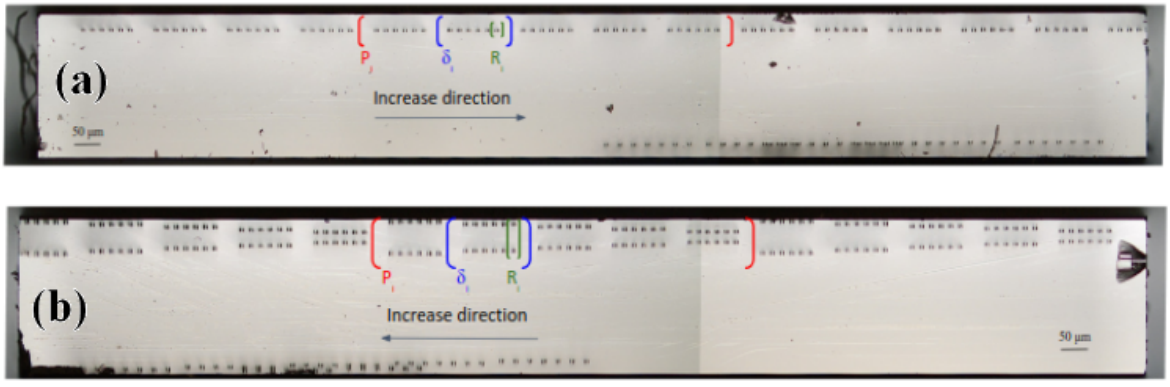

Figure 4.11. Cross sectional optical microscopy images of input (a) and output (b) ports of Y-splitters in OG diamond. Labels indicate how the writing power, separation of output ports and bending radius parameters are grouped. The arrow indicates the direction where the parameters increase.

Figure 4.12. Cross sectional side view optical microscopy images of Y-splitters in OG diamond.

Characterization

Imaging the guided modes with the Spiricon beam profiler, we observed that all the waveguides showed to have good mode shapes. We also noted that changing slightly the input coupling changed the coupling efficiency of the two output waveguides, pointing to the existence of different guiding paths within the waveguide sidewalls. Moreover, the shallow paths showed a higher attenuation with respect to the deep ones.

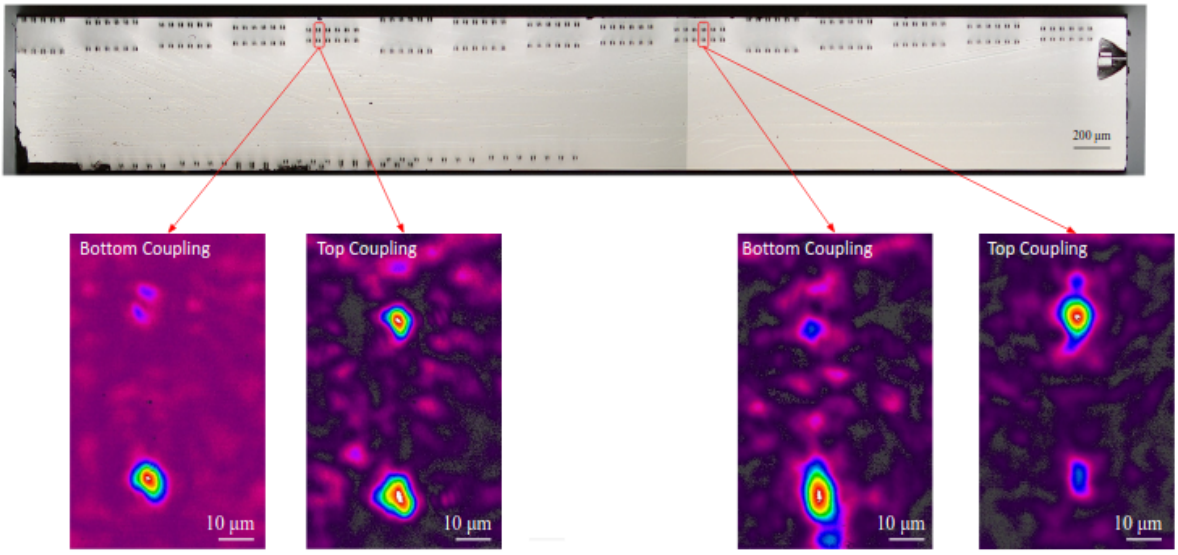

Figure 4.13. Cross sectional optical microscopy images of output ports of Y-splitters in OG diamond. In set images show the behavior of splitters 33 and 66 for different launching conditions. It can be seen that for splitter 66 there exists a condition for achieving splitting of the field onto the output ports.

We managed to find some splitters that showed a balanced coupling into output guides for certain launching conditions (fig. 4.13) and proceeded to measure the insertion losses by coupling the output to an optical power meter as shown in section 3.2.

As shown in table 4.1, we concluded that the best splitter was the number 64, having values of insertion losses for upper and lower output ports respectively of 28,8 dB and 28,5 dB, characterized by radius of curvature 175 mm, separation between output ports 20 µm and writing power of 50 mW. In conclusion, we were able to achieve a good splitting ratio but at the cost of very high losses. This is probably due to a non-ideal adiabatic tapering and to the increased propagation losses in the shallow guiding path.

To improve the device a more gentile broadening of the tapering region, a higher separation from the surface of the top output port and a smaller depth of the waveguides would be the next steps.

#Waveguide	R [mm]	δ [μm]	P [mW]	Top coupling IL_{bottom} [dB]	Top coupling IL_{top} [dB]	Bottom coupling IL_{bottom} [dB]	Bottom coupling IL_{top} [dB]
22	175	50	30	-19.9	-34.4	-22.5	-25,1
39	150	50	40	–21.8	-34.7	-27.7	-32.3
64	175	20	50	-25.4	-34.9	-28.5	-28.8
66	225	20	50	-23.5	-34.0	-32.8	-32.1
68	125	30	50	-23.1	-31.8	-35.0	-36.3
72	225	30	50	-22.3	-35.1	-34.3	-35.9
75	150	40	50	-20.2	-37.1	-36.3	-36.8

Table 4.1.

4.4 High Density NVs in DNV Diamond

NVs appear more frequently as isolated single emitters in high purity, low nitrogen content diamond, like electronic grade, which therefore is more suitable for quantum computing applications. Whereas diamond with lower purity and thus higher concentration of nitrogen, like optical grade and HPHT, is the choice of preference for quantum sensing applications. For the purposes of sensing, single NVs can be incorporated into nano diamonds or nanophotonic devices enabling their use as atomic scale probes in scanning probe microscopy or in vivo imaging of cells or other biological processes. However, as the measurement of the spin states depends on the collection of fluorescence, the measurement sensitivity using single NVs is relatively low, so that to achieve a high sensitivity the speed of the measurement must be sacrificed. Alternatively, one can work towards an increase of the devices' sensitivity, at the expense of the measurement resolution, through the use of high-density ensembles of NVs. This is related to the fact that the device sensitivity scales with the square root of the NV centers' concentration, allowing then also faster measurements.

Providing a uniform and high concentration ensemble of NV centers (4.5 ppm NV centers with T_2^* of 0.5 ms), we studied the laser writing of optical waveguides in a new commercial CVD diamond from Element 6 specifically designed for quantum sensing.

From a waveguide written in this DNV-B14 diamond, if the coherence time of NV centers is not degraded, one could expect a more than 10-fold improvement in sensitivity compared to the results in HPHT.

Waveguide Fabrication and Characterization

The fabrication and characterization of waveguides were carried out, respectively, in the Felis lab at the CNR-IFN facility at the Politecnico di Milano, Lecco campus and University of Calgary.

Optical waveguides were laser written in DNV-B14 diamond with our standard

fabrication parameters of 515-nm wavelength, 300-fs pulse duration, 500-kHz pulse duration, 1.25-NA oil immersion objective, 0.5-mm/s scan speed, and 13-mm separation between waveguide sidewalls. Figure 4.14 shows the overhead and cross-sectional optical microscope images of the sample, which features five identical sets of waveguides with four waveguides per set, written with powers of 50, 40, 30, 20 mW (left to right). The repetition of the same laser parameters for the fabrication was chosen to validate the repeatability of the results, given the inhomogeneity of previous experiments within the same HPHT diamond sample [109].

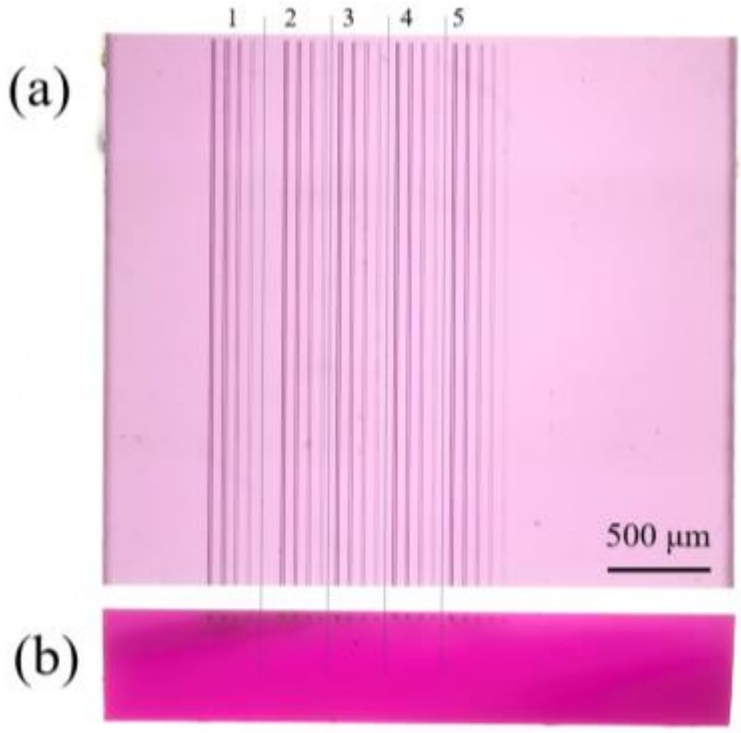

Figure 4.14. (a) Overhead and (b) cross sectional optical microscopy images of waveguides in DNV-B14 diamond from Element 6. The sample dimensions are 3 mm × 3 mm × 0.5 mm. Five identical sets of waveguides were attempted with average powers of 50, 40, 30, 20 mW at a depth of 30 mm.

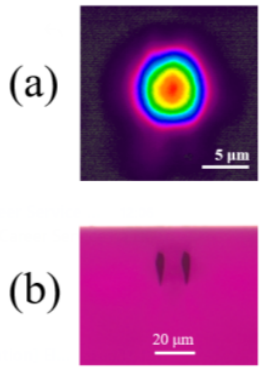

Figure 4.15. (a) Mode profile and (b) cross sectional microscope image of waveguide formed with 40-mW average power.

Confocal Photoluminescence Microscopy

The confocal microscopy analysis was performed in the labs of our collaborators at the University of Calgary to ensure that the NV properties in diamond were not compromised by the fabrication.

For confocal photoluminescence measurements, nitrogen-vacancy defects were excited with a 520-nm fiber pigtailed laser diode (LP520-SF15, Thorlabs) focused onto the sample with a 0.70-NA objective (100× Plan Apo Infinity Corrected Long WD Objective, Mitutoyo). Photoluminescence was collected through the same objective, filtered from the excitation light using a 532-nm dichroic beamsplitter (Di02-R532-25x36, Semrock) and 593-nm long-pass filter (FF01-593/LP-25, Semrock) and focused into a single mode fiber which provided the confocal aperture. Photon counting of the filtered light was performed using an avalanche photodiode (COUNT-20C-FC, Laser Components).

Confocal photoluminescence maps are shown in Figure 4.16 for the waveguide in Figure 4.15(a). Overhead (left) and cross sectional (right) views are shown, where similar count rates were observed within the pristine (indicated by region 1) and waveguide regions (region 3). In region 2, there is a dramatic reduction in signal within the laser-induced damage tracks which define the waveguide sidewalls.

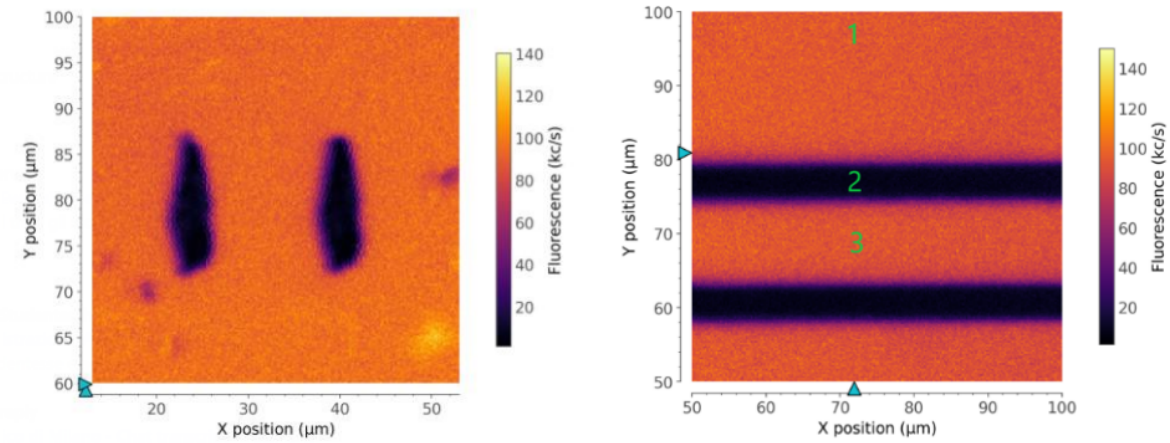

Figure 4.16. Confocal fluorescence microscopy scan with overhead (right) and cross sectional (left) views showing type II waveguide, with similar photon count rates in the pristine and waveguide regions. The waveguide depth (center of modification to surface) is approximately 30 mm. The air interface is just off screen at a Y position of 50 mm.

.

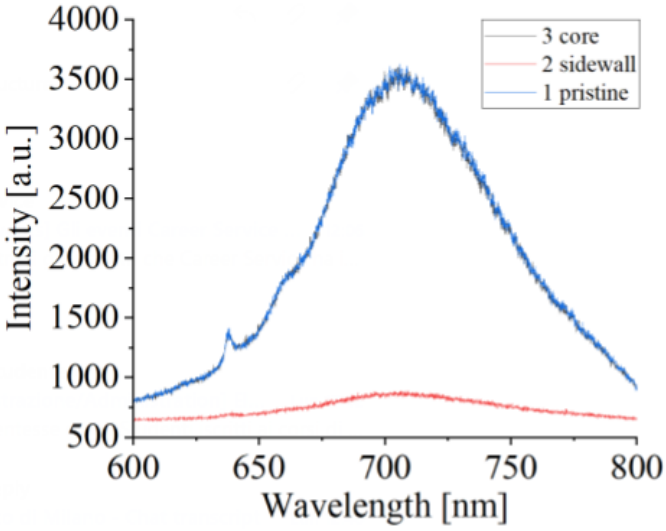

Figure 4.17. Photoluminescence spectra within (1) pristine, (2) sidewall and (3) waveguide regions in diamond when excited with 532-nm light.

Coherence Properties Characterization

Based on the above optical result, the waveguide formed with 40-mW average power in Set 4 was further characterized by the group from Cardiff University.

From Fig. 4.18, there is no significant difference of zero field CWODMR between pristine and waveguide area in diamond. The central frequency D in pristine and

waveguide regions are 2870.29, and 2869.98 MHz, respectively, which are very close to 2870 MHz. The zero-field splitting parameter E is less than 3.1 MHz which is smaller than that (4 MHz) in normal HTHP diamond samples. But a 0.23 MHz lager E was found on the waveguide region, indicating more local strain within the waveguide. Finally, both ODMR contrasts are over 8%, showing uniform MW field coupling efficiency.

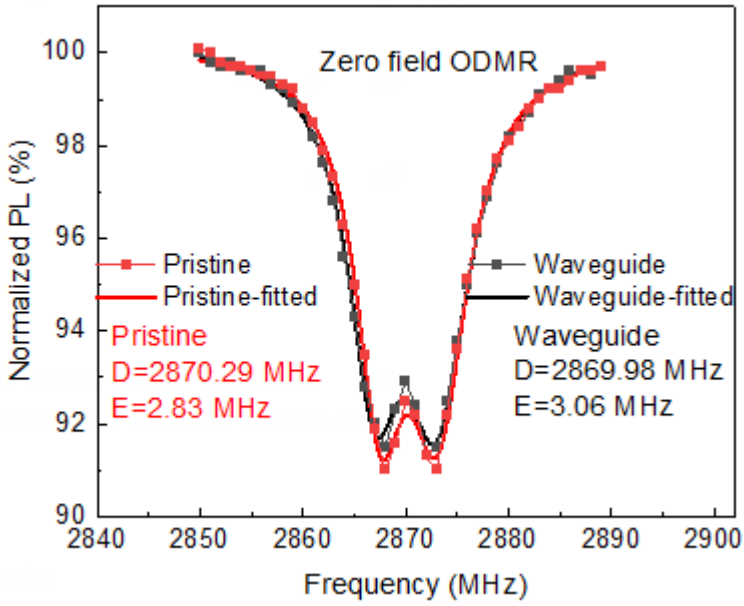

Figure 4.18. Zero field ODMR spectra within pristine and waveguide regions in diamond.

To evaluate the static field inhomogeneities, T_2^* of NVs in waveguide and pristine diamond have been demonstrated by Ramsey fringes in Fig. 4.19. Both waveguide and pristine areas have the comparable ODMR contrast (~ 1%) and dephasing coherence time (~ 500 ns). The experimental data is fitted by:

$$e^{\left(\frac{t}{T_2^*}\right)^n} \cdot \left(\sum_i A_i \sin\left(w_i t + b_i\right) + c\right)$$

where the t is the free evolution time, T_2^* is the dephasing coherence time, A_i is the amplitude, w_i is the precession frequency, b_i is the phase determined by MW detuning

and Rabi frequency, *n* is the exponential coefficient which depends on the domain dephasing source. Considering it as a nearly Gaussian decay, the *n* is set as 1.9. The slight difference in dephasing time is probably due to the magnetic gradient and transverse magnetic field. Thanks to excellent coherence property and PL rate, this waveguide device could be a very sensitive static field sensor.

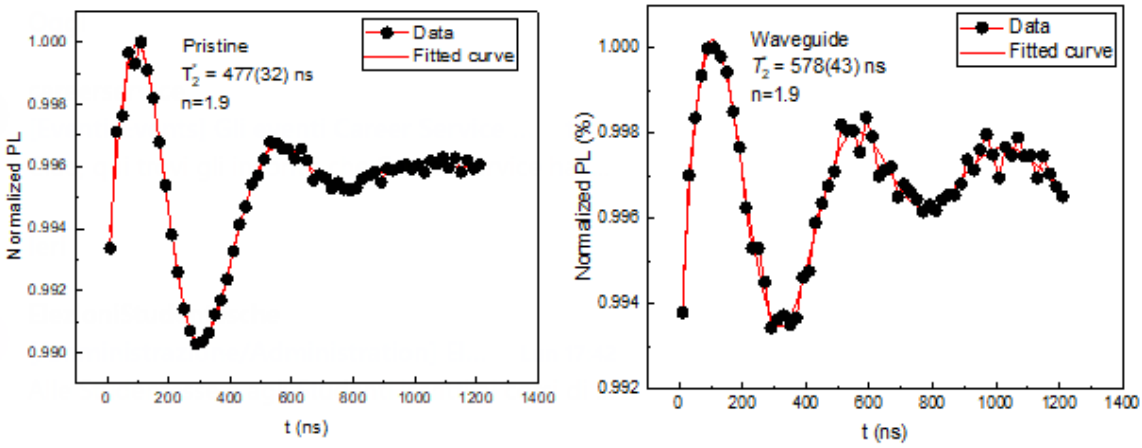

Figure 4.19. ODMR spectra with bias magnetic field in pristine and waveguide regions in diamond.

The photon shot-noise limited CW magnetic field sensitivity is given by equation:

$$\eta \sim \frac{\hbar}{g\mu_B}\frac{1}{\sqrt{M\Gamma}}\frac{1}{T_2^*}$$

By taking the PL rate of 3.2×10^{12} Hz, contrast of 4%, T_2^* of 500 ns, the photon shot noise sensitivity is estimated at ~ 257 pT·Hz$^{-1/2}$. This constitutes a great achievement, since previous results obtained by similar fabrications in HPHT diamond suggested a magnetic field sensitivity of 1.5 nT·Hz$^{-1/2}$, a value already above the state-of-the-art sensitivities for magnetic sensors of ~ 0.29 nT·Hz$^{-1/2}$ [109].

Chapter 5

Deterministic Placing of Color Centers

5.1 Motivation

Ion beam implantation, in which high energy ions are bombarded onto the surface of the material, is the traditional technique for deterministically placing color centers. However, this method has several drawbacks. To begin with, the method is incapable of creating defects in the bulk at depths deeper than 5 μm with high accuracy while maintaining the color centers' high quality properties. For greater depths, higher energy atoms would be required, causing residual damage to the crystal lattice, resulting in undesirable strain and local unwanted defects, which reduces the spectral properties of the color centers [110, 111]. The technique also necessitates extensive sample preparation and high-budget labs equipped with particle accelerators for high-energy ion accelerations for the formation of deep defect centers [110].

Color centers in glasses [112, 113] and crystals [114] have been successfully created using femtosecond laser pulses. In fact, it has been demonstrated that color center formation contributes to the increased refractive index change during bulk femtosecond

laser writing in glasses. Since femtosecond laser micro-fabrication is a highly nonlinear process, it allows for the creation of color centers within small focal volumes with submicrometer resolution for high NA focusing objectives.

The preliminary motivation was obtained by the photoluminescence measurements performed within the damage lines in diamond formed by laser writing which showed the presence of amorphous carbon along with substantial quantities of vacancies and vacancy complex defects [102]. This implied the possibility of laser-induced vacancy creation by focusing femtosecond laser pulses with energies lower than the amorphization threshold. The heat treatment would drive the mobilization of vacancy defects to increase the probability of encountering impurities.

5.2 Laser Writing of NV Centers in Diamond

Previous work from Dr. Bharadwaj showed the ability to deterministically fabricate NV centers in bulk diamond using femtosecond laser pulses.

To laser inscribe NV ensembles to boost the sensitivity in quantum sensing, static laser exposures in lower purity optical grade CVD diamond, with a nitrogen content of about 100 ppb, were performed. Initial efforts were focused towards determining the pulse energy threshold for amorphization. 515 nm wavelength femtosecond laser pulses with varying pulse energies and pulse numbers were focused using an 1.25 NA objective at a depth of 25 μm within the diamond bulk. The sample was then annealed at a high temperature of 1000 $^{\circ}$C for 3 hours in a nitrogen atmosphere to avoid oxidation of the diamond surface in a tubular horizontal furnace (LTF15/50/450, Lenton). Above 600° C, the vacancies become mobile and can be captured by the substitutional nitrogen impurities to form the NV centers [115]. The higher temperature of 1000° C has been shown to improve the spectral properties of the NV centers formed [110, 116, 117].

The initial trials were performed with a wide range of pulse energies from 2 nJ to 100 nJ and pulse numbers from single pulse until 5000 pulses. The dots were separated by a spacing of 20 µm, offering a convenient spatial separation for subsequent characterization. Preliminary overhead microscope imaging of the static exposures revealed a formation of visible dark modification for higher energies and higher pulse numbers, as can be seen in Figure 5.1(a). Confocal photoluminescence studies using 532 nm excitation wavelength were performed on the static exposed positions to better understand the laser pulse induced material modification in diamond. There were three main trends observed corresponding to the photoluminescence spectra obtained. For the static exposures creating visible marks i.e., high energy and high pulse number, as shown in 5.1(b), the photoluminescence shows the presence of a G-peak even after annealing. The zero phonon line (ZPL) of NV^- is not recovered after annealing. This indicates amorphization in the regions with visible dots. The static exposures produced invisible modifications for low energies and low pulse numbers.

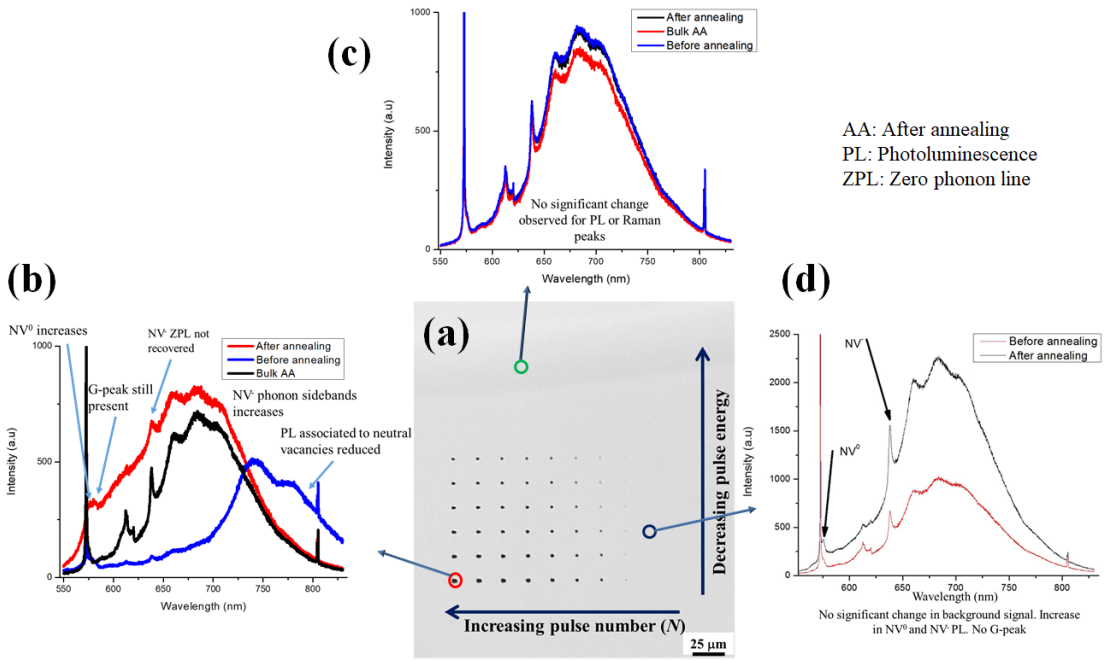

Figure 5.1. (a) Overhead microscope image of laser induced modification for pulse energies of 2, 6, 10, 20, 30, 40, 50, 60, 80 and 100 nJ with pulse numbers (N) of 1, 5, 25, 50, 100, 500, 1000, 2000 and 5000 at a depth of 25 µm. A typical confocal PL measured from (b) an exposure creating visible modification, (c) invisible static exposure with low pulse energy (d) invisible static exposure with low pulse numbers and moderate energies.

The photoluminescence measurement performed for low energy (< 10 nJ) static exposures shows no significant improvement in the ZPL intensity of NV^- or the Raman peak before and after the annealing as shown in Figure 5.1(c). This implies the absence or the inability to create any useful modification using the corresponding writing parameters.

The photoluminescence from the exposures with lower pulse numbers (N < 10) and pulse energies lower than 40 nJ, shows no significant change in the background photoluminescence but the ZPL of NV^- is greatly enhanced without any presence of G-peak as shown in Figure 5.2(d). This indicates the presence of NV centers with good spectral properties and allows us to narrow down the parameter range for further optimization.

Inspired by the preliminary results from the optical grade diamond sample, further static exposures with refined writing parameters with pulse energies from 10 to 30 nJ and number of pulses N of 5 and 1 were performed on ultrapure electronic grade diamond sample with the aim to create single NVs for quantum computing applications. Since, the formation of the NV center greatly depends on the presence of a substitutional nitrogen atom in the vicinity, there is a certain probability of NV formation after annealing at varying locations in the sample. In order to determine this probability, 10 trials of the same parameters were performed at 10 different locations for statistical analysis. Marker points were laser-written with static exposures using 25 pulses of high energy of about 100 nJ to locate the spatial position of the invisible NV centers created. The sample, following the static exposures was annealed at 1000° C for 3 h. Visible modifications were observed for the set with number of pulses N = 5 as shown in Figure 5.2(a), which implies amorphization rather than NV center formation. For N = 1, the modifications were invisible.

Confocal photoluminescence was performed at the static exposed sites for the set with single pulse (N = 1) irradiation, revealing the enhancement of the NV^- ZPL as shown in Figure 5.2(b) for certain pulse energies. The pristine diamond shows no

photoluminescence at the wavelength range of interest. As the pulse energy increases, until about 14 nJ of pulse energy, there is no significant NV^- ZPL intensity observed. As the pulse energy increases further, the intensity of the ZPL increases and at about 18 nJ, the peak intensity saturates and begins to drop with further increase in the pulse energy and at about 28 nJ the disappearance of ZPL is observed. This saturation can be attributed to the pulse energy reaching closer to the amorphization threshold energy leading to a degradation in the NV spectral properties [116].

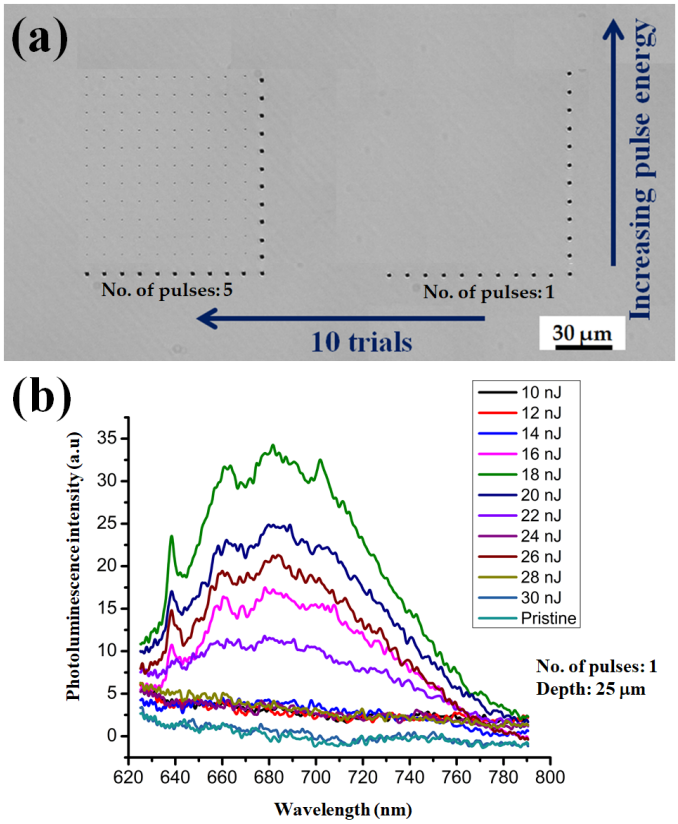

Figure 5.2. (a) Overhead microscope image of laser induced modification for pulse energies of 10, 12, 14, 16, 18, 20, 22, 24, 26, 28 and 30 nJ with pulse numbers (N) of 1 and 5 at a depth of 25 µm. The visible dots are marker dots written with a pulse energy of 100 nJ and (N) = 25 pulses. (b) Confocal photoluminescence measurement showing the ZPL of NV − from the static exposures written with single laser pulse and various pulse energies.

Another important parameter of interest is the success rate of formation of NVs.

It was seen that for a pulse energy of 24 nJ, 8 out of the 10 trials produced NV centers giving a NV center creation probability of 80% but when averaged over 5 different samples, the probability was about 50%, comparable with the yield reported by Chen et al. [116].

Further spectral characterization of the NV photoluminescence was performed at the University of Calgary in order to better understand the spatial confinement and the statistical behavior of the photon emission from the laser written NVs in electronic grade diamond.

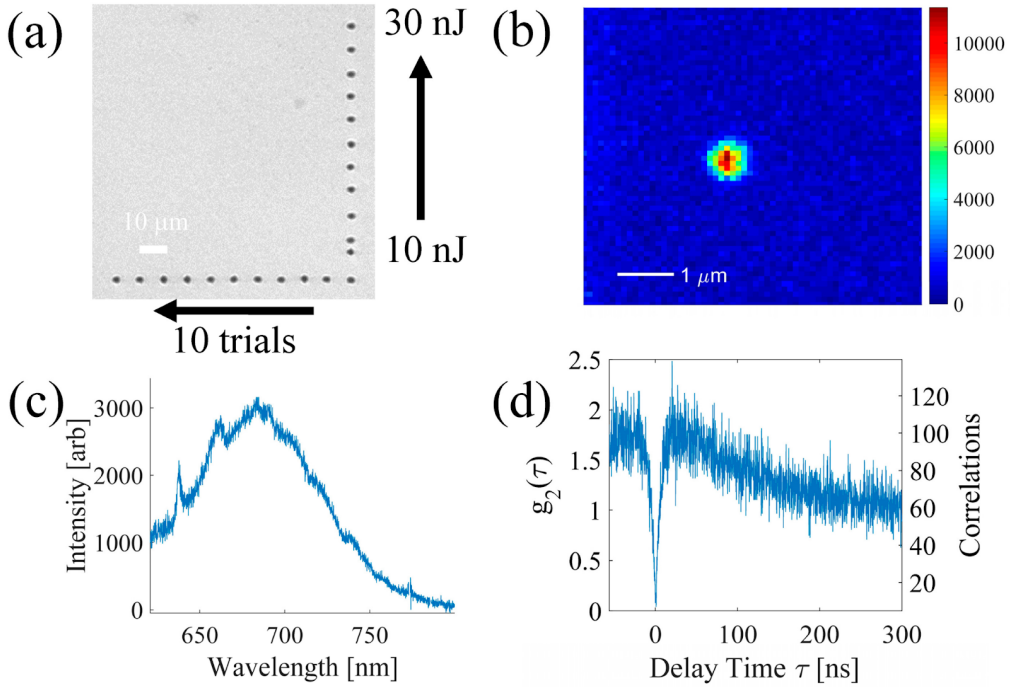

Figure 5.3. (a) Overhead microscope image of laser induced modification for pulse energies of 10, 12, 14, 16, 18, 20, 22, 24, 26, 28 and 30 nJ with pulse number of 1 at a depth of 25 µm. The visible dots are marker dots written with a pulse energy of 100 nJ and (N) = 25 pulses. (b) Overhead photoluminescence map of static exposure with a pulse energy of 24 nJ. (c) Photoluminescence measurement of the 24 nJ static exposure NV. (d) Intensity autocorrelation (corrected for background on left y-axis, raw uncorrected correlations counts on the right y-axis) revealing single photon emission.

The static exposure with a pulse energy of 24 nJ was considered for further analysis. The photoluminescence map measured from the static exposure showed an emission with a spatial confinement of about 1 µm^2 within the static exposure as shown in Figure 5.3(b). The photoluminescence measured from the static exposure revealing the NV$^-$ ZPL measured at room temperature is shown in Figure 5.3(c). Second-order intensity correlation measurements were also performed to probe the statistical nature of the photon emission from the laser written NV centers. A typical photon antibunching setup used to obtain the second order intensity correlation function is shown in Figure

5.4. The second order intensity correlation function at zero delay time is given by the following equation:

$$g^{(2)}(0) = \frac{\langle n(n-1)\rangle}{\langle n\rangle^2}$$

where, n is the number of photons emitted by the source. It can be seen that at a delay time of 0, if a single photon is emitted, then the second order intensity correlation function $g^{(2)}(0)$ is 0. If two photons are emitted, then $g^{(2)}(0)$ is 0.5, suggesting that if a value of anything less than 0.5 is obtained, then the source can be regarded as a single photon source. The antibunching $g^{(2)}(0)$ dip for the laser written NV centers was obtained to be well below 0.5 as can be seen from Figure 5.3(d), implying single photon emission from the NV created in the bulk of diamond using single femtosecond laser pulse irradiation followed by annealing [118].

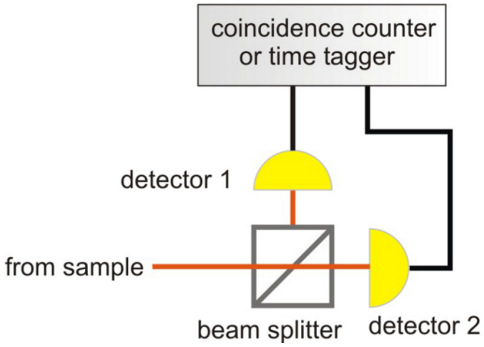

Figure 5.4. A typical photon antibunching setup for determining the second order intensity correlation function.

5.3 Laser Writing of Vacancy Centers in SiC

Silicon carbide (SiC) is a wide-bandgap semiconductor characterized by high breakdown voltage, high thermal conductivity, and it is commercially available in high-quality wafers. Aside from applications in electronics, SiC has attracted increasing attention as a suitable material for quantum technologies as it can host several optically active point defects that emit light in the spectral region from visible to near-infrared and can overcome many of the drawbacks of diamond such as compatibility with microelectronics technology, nanostructuring and n- and p-type doping.

Motivated by the results obtained in diamond, i.e. the possibility to create laser-induced vacancies with focused femtosecond laser pulses, we decided to deterministically fabricate color centers in SiC, namely the silicon vacancy center (V_{Si}) and the divacancy centers ($V_{Si}V_C$). For this project we started a collaboration with the group of Prof. Castelletto from RMIT University towards this common goal. Their results from previous research [119,120] have been the starting point of the experiment presented in this section.

From PL confocal maps generated using a 730 nm excitation and a confocal objective with NA of 0.85 (fig 5.5), they observed that laser pulse energies below 13 nJ did not provide any PL suggesting that the damage was not enough to produce vacancies and localization was not achieved. The confocal map of an individual spot written at 330 nJ/pulse had a full width half maximum (FWHM) in the lateral (XY) direction of 1.22 ± 0.03 and 1.25 ± 0.03 μm, while at 13 nJ, the spot had a FWHM of 498 ± 2 nm, comparable with the confocal lateral diffraction limit of $0.61\lambda/(2NA)$= 494.8 nm.

Using room temperature and 80 K spectroscopy, they determined the origin of the PL as shown in Figure 5.6. The broad emission of the fabricated areas at 920 nm is attributed to the V_{Si} [121, 122] (Figure 5.6(a)). In addition, for fabrication at shallower depths, they observed also a room temperature broad emission at 770 nm, which is

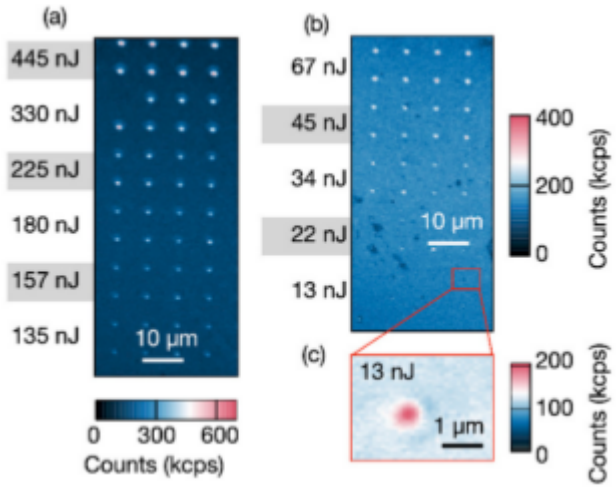

Figure 5.5. Confocal maps of high-purity semi-insulating (HPSI) 4H-silicon carbide (SiC) containing arrays of color centers laser written with a 515 nm fs-laser at single energies ranging from (a) 135-445 nJ to (b) 13–67 nJ.

attributed to surface damage. At 80 K (Figure 5.7(b)), they observed from the fabricated area a clear emission from the V1' at 859 nm corresponding to the optical transition between the ground state and the second excited state of the V_{Si} center.

In summary, it was demonstrated that this technique is valid and can lead to a facile and more deterministic on demand generation of key color centers in SiC for single photon sources and distributed quantum networks.

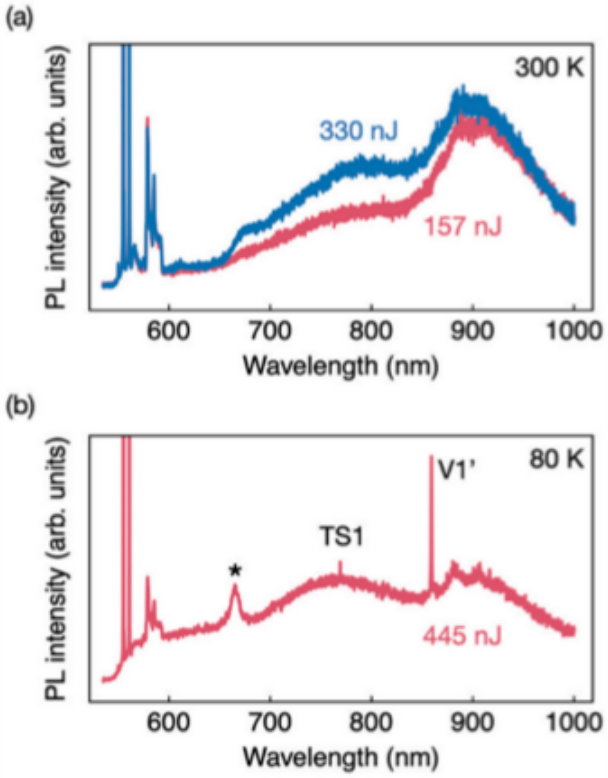

Figure 5.6 Spectroscopy of the (a) HPSI 4H-SiC laser written area corresponding to the highest energy dots of 445 and 330 nJ showing a broad emission centered at 920 nm and an emission at 770 nm. (b) Here, 80 K spectroscopy of a dot at 445 nJ. V1' is at 859 nm corresponding to the hexagonal ZPL of the VSi in the 4H-SiC. The emission at 769 nm shows a ZPL at low temperature, TS1, previously observed in proton irradiated 4H-SiC annealed at high temperature, however, the origin is unknown. A peak indicated with (*) is also an unknown emission and it is due to laser irradiation.

We received samples of 4H-SiC from RMIT University consisting in two n-type (10^{15} cm^{-3}) doped samples and in particular the a-grown SiC, in which the creation of NV centers was never demonstrated and should be characterized by an enhanced PL spectrum. Moreover two intrinsic High Purity Semi-Insulating samples from CREE commercial were delivered and a thin layer sample, which could be a good candidate to study the emitters in the red.

The initial experiment was on a sample of High Purity Semi-Insulating 4H-SiC. We used a central wavelength of the pulses of 515 nm and a focusing objective with NA of 1.25 and 100x magnification. For statistical analysis, 6 trials of the same parameters were performed. The parameters being varied were: the average pulse energy, from 10 to 230 nJ ; the number of pulses per exposure, from 1 to 500; the focusing depth, from 7 to 25 μm. The geometry of the fabrication layout is shown in fig 5.7.

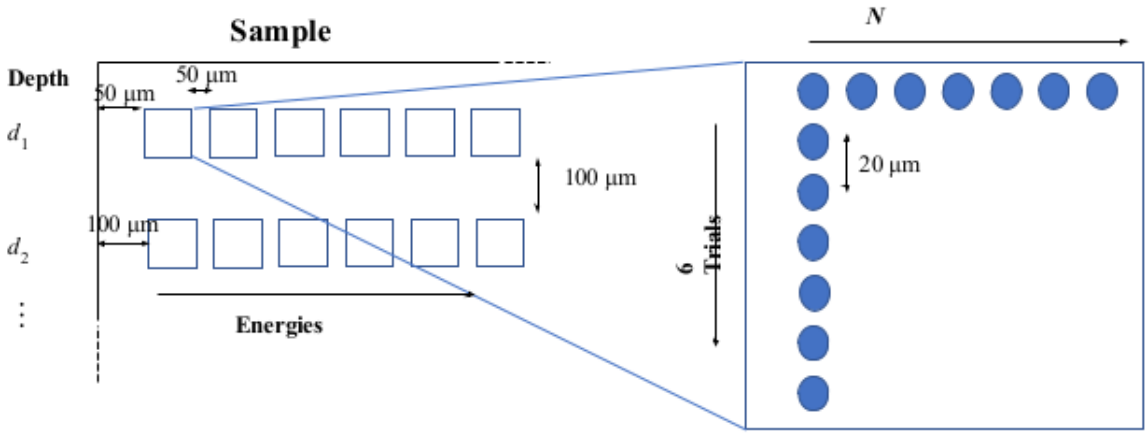

Figure 5.7. Fabrication layout. Writing regions with different pulse energy are separated by 50 µm. Writing regions with different depth are separated by 100 µm. Irradiation spots inside every writing region are separated by 20 µm.

Unfortunately, our femtosecond source turned out to have problems and we didn't manage to create the color centers. The equipment was delivered to MenloSystems for maintenance where it was found that one of the diodes was broken and the internal pulse compressor misaligned, resulting inpulse durations longer than 1 ps, instead of the expected 300 fs. For the time constraints of the thesis work it was impossible to repeat the experiments.

In conclusion, even though the flaws in the femtosecond laser source prevented our experiment from yielding results, the technique's potential to create active color centers in SiC is undeniably promising. The next phase of research will focus on developing a method to create atomic defects like $V_{Si}N_C$ centers, which emit light at the telecom wavelength, in addition to vacancy centers like V_{Si} and $V_{Si}V_C$ as treated in the presented work.

5.4 Laser Writing of color centers in hBN

Hexagonal boron nitride (hBN) is a laminar van der Waals material, and thus very interesting for the purpose of researching semiconductor physics in two dimensions [123]. (2D). In particular, a large number of defect states with internal optical transitions corresponding to color centers may be present in the wide bandgap of hBN. As previously demonstrated in the bulk semiconductors such as diamond and silicon carbide, some of these centers have already shown great promise in the application of quantum technology [124,125]. But because of the unique characteristics of quasi 2D semiconducting flakes, color centers in exfoliated hBN may show significant improvements over their bulk counterparts. Many color centers in hBN [124,125] have been identified as new generation high temperature single photon emitters in recent years. It is generally acknowledged that these color centers can be connected to point defects and point defect complexes, even though the microscopic arrangement and electronic structure of these emitters are still not fully understood.

With the goal of creating single photon emitters in hBN using the technique of femtosecond laser micromachining, we started a collaboration with CIC nanoGune research center and Ulm University which lead to the results presented in this section.

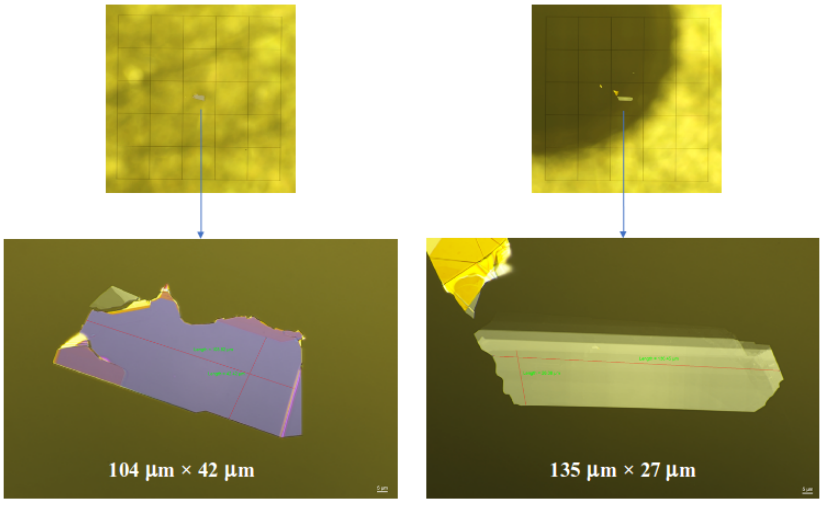

Figure 5.8. Overhead microscope images of bottom right and top left grids on sample 1 and zoomed view of the flakes deposited onto it.

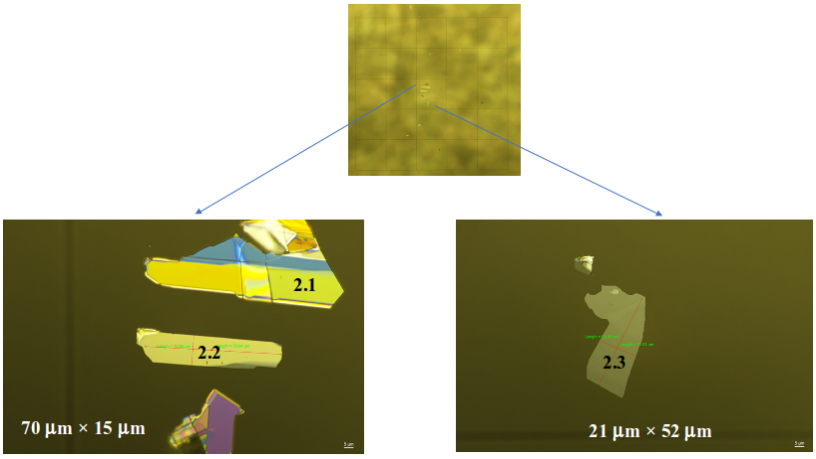

Figure 5.9. Overhead microscope images of sample 2 and zoomed view of the three flakes deposited onto it.

The samples consisted in 1-10 layers of hBN flakes deposited on fused silica (10 × 10 × 1 mm^3) obtained by exfoliation and were provided by CIC nanoGUNE research center. For each sample, 4 grids were laser written in order to easily locate the hBN flakes deposited onto it. Each grid consisted in 5×5 square sections of 300 μm^2.

Considering the two most interesting samples, the deposition onto the silica substrate resulted in two grids containing a hBN flake on sample 1 and one grid on sample 2 containing multiple flakes. In figures 5.8-9 images of the flakes located onto the grids and details on the flakes are shown.

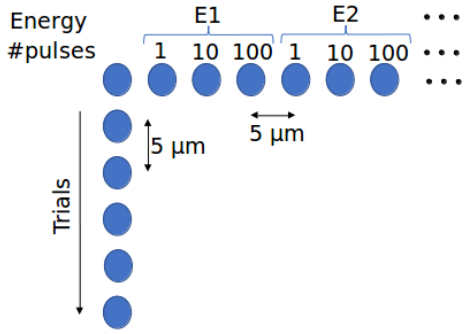

Figure 5.10. Fabrication geometry for static exposures.

Fabrications were carried out at Felis laboratory in Lecco. The laser writing parameters were: 515 nm wavelength, 250 kHz repetition rate, 100× objective (without oil), NA of 0.9. For sample 1 the particular fabrication geometry is depicted in figure 5.8. For the flake in the top left grid the writing energies were: 4, 10, 15, 25, 40 nJ, while for the flake in the bottom right grid the writing energies were: 30, 35, 40, 50, 60 ,70 , 80 nJ and the maximum number of pulses was 50. For sample 2 only single pulse exposures were done. After the fabrication, images and spectra were acquired through confocal microscopy to inspect for the presence of color centers at Ulm University. One of the flakes of sample 1 showed very interesting results, as can be seen in fig. 5.11. Plenty of possible emitters all over the examined spectral region (580-800 nm) were observed, even though the correlation between irradiated spots and emitters location was not clearly defined and many of them were unstable and blinking.

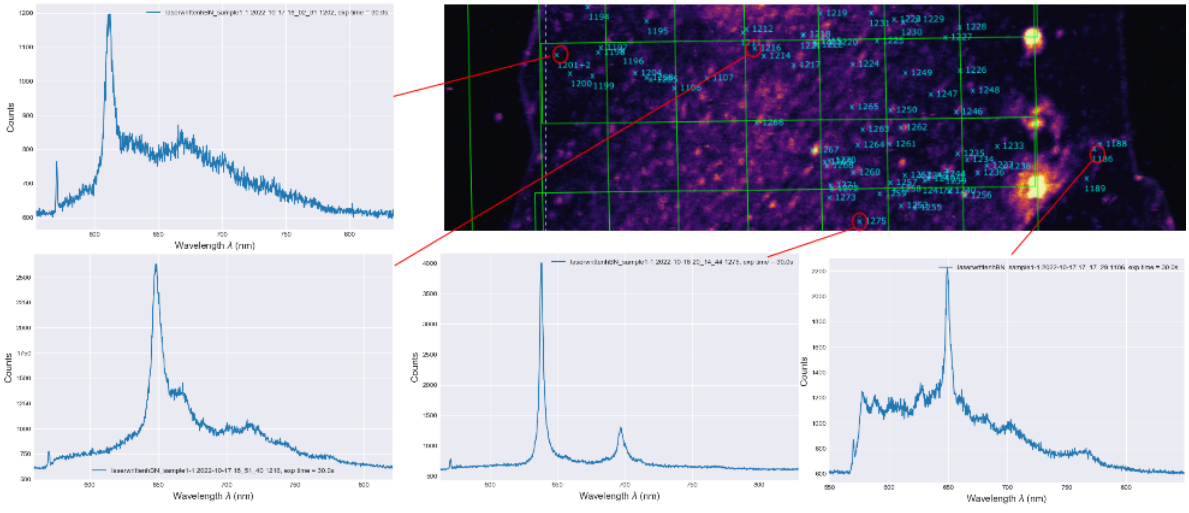

Figure 5.11. Confocal microscopy image of one flake of sample 1 after irradiation and emission spectra of possible emitters.

For what concerns sample 2, after an annealing treatment at 800°C, the samples were inspected with confocal microscopy (fig 5.12) and spectra were acquired, however the data didn't point to presence of deterministically placed emitters through laser irradiation, probably because the oven used in Ulm for annealing didn't reach high

enough temperature resulting in the bleaching of the possible created emitters, or generally didn't manage to activate them.

In conclusion, we didn’t manage to produce strong evidence of fabrication of color centers in hBN through femtosecond laser pulses were produced, but more research is needed. Next steps could be the study of the type of emitters and their concentration as a function of laser writing parameters; measuring the second order correlation $g^{(2)}$ in order to check for the actual presence of single photon emitters and experiment on other types of hBN samples, such as CVD grown ones, to investigate the influence of the type of material used on the results.

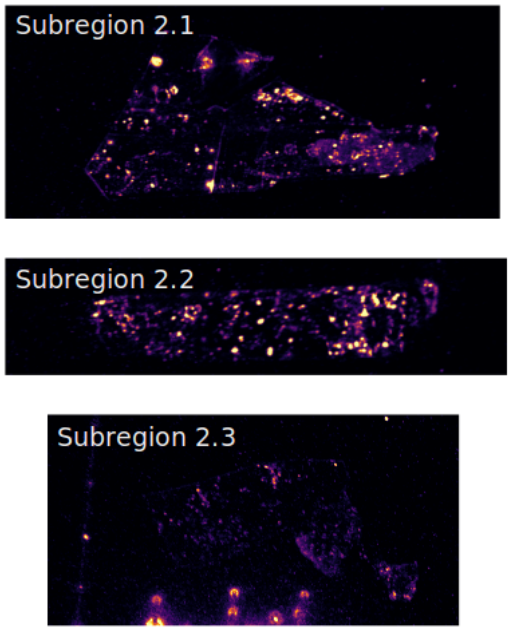

Figure 5.12. Confocal microscopy image of flakes on sample 2 after irradiation.

Chapter 6

Conclusion

The key goal of this thesis work was to develop integrated quantum photonic devices based on optically interconnected color centers for applications in quantum information and sensing through femtosecond laser micromachining.

The waveguides in the bulk of relevant materials play a major role in the optical excitation and collection of the photoluminescence from color centers. The optical mode size and the physical dimensions allow easy compatibility with existing fiber optic technology for optical excitation and collection, opening the way to lab-on-a-chip quantum devices. In this work photonic components were engineered, in particular Y-Splitters in optical grade diamond and waveguides in NV doped diamond.

The Y-Splitters were developed with the purpose of increasing the collection of emission from ensembles of defect centers and thus improve the sensitivity of quantum sensors, but also to potentially enable complex functions as on-chip Hong-Ou-Mandel interference and path-entaglement. The optimization of the splitting ratio was the priority and the presented results were satisfactory, however the losses of the fabricated devices were substantially high. The next steps will be to find the parameters that improve the losses of the device, in particular the depth of the whole device with respect to the surface of the sample and the geometry of the tapering regions.

Waveguides in DNV diamond were developed with the idea to create an easy-to-fabricate quantum sensor, having an high concentration of NV centers in core region provided by the material platform itself. Type II waveguides were written using

femtosecond pulses irradiation and were characterized to inspect the performance. It was found that the guiding region had a similar photoluminescence count rate to the pristine region, pointing to the fact that the NV centers within the waveguide were not damaged. After characterizing the sample with Optically Detected Magnetic Resonance (ODMR) , it was possible to estimate the magnetic field sensitivity of the device which resulted in a value of some order of magnitude better with respect to previous results.

Deterministic placement of color centers using focused femtosecond laser pulses is a very important capability that has been shown possible. Deep emitters placement has always been a challenge using ion-beam implantation techniques due to the various drawbacks mentioned in chapter 5. In addition, the process requires high budget labs and intensive material processing. On the other hand, femtosecond laser writing is a very simple and scalable technique of color center placement. The technique does not require any intensive sample treatment.

Using the same femtosecond laser workstation for the writing of optical waveguides, NV centers in diamond have been previously created and attempts to create vacancy centers in SiC and to discover useful spin defects in hBN have been carried out.

SiC was taken in consideration due to its impressive properties ranging from high breakdown voltage, second order optical nonlinearity, compatibility with CMOS fabrication and, of course, the possibility to host active color centers. The experiments didn’t yield results because of faults in the laser source.

The work carried out on hBN had the intention to discover new single photon emitters in a material that has a lot to offer and it’s still relatively unknown. The sample consisted in exfoliated flakes onto a fused silica substrate. After irradiation hints for newly found emitters were suggested, but after annealing it was not possible to infer a correlation between irradiated spots and emitters location. Next steps will be constituted by a wider range of parameters of irradiation to be investigated and also

different types of samples, such as CVD grown ones.

In summary, femtosecond laser fabrication was proposed as an effective and potentially scalable method of fabrication of integrated quantum photonic devices, and even if there is great room for improvement, this work constitutes an effective proof-of-concept.

Bibliography

[1] BC Stuart, MD Feit, AM Rubenchik, BW Shore, and MD Perry. Laser-induced damage in dielectrics with nanosecond to subpicosecond pulses. Physical review letters, 74(12):2248, 1995.

[2] Chris B Schaffer, Andre Brodeur, and Eric Mazur. Laser-induced breakdown and damage in bulk transparent materials induced by tightly focused femtosecond laser pulses. Measurement Science and Technology, 12(11):1784, 2001.

[3] LV Keldysh et al. Ionization in the field of a strong electromagnetic wave. Sov. Phys. JETP, 20(5):1307–1314, 1965.

[4] Roberto Osellame, Giulio Cerullo, and Roberta Ramponi. Femtosecond laser micromachining: photonic and microfluidic devices in transparent materials, volume 123. Springer Science & Business Media, 2012.

[5] EN Glezer, M Milosavljevic, L Huang, RJ Finlay, T-H Her, J Paul Callan, and Eric Mazur. Three-dimensional optical storage inside transparent materials. Optics Letters, 21(24):2023–2025, 1996.

[6] Chris B Schaffer, José F García, and Eric Mazur. Bulk heating of transparent materials using a high-repetition-rate femtosecond laser. Applied Physics A, 76(3):351–354, 2003.

[7] Shane M Eaton, Haibin Zhang, Peter R Herman, Fumiyo Yoshino, Lawrence Shah, James Bovatsek, and Alan Y Arai. Heat accumulation effects in femtosecond laser-written waveguides with variable repetition rate. Optics Express, 13(12):4708–4716, 2005.

[8] James W Chan, Thomas Huser, S Risbud, and DM Krol. Structural changes in fused silica after exposure to focused femtosecond laser pulses. Optics letters, 26(21):1726–1728, 2001.

[9] T Toney Fernandez, P Haro-González, B Sotillo, M Hernandez, Daniel Jaque, P Fernandez, Concepción Domingo, Jan Siegel, and J Solis. Ion migration assisted inscription of high refractive index contrast waveguides by femtosecond laser pulses in phosphate glass. Optics letters, 38(24):5248–5251, 2013.

[10] Masahiro Shimizu, Masaaki Sakakura, Shingo Kanehira, Masayuki Nishi, Yasuhiko Shimotsuma, Kazuyuki Hirao, and Kiyotaka Miura. Formation mechanism of element distribution in glass under femtosecond laser irradiation. Optics letters, 36(11):2161–2163, 2011.

[11] TT Fernandez, M Sakakura, SM Eaton, B Sotillo, J Siegel, J Solis, Y Shimotsuma, and K Miura. Bespoke photonic devices using ultrafast laser driven ion migration in glasses. Progress in Materials Science, 2017.

[12] G Della Valle, R Osellame, and P Laporta. Micromachining of photonic devices by femtosecond laser pulses. Journal of Optics A: Pure and Applied Optics, 11(1):013001, 2008.

[13] Rafael R Gattass and Eric Mazur. Femtosecond laser micromachining in transparent materials. Nature photonics, 2(4):219–225, 2008.

[14] Yasuhiko Shimotsuma, Peter G Kazansky, Jiarong Qiu, and Kazuoki Hirao. Self-organized nanogratings in glass irradiated by ultrashort light pulses. Physical review letters, 91(24):247405, 2003.

[15] C Hnatovsky, RS Taylor, PP Rajeev, E Simova, VR Bhardwaj, DM Rayner, and PB Corkum. Pulse duration dependence of femtosecond-laser-fabricated nanogratings in fused silica. Applied Physics Letters, 87(1):014104, 2005.

[16] C Hnatovsky, RS Taylor, E Simova, PP Rajeev, DM Rayner, VR Bhardwaj, and PB Corkum. Fabrication of microchannels in glass using focused femtosecond laser radiation and selective chemical etching. Applied Physics A: Materials Science & Processing, 84(1):47–61, 2006.

[17] Yves Bellouard, Ali Said, Mark Dugan, and Philippe Bado. Fabrication of high-aspect ratio, micro-fluidic channels and tunnels using femtosecond laser pulses and chemical etching. Optics express, 12(10):2120–2129, 2004.

[18] Valeria Maselli, Roberto Osellame, Giulio Cerullo, Roberta Ramponi, Paolo Laporta, Luca Magagnin, and Pietro Luigi Cavallotti. Fabrication of long microchannels with circular cross section using astigmatically shaped femtosecond laser pulses and chemical etching. Applied physics letters, 88(19):191107, 2006.

[19] Roberto Osellame, Mirko Lobino, Nicola Chiodo, Marco Marangoni, Giulio Cerullo, Roberta Ramponi, Henry T Bookey, Robert R Thomson, Nicholas D Psaila, and Ajoy K Kar. Femtosecond laser writing of waveguides in periodically poled lithium niobate preserving the nonlinear coefficient. Applied physics letters, 90(24):241107, 2007.

[20] Li Gui, Baoxi Xu, and Tow Chong Chong. Microstructure in lithium niobate by use of focused femtosecond laser pulses. IEEE Photonics Technology Letters, 16(5):1337–1339, 2004.

[21] JR Macdonald, RR Thomson, SJ Beecher, ND Psaila, HT Bookey, and AK Kar. Ultrafast laser inscription of near-infrared waveguides in polycrystalline znse. Optics letters, 35(23):4036–4038, 2010.

[22] J Burghoff, S Nolte, and A Tünnermann. Origins of waveguiding in femtosecond laser-structured linbo3. Applied Physics A, 89(1):127–132, 2007.

[23] Airan Rodenas and Ajoy K Kar. High-contrast step-index waveguides in borate nonlinear laser crystals by 3d laser writing. Optics express, 19(18):17820–17833, 2011.

[24] D Du, X Liu, G Korn, J Squier, and G Mourou. Laser-induced breakdown by impact ionization in sio2 with pulse widths from 7 ns to 150 fs. Applied physics letters, 64(23):3071–3073, 1994.

[25] Feng Chen and JR Aldana. Optical waveguides in crystalline dielectric materials produced by femtosecond-laser micromachining. Laser & Photonics Reviews, 8(2):251–275, 2014.

[26] T Gorelik, M Will, S Nolte, A Tuennermann, and U Glatzel. Transmission electron microscopy studies of femtosecond laser induced modifications in quartz. Applied Physics A: Materials Science & Processing, 76(3):309–311, 2003.

[27] Vasilis Apostolopoulos, Laetitia Laversenne, Tristan Colomb, Christian Depeursinge, RP Salathé, Markus Pollnau, Roberto Osellame, Giulio Cerullo, and Paolo Laporta. Femtosecond-irradiation-induced refractive-index changes and channel waveguiding in bulk ti 3+: sapphire. Applied Physics Letters, 85(7):1122–1124, 2004.

[28] Amir H Nejadmalayeri, Peter R Herman, Jonas Burghoff, Matthias Will, Stefan Nolte, and Andreas Tünnermann. Inscription of optical waveguides in crystalline silicon by mid-infrared femtosecond laser pulses. Optics letters, 30(9):964–966, 2005.

[29] SM Eaton, CA Merchant, R Iyer, AJ Zilkie, AS Helmy, JS Aitchison, PR Herman, D Kraemer, RJD Miller, C Hnatovsky, et al. Raman gain from waveguides inscribed in k gd (wo 4) 2 by high repetition rate femtosecond laser. Applied Physics Letters, 92(8):081105, 2008.

[30] Thomas Calmano, Martin Ams, Peter Dekker, Michael J Withford, and Christian Kränkel. 2 w single-longitudinal-mode yb: Yag distributed-feedback waveguide laser. Optics Letters, 42(14):2734–2737, 2017.

[31] K Miura Davis, Kiyotaka Miura, Naoki Sugimoto, and Kazuyuki Hirao. Writing waveguides in glass with a femtosecond laser. Optics letters, 21(21):1729–1731, 1996.

[32] Fredrik Laurell, Thomas Calmano, Sebastian Müller, Peter Zeil, Carlota Canalias, and Günter Huber. Laser-written waveguides in ktp for broadband type ii second harmonic generation. Optics express, 20(20):22308–22313, 2012.

[33] Richard D Simmonds, Patrick S Salter, Alexander Jesacher, and Martin J Booth. Three dimensional laser microfabrication in diamond using a dual adaptive optics system. Optics express, 19(24):24122–24128, 2011.

[34] PS Salter, M Baum, I Alexeev, M Schmidt, and MJ Booth. Exploring the depth range for three-dimensional laser machining with aberration correction. Optics express, 22(15):17644–17656, 2014.

[35] Shane M Eaton, Carmela De Marco, Rebeca Martinez-Vazquez, Roberta Ramponi, Stefano Turri, Giulio Cerullo, and Roberto Osellame. Femtosecond laser microstructuring for polymeric lab-on-chips. Journal of biophotonics, 5(8-9):687–702, 2012.

[36] Maria Farsari and Boris N Chichkov. Materials processing: Two-photon fabrication. Nature photonics, 3(8):450–452, 2009.

[37] Robert R Thomson, Ajoy K Kar, and Jeremy Allington-Smith. Ultrafast laser inscription: an enabling technology for astrophotonics. Optics express, 17(3):1963–1969, 2009.

[38] A Arriola, S Gross, M Ams, T Gretzinger, D Le Coq, RP Wang, H Ebendorff-Heidepriem, J Sanghera, S Bayya, LB Shaw, et al. Mid-infrared astrophotonics: study of ultrafast laser induced index change in compatible materials. Optical Materials Express, 7(3):698–711, 2017.

[39] Thomas Meany, Markus Gräfe, René Heilmann, Armando Perez-Leija, Simon Gross, Michael J Steel, Michael J Withford, and Alexander Szameit. Laser written circuits for quantum photonics. Laser & Photonics Reviews, 9(4):363–384, 2015.

[40] Shane M Eaton, Wei-Jen Chen, Haibin Zhang, Rajiv Iyer, Jianzhao Li, Mi Li Ng, Stephen Ho, J Stewart Aitchison, and Peter R Herman. Spectral loss characterization of femtosecond laser written waveguides in glass with application to demultiplexing of 1300 and 1550 nm wavelengths. Journal of Lightwave Technology, 27(9):1079–1085, 2009.

[41] G Douglass, F Dreisow, S Gross, S Nolte, and MJ Withford. Towards femtosecond laser written arrayed waveguide gratings. Optics express, 23(16):21392–21402, 2015.

[42] Haibin Zhang, Stephen Ho, Shane M Eaton, Jianzhao Li, and Peter R Herman. Three- dimensional optical sensing network written in fused silica glass with femtosecond laser. Optics express, 16(18):14015–14023, 2008.

[43] Koji Sugioka and Ya Cheng. Femtosecond laser processing for optofluidic fabrication. Lab on a Chip, 12(19):3576–3589, 2012.

[44] Moez Haque, Kenneth KC Lee, Stephen Ho, Luís A Fernandes, and Peter R Herman. Chemical-assisted femtosecond laser writing of lab-in-fibers. Lab on a Chip, 14(19):3817–3829, 2014.

[45] Steger, M. et al. Quantum information storage for over 180 s using donor spins in a 28 Si “semiconductor vacuum”. Science 336, 1280–1283 (2012).

[46] Gordon, J. P. & Bowers, K. D. Microwave spin echoes rom donor electrons in silicon. Phys. Rev. Lett. 1, 368–370 (1958).

[47] Maiman, T. H. Stimulated optical radiation in ruby. Nature 187, 493–494 (1960).

[48] Abraham, M., Weeks, R. A., Clark, G. W. & Finch, C. B. Electron spin resonance of rare-earth ions in thorium oxide: Yb 3+ and Er 3+ . Phys. Rev. 137, A138–A142 (1965).

[49] Kane, B. E. A silicon-based nuclear spin quantum computer. Nature 393, 133–137 (1998).

[50] Ichimura, K. A simple frequency-domain quantum computer with ions in a crystal coupled to a cavity mode. Opt. Commun. 196, 119–125 (2001).

[51] Gruber, A. et al. Scanning confocal optical microscopy and magnetic resonance on single defect centers. Science 276, 2012–2014 (1997).

[52] Barry, J. F. et al. Sensitivity optimization for NV-diamond magnetometry. Rev. Mod. Phys. 92, 15004 (2020).

[53] Jaskula, J. C. et al. Improved quantum sensing with a single solid-state spin via spin-to-charge conversion. Phys. Rev. Appl. 11, 064003 (2019).

[54] Bradley, C. E. et al. A ten-qubit solid-state spin register with quantum memory up to one minute. Phys. Rev. X 9, 031045 (2019).

[55] Morello, A. et al. Single-shot readout of an electron spin in silicon. Nature 467, 687–691 (2010)

[56] Hensen, B. et al. Loophole-free Bell inequality violation using electron spins separated by 1.3 kilometres. Nature 526, 682–686 (2015).

[57] Wolfowicz, G. et al. Coherent storage of microwave excitations in rare-earth nuclear spins. Phys. Rev. Lett. 114, 170503 (2015).

[58] Tyryshkin, A. M., Lyon, S. A., Astashkin, A. V. & Raitsimring, A. M. Electron spin relaxation times of phosphorus donors in silicon. Phys. Rev. B 68, 193207 (2003).

[59] Orbach, R. Spin-lattice relaxation in rare-earth salts. Proc. R. Soc. Lond. A Math. Phys. Sci. 264, 458–484 (1961).

[60] Green, B. L. et al. Neutral silicon-vacancy center in diamond: spin polarization and lifetimes. Phys. Rev. Lett. 119, 096402 (2017).

[61] Jarmola, A., Acosta, V. M., Jensen, K., Chemerisov, S. & Budker, D. Temperature- and magnetic-field-dependent longitudinal spin relaxation in nitrogen-vacancy ensembles in diamond. Phys. Rev. Lett. 108, 197601 (2012).

[62] Tetienne, J.-P. et al. Spin relaxometry of single nitrogen-vacancy defects in diamond nanocrystals for magnetic noise sensing. Phys. Rev. B 87, 235436 (2013).

[63] Tyryshkin, A. M. et al. Electron spin coherence exceeding seconds in high-purity silicon. Nat. Mater. 11, 143–147 (2011).

[64] Ye, M., Seo, H. & Galli, G. Spin coherence in two-dimensional materials. NPJ Comput. Mater. 5, 44 (2019).

[65] Heremans, F. J., Yale, C. G. & Awschalom, D. D. Control of spin defects in wide-bandgap semiconductors for quantum technologies. Proc. IEEE 104, 2009–2023 (2016).

[66] Whiteley, S. J. et al. Spin–phonon interactions in silicon carbide addressed by Gaussian acoustics. Nat. Phys. 15, 490–495 (2019).

[67] Laucht, A. et al. Electrically controlling single-spin qubits in a continuous microwave field. Sci. Adv. 1, e1500022 (2015).

[68] Dreher, L. et al. Electroelastic hyperfine tuning of phosphorus donors in silicon. Phys. Rev. Lett. 106, 037601 (2011).

[69] Leibfried, D., Blatt, R., Monroe, C. & Wineland, D. Quantum dynamics of single trapped ions. Rev. Mod. Phys. 75, 281–324 (2003).

[70] Bersin, E. et al. Individual control and readout of qubits in a sub-diffraction volume. NPJ

Quantum Inf. 5, 39 (2019).

[71] Awschalom, D. D., Hanson, R., Wrachtrup, J. & Zhou, B. B. Quantum technologies with optically interfaced solid-state spins. Nat. Photonics 12, 516–527 (2018).

[72] Waldherr, G. et al. Quantum error correction in a solid-state hybrid spin register. Nature 506, 204–207 (2014).

[73] Zaiser, S. et al. Enhancing quantum sensing sensitivity by a quantum memory. Nat. Commun. 7, 12279 (2016).

[74] Taminiau, T. H., Cramer, J., Van Der Sar, T., Dobrovitski, V. V. & Hanson, R. Universal control and error correction in multi-qubit spin registers in diamond. Nat. Nanotechnol. 9, 171–176 (2014).

[75] Zhao, N. et al. Sensing single remote nuclear spins. Nat. Nanotechnol. 7, 657–662 (2012).

[76] Radko, I. P. et al. Determining the internal quantum efficiency of shallow-implanted nitrogen-vacancy defects in bulk diamond. Opt. Express 24, 27715 (2016).

[77] Müller, T. et al. Optical signatures of silicon-vacancy spins in diamond. Nat. Commun. 5, 3328 (2014).

[78] Doherty, M. W. et al. The nitrogen-vacancy colour centre in diamond. Phys. Rep. 528, 1–45 (2013).

[79] Christle, D. J. et al. Isolated spin qubits in SiC with a high-fidelity infrared spin-to-photon interface. Phys. Rev. X 7, 021046 (2017).

[80] Kindem, J. M. et al. Control and single-shot readout of an ion embedded in a nanophotonic cavity. Nature 580, 201–204 (2020).

[81] Toyli, D. M. et al. Measurement and control of single nitrogen-vacancy center spins above 600 K. Phys. Rev. X 2, 031001 (2012).

[82] Bradac, C., Gao, W., Forneris, J., Trusheim, M. E. & Aharonovich, I. Quantum nanophotonics with group IV defects in diamond. Nat. Commun. 10, 5625 (2019).

[83] Humphreys, P. C. et al. Deterministic delivery of remote entanglement on a quantum network. Nature 558, 268–273 (2018).

[84] Bassett, L. C., Heremans, F. J., Yale, C. G., Buckley, B. B. & Awschalom, D. D. Electrical tuning of single nitrogen-vacancy center optical transitions enhanced by photoinduced fields. Phys. Rev. Lett. 107, 266403 (2011).

[85] Wolfowicz, G., Whiteley, S. J. & Awschalom, D. D. Electrometry by optical charge conversion of deep defects in 4H-SiC. Proc. Natl Acad. Sci. USA 115, 7879–7883 (2018).

[86] Han, K. Y., Kim, S. K., Eggeling, C. & Hell, S. W. Metastable dark states enable ground state depletion microscopy of nitrogen vacancy centers in diamond with diffraction-unlimited resolution. Nano Lett. 10, 3199–3203 (2010).

[87] Fávaro de Oliveira, F. et al. Tailoring spin defects in diamond by lattice charging. Nat. Commun. 8, 15409 (2017).

[88] Yutaka Ando, Yoshiki Nishibayashi, Koji Kobashi, Takashi Hirao, and Kenjiro Oura. Smooth and high-rate reactive ion etching of diamond. Diamond and Related Materials, 11(3):824 –827, 2002.

[89] Birgit J.M. Hausmann, Mughees Khan, Yinan Zhang, Tom M. Babinec, Katie Martinick, Murray McCutcheon, Phil R. Hemmer, and Marko Lončar. Fabrication of diamond nanowires for quantum information processing applications. Diamond and Related Materials, 19(5):621 – 629, 2010. Proceedings of Diamond 2009, The 20th European Conference on Diamond, Diamond-Like Materials, Carbon Nanotubes and Nitrides, Part 1.

[90] Elke Neu, Patrick Appel, Marc Ganzhorn, Javier Miguel-Sánchez, Margarita Lesik, Vianney Mille, Vincent Jacques, Alexandre Tallaire, Jocelyn Achard, and Patrick Maletinsky. Photonic nano-structures on (111)-oriented diamond. Applied Physics Letters, 104(15):153108, 2014.

[91] B. J. Shields, Q. P. Unterreithmeier, N. P. de Leon, H. Park, and M. D. Lukin. Efficient readout of a single spin state in diamond via spin-to-charge conversion. Phys. Rev. Lett., 114:136402, Mar 2015.

[92] S. Ali Momenzadeh, Rainer J. Stöhr, Felipe Favaro de Oliveira, Andreas Brunner, Andrej Denisenko, Sen Yang, Friedemann Reinhard, and Jörg Wrachtrup. Nanoengineered diamond waveguide as a robust bright platform for nanomagnetometry using shallow nitrogen vacancy centers. Nano Letters, 15(1):165–169, 2015. PMID: 25438091.

[93] J. P. Hadden, J. P. Harrison, A. C. Stanley-Clarke, L. Marseglia, Y.-L. D. Ho, B. R. Patton, J. L. O'Brien, and J. G. Rarity. Strongly enhanced photon collection from diamond defect centers under microfabricated integrated solid immersion lenses. Applied Physics Letters, 97(24):241901, 2010.

[94] Paul E Barclay, Kai-Mei C Fu, Charles Santori, Andrei Faraon, and Raymond G Beausoleil. Hybrid nanocavity resonant enhancement of color center emission in diamond. Physical Review X, 1(1):011007, 2011.

[95] Paolo Olivero, Sergey Rubanov, Patrick Reichart, Brant C Gibson, Shane T Huntington, James Rabeau, Andrew D Greentree, Joseph Salzman, David Moore, David N Jamieson, et al. Ion-beam-assisted lift-off technique for three-dimensional micromachining of freestanding single-crystal diamond. Advanced Materials, 17(20):2427–2430, 2005.

[96] Andrei Faraon, Charles Santori, Zhihong Huang, Victor M Acosta, and Raymond G Beausoleil. Coupling of nitrogen-vacancy centers to photonic crystal cavities in monocrystalline diamond. Physical review letters, 109(3):033604, 2012.

[97] S Lagomarsino, P Olivero, F Bosia, M Vannoni, S Calusi, L Giuntini, and M Massi. Evidence of light guiding in ion-implanted diamond. Physical review letters, 105(23):233903, 2010.

[98] Joel W Ager III, D Kirk Veirs, and Gerd M Rosenblatt. Spatially resolved raman studies of diamond films grown by chemical vapor deposition. Physical Review B, 43(8):6491, 1991.

[99] J Schwan, S Ulrich, V Batori, H Ehrhardt, and SRP Silva. Raman spectroscopy on amorphous carbon films. Journal of Applied Physics, 80(1):440–447, 1996.

[100] Belén Sotillo, Vibhav Bharadwaj, JP Hadden, Masaaki Sakakura, Andrea Chiappini, Toney Teddy Fernandez, Stefano Longhi, Ottavia Jedrkiewicz, Yasuhiko Shimotsuma, Luigino Criante, et al. Diamond photonics platform enabled by femtosecond laser writing. Scientific reports, 6, 2016.

[101] Leilei Huang, Patrick Salter, Michał Karpiński, Brian Smith, Frank Payne, and Martin Booth. Waveguide fabrication in kdp crystals with femtosecond laser pulses. Applied Physics A, 118(3):831–836, 2015.

[102] Jing Bai, Guanghua Cheng, Xuewen Long, Yishan Wang, Wei Zhao, Guofu Chen, Razvan Stoian, and Rongqing Hui. Polarization behavior of femtosecond laser written optical waveguides in ti: Sapphire. Optics express, 20(14):15035–15044, 2012.

[103] B Sotillo, A Chiappini, V Bharadwaj, JP Hadden, F Bosia, P Olivero, M Ferrari, R Ramponi, PE Barclay, and SM Eaton. Polarized microraman studies of femtosecond laser written stress-induced optical waveguides in diamond. arXiv preprint arXiv:1711.09140, 2017.

[104] Koch MK, Hoese M, Bharadwaj V, Lang J, Hadden JP, Ramponi R, Jelezko F, Eaton SM, Kubanek A. Super-Poissonian Light Statistics from Individual Silicon Vacancy Centers Coupled to a Laser-Written Diamond Waveguide. ACS Photonics. 2022 Oct 19;9(10):3366-3373. doi: 10.1021/acsphotonics.2c00774. Epub 2022 Oct 4. PMID: 36281332; PMCID: PMC9585639.

[105] Sipahigil, A.; Jahnke, K. D.; Rogers, L. J.; Teraji, T.; Isoya, J.; Zibrov, A. S.; Jelezko, F.;

Lukin, M. D. Indistinguishable Photons from Separated Silicon-Vacancy Centers in Diamond. Phys. Rev. Lett. 2014, 113, 113602.

[106] Polino, E.; Valeri, M.; Spagnolo, N.; Sciarrino, F. Photonic quantum metrology. AVS Quantum Sci. 2020, 2, 024703.

[107] S Pezzagna, B Naydenov, F Jelezko, J Wrachtrup, and J Meijer. Creation efficiency of nitrogen-vacancy centres in diamond. New Journal of Physics, 12(6):065017, 2010.

[108] T Yamamoto, T Umeda, K Watanabe, S Onoda, ML Markham, DJ Twitchen, B Naydenov, LP McGuinness, T Teraji, S Koizumi, et al. Extending spin coherence times of diamond qubits by high-temperature annealing. Physical Review B, 88(7):075206, 2013.

[109] Eaton, S.M.; Hadden, J.P.; Bharadwaj, V.; Forneris, J.; Picollo, F.; Bosia, F.; Sotillo, B.; Giakoumaki, A.N.; Jedrkiewicz, O.; Chiappini, A.; et al. Quantum micro–nano devices fabricated in diamond by femtosecond laser and ion irradiation. Adv. Quantum Technol. 2019, 2, 1900006.

[110] Alexander M Streltsov and Nicholas F Borrelli. Study of femtosecond-laser-written waveguides in glasses. JOSA B, 19(10):2496–2504, 2002.

[111]James W Chan, TR Huser, SH Risbud, and DM Krol. Modification of the fused silica glass network associated with waveguide fabrication using femtosecond laser pulses. Applied Physics A, 76(3):367–372, 2003.

[112] Lilia Coronato Courrol, Ricardo Elgul Samad, Laércio Gomes, Izilda Márcia Ranieri, Sonia Licia Baldochi, Anderson Zanardi de Freitas, and Nilson Dias Vieira Junior. Color center production by femtosecond pulse laser irradiation in lif crystals. Optics express, 12(2):288–293, 2004.

[113] JR Rabeau, Patrick Reichart, Grigori Tamanyan, DN Jamieson, Steven Prawer, Fedor Jelezko, Torsten Gaebel, Iulian Popa, Michael Domhan, and J Wrachtrup. Implantation of labelled single nitrogen vacancy centers in diamond using n 15. Applied Physics Letters, 88(2):023113, 2006.

[114] Yu-Chen Chen, Patrick S Salter, Sebastian Knauer, Laiyi Weng, Angelo C Frangeskou, Colin J Stephen, Shazeaa N Ishmael, Philip R Dolan, Sam Johnson, Ben L Green, et al. Laser writing of coherent colour centres in diamond. Nature Photonics, 11(2):77–80, 2017.

[115] Boris Naydenov, Friedemann Reinhard, Anke Lämmle, V Richter, Rafi Kalish, Ulrika FS D'Haenens-Johansson, Mark Newton, Fedor Jelezko, and Jörg Wrachtrup. Increasing the coherence time of single electron spins in diamond by high temperature annealing. Applied Physics Letters, 97(24):242511, 2010.

[116] Belén Sotillo, Vibhav Bharadwaj, John Patrick Hadden, Stefano Rampini, Andrea Chiappini, Toney T Fernandez, Cristina Armellini, Ali Serpengüzel, Maurizio Ferrari, Paul E Barclay, et al. Visible to infrared diamond photonics enabled by focused femtosecond laser pulses. Micromachines, 8(2):60, 2017.

[117] S. Castelletto, A. F. M. Almutairi, K. Kumagai, T. Katkus, Y. Hayasaki, B. C. Johnson, and S. Juodkazis, "Photoluminescence in hexagonal silicon carbide by direct femtosecond laser writing," Opt. Lett. 43, 6077-6080 (2018)

[118] Castelletto S, Maksimovic J, Katkus T, Ohshima T, Johnson BC, Juodkazis S. Color Centers Enabled by Direct Femto-Second Laser Writing in Wide Bandgap Semiconductors. Nanomaterials. 2021; 11(1):72. https://doi.org/10.3390/nano11010072

[119] Sörman, E.; Son, N.T.; Chen, W.M.; Kordina, O.; Hallin, C.; Janzén, E. Silicon vacancy related defect in 4H and 6H SiC. Phys. Rev. B 2000, 61, 2613–2620.

[120] Fuchs, F.; Stender, B.; Trupke, M.; Simin, D.; Pflaum, J.; Dyakonov, V.; Astakhov, G.V. Engineering near-infrared single-photon emitters with optically active spins in ultrapure silicon carbide. Nat. Commun. 2015, 6, 7578.

[121] Ivády, V., Barcza, G., Thiering, G. et al. Ab initio theory of the negatively charged boron

vacancy qubit in hexagonal boron nitride. npj Comput Mater 6, 41 (2020).

[122] T. T. Tran, K. Bray, M. J. Ford, M. Toth, and I. Aharonovich, Nature Nanotechnology 11, 37 EP (2015).

[123] N. Chejanovsky, M. Rezai, F. Paolucci, Y. Kim, T. Rendler, W. Rouabeh, F. Favaro de Oliveira, P. Her- ´ linger, A. Denisenko, S. Yang, I. Gerhardt, A. Finkler, J. H. Smet, and J. Wrachtrup, Nano Letters 16, 7037 (2016).

[124] N. R. Jungwirth, B. Calderon, Y. Ji, M. G. Spencer, M. E. Flatte, and G. D. Fuchs, Nano Letters ´ 16, 6052 (2016).

[125] A. Bommer and C. Becher, Nanophotonics 0 (2019), 10.1515/nanoph-2019-0123